Construction of a portable platform for cold atom interferometry

by

Jonathan Ian Malcolm

A thesis submitted to
The University of Birmingham
for the degree of
DOCTOR OF PHILOSOPHY

Midlands Ultracold Atom Research Centre
School of Physics and Astronomy
College of Engineering and Physical Sciences
The University of Birmingham

December 2015

Abstract

This thesis details the construction of a portable platform for cold atom experiments, as part of the European iSense project. This culminated in the demonstration of a working portable cold atom interferometer to the praise of the EC and reviewers during the final project meeting. Reductions in the size, weight and power consumption of all the crucial components for a cold atom system such as lasers, optics, magnetic field generation and electronics have been realised. These novel components have been integrated into a portable device that has been transported and operated by just two people. The completed device weighs 63 kg and uses 240 W power in a volume of just 61.1 litres. The system has generated a cloud of $(6.7 \pm 0.7) \times 10^6$ rubidium-87 atoms at a temperature of 4.4 µK in 2 seconds using a mirror-MOT setup. The device has successfully performed atom interferometry in the form of a Ramsey interferometer both at the University of Birmingham, UK and also at an office in Brussels, BE after a journey of 570 km. A measurement of the hyperfine splitting of the ground state of ^{87}Rb was performed and gives an uncertainty of $\delta\omega/\omega = 5.2 \times 10^{-7}$. The theoretical limit of the sensitivity to gravity of the iSense system is 3.9 µGal/$\sqrt{\text{Hz}}$.

It is well known that a vital ingredient of success is not knowing that what you're attempting can't be done.

Sir Terry Pratchett, 1948-2015

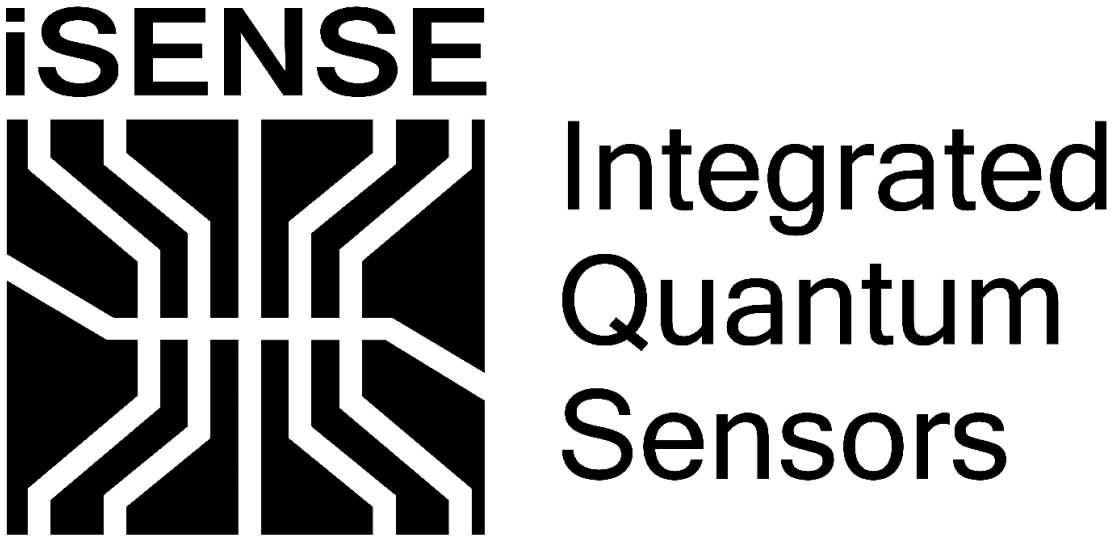

iSense Project Logo

ACKNOWLEDGEMENTS

First of all, thanks to my supervisor, Kai Bongs. Without him, this project would never have existed. His drive to push the technical limits of cold atom experiments, sometimes in very limited timeframes, was at times frustrating, but ultimately generated fantastic results. His belief that travel is a fundamental part of research was greatly appreciated and allowed me to visit amazing labs, people and places all across Europe.

Tristan, thanks for easing me into the PhD life and imparting valuable pearls of wisdom such as the ingredients in an 'authentic' paella, and how to pull off the 'Godfather' look at weddings. Thank you Mike for pushing the project in my final months (and beyond), and for the support during this write-up. Thanks to Vincent for the critical advice and assistance along the way.

Lingxiao and Clemens, thank you for your continuing hard work pushing iSense further forward day by day. I'm looking forward to seeing the system out and about in future, turning the heads of important people. Chris, for sharing the lab for the last few years and putting up with spontaneous visits from high-ranking officials and some mysterious grounding issues. Thankfully, a similar taste in music probably kept us sane for the most part. Andy, for giving me someone to go see crazy Japanese bands with. Everyone else in the Cold Atom/Quantum Matter group during my time there. We've had lots of adventures over the years, everyone has made it a pleasure to work and study (and play!) in Birmingham.

Big thanks to everyone in the iSense collaboration that has contributed to the project, it wouldn't have been possible without you all. Berlin, Hannover, SYRTE, FBH, Florence, Institute d'Optique, Innsbruck, ONERA and Nottingham. Funding from European

Union's Seventh Framework Programme under grant agreement no. 250072.

Thanks to my examiners, Professor Ifan Hughes and Dr Alan Watson, for reading the thesis and conducting my viva. It was a pleasure!

Thanks to all the people at the IQO in Hannover for making a naïve young PhD student (who can't speak German) feel very welcome and at home in your marvellous castle for a few months, and at subsequent meetings and conferences. In particular the QUANTUS crew. I wish you all the best of luck with strapping your experiments to thousands of kilos of rocket fuel to see what happens.

To the original sat-in-the-back-corner-too-cool-for-school-West-117-crew: Andy, Joe and Tanya. It's been an amazing 8 years and the next step seems to involve dispersing across the planet. Hopefully that'll lead to some adventurous holidays in the not too distant future, good luck to all of you.

The mechanical workshop team at Birmingham have always been helpful and irreplaceable. Thanks for all your hard work building everything that I've asked for without fail and always to extremely high standards.

All of the others who exist outside of the Physics buildings, the housemates, the archery people, the rock music people; it's been a blast. Birmingham wouldn't have been as interesting without you. Jo and Matt, thanks for reading the thesis and making sure it all made sense.

Finally, to my sister and my parents. Always supportive, always interested, always excited, always worried and always there.

PUBLICATIONS

Scientific papers including the author

Müntinga H et al. including Malcolm J 2013 Interferometry with Bose-Einstein Condensates in Microgravity *Physical Review Letters* **110** 093602

Bongs K, Malcolm J et al. 2014 iSense: A Technology Platform for Cold Atom Based Quantum Technologies *in Research in Optical Sciences, OSA Technical Digest* **QTu3B.1**

Presentations by the author

MUARC Summer School, Grenada, September 2011, *Poster*

Young Atom Opticians Conference, Krakow, March 2012, *Poster*

GGtop Launch Event, London, May 2012, *Poster*

508. Heraeus Conference, Bad Honnef, June 2012, *Poster*

IOP Quantum Technologies Meeting, London, December 2012, *Poster*

DSTL Town Meeting: Precision Timing (and Navigation) Technology, Harwell, March 2013, *Poster*

Young Atom Opticians Conference, Birmingham, April 2013, *Poster*

Enrico Fermi School: CLXXXVIII Atom Interferometry, July 2013, *Poster*

UK National Quantum Technology Hub in Sensors and Metrology: Kickoff Meeting, Nottingham, January 2015, *Poster*

Quantum Technologies Strategic Meeting, Chichely Hall, March 2015, *Live Demo*

CONTENTS

LIST OF FIGURES

LIST OF TABLES

CHAPTER 1

INTRODUCTION

Devices that use 'classical' principles to measure physical properties of the world around us are commonplace. They can be found in smartphone accelerometers, laser gyroscopes in aircraft and clocks in navigation systems to name but a few. They are typically based on a macroscopic object that undergoes motion when a force is applied to it, which is tracked in ways such as through an optical interferometer to give a measurement of that force. This idea leads back to experiments such as the (disputed) dropping of objects from the Leaning Tower of Pisa to observe their rate of fall by Galileo in the 16th-17th Century. The demand and progress in devices that utilise this principle has been remarkable in the past hundred years. However, devices that measure in this way are seen to be reaching their limits in sensitivity and scalability, and a fundamental shift in the methods that we use to measure our environment is needed; a shift towards the quantum world.

Since the first successful trapping and cooling of atoms in experiments during the 1980s, an explosion of research in this field has taken place and the best precision measurements of forces and fundamental constants are now held in the majority by cold atom based systems [1, 2]. Quantum technologies based on cold atoms have remained for the most part confined to the laboratory environment. The need for vacuum chambers, magnetic fields and complex laser systems, and electronics of high quality that all work together meant that transporting an entire cold atom experiment was far from the

forefront of the minds of researchers.

In recent years however, we have reached a stage of development where this technology can begin to leave the laboratory and venture out into the wider world. Portable Bose-Einstein Condensate (BEC) apparatus exist [3] and are being commercialised [4]. Cold atom experiments that take place in extreme environments such as parabolic flights [5] and droptowers [6] where the entire experiment is in freefall are currently operating. The lessons being learnt in these experiments are being used to develop space-worthy cold atom experiments [7].

Appealing to the outside world means constructing devices that are able to perform tasks that are deemed useful to consumers or industry in some way. Gyroscopes, clocks, quantum memory and communication are all of great interest and have groups working towards portable cold atom implementations of them. However, it is gravitational acceleration sensing that is being seen as the best way to show the potential benefits of cold atoms. The basic tools for all of these systems are very similar and so an effort to condense the laboratory into a modular, scalable, technology platform that could be implemented in multiple experiments is of great interest.

1.1 Atom Interferometry as a Method for Precision Measurements

The wave nature of atoms has been known since the founding of quantum mechanics, typified by the performing of the double slit experiment with electrons [8] and observing the same interference that occurs when using light. Perhaps the most well known use of atom interferometry is in the field of timekeeping. The method developed by Ramsey in the 1940s and 1950s [9] that enabled precise measurement of atomic transition frequencies is now the basis of our entire definition of time. It is used in the caesium atomic fountain clocks found in national laboratories around the world, such as NPL (GB), PTB (DE), SYRTE (FR) and NIST (US), to define the value of the second.

The first measurements of gravity based on matter waves were reported in 1975 by Colella, Overhauser and Werner [10, 11]. They used a beam of neutrons passing through three silicon plates to generate their interferometer. Tilting the angle of the plates with respect to the beam created interference patterns caused by a gravitationally induced phase shift on the neutrons. In 1991, Kasevich and Chu demonstrated interference of trapped and cooled sodium atoms [12]. They used a sequence of laser pulses based on the principles of Ramsey and Bordé [13] to extract a reading of the gravitational acceleration of the atoms [14]. The advantage of using atoms over electrons and neutrons for interferometry is that their de Broglie wavelengths ($\lambda = h/p$) are much smaller, leading to more precise measurements. As their mass is extremely well defined, and each atom of an element has exactly the same properties, they are the perfect test masses compared to man-made objects. The interference of larger mass objects such as molecules containing hundreds of atoms is also being investigated [15, 16] with the goal to observe the boundary between the classical and quantum worlds.

Cold atom gravimeters have been construceed in laboratories around the world [17]. Aside from absolute measurements of gravitational acceleration, atom interferometry also lends itself to other precision measurements including the gravitational constant 'G' [18, 19], gravity gradient [20] and lately the curvature [21], rotations [22], the universality of free-fall [23] and the fine structure constant [24, 25, 26]. There are even plans for cold atom based gravitational wave detectors [27, 28]. While gravity measurements tend to take the same form, the fine structure constant is calculated by measuring the recoil velocity of atoms when absorbing photons and rotations are measured when the atoms are travelling in horizontal - rather than vertical - directions. Examples of this include trapped BECs on a ring [29, 30], but the general atom interferometry techniques are analogous.

Source	Gravity (μGal)
Earth	9.8×10^8
Solid Earth Tides	300
Ocean Loading	20
Hydrology	10
Postglacial Rebound	10
Ice and Glaciers	5
Minerals	1000

Table 1.1: Select list of sources of gravitational variation on Earth, and their strengths in μGal. Compiled from [31, 32, 33].

1.2 Portable Gravimetry

Gravity measurements are of interest to many fields - a few of the large geographical sources of gravity variations are listed in table 1.1 with their typical magnitudes. In these fields the most commonly used unit is the gal, named after Galileo, where 1 Gal = 0.01 $\mathrm{m\,s^{-2}}$. Geodesists use gravity measurements on scales from boreholes up to planet-scale surveys. Measurements taken using satellite instruments such as GRACE and GOCE show large scale variations in gravity across the planet. The uses of these measurements include observing ice sheet thickness [34], a particular concern for the present day, and mapping the Earth's geoid (the shape of the Earth according to gravity) to discern the composition of the planet. Due to the extremely large distance of the satellite-based sensor from the source, the horizontal resolution is on the kilometre scale. This is not suitable for, for example, finding specific objects underground such as mineral deposits or historical objects. In the mid-range, oil and mineral prospectors use gravity gradiometers with high repetition rates onboard aircraft to map out regions of interest before taking finer ground measurements. Finally on the smaller scale, higher resolution ground-based measurements give local variations such as the post-glacial rebound of Northern Europe since the last ice age [35], locating buried objects, or mapping groundwater and geological features. Fixed gravity sensors could also be employed as additional early warning devices for volcanic eruptions [36]. There are other fields in which a portable, precise, gravimeter could be of use. These include archaeology, civil engineering [37] and the field of defence

where it could act as an unblockable and undetectable passive navigation system, removing the reliance on GPS systems.

There are two types of device used to measure gravity: absolute gravimeters that aim to give a precise measurement of the value of g at a specific point, and relative gravimeters that record changes in gravity. A relative gravimeter is generally smaller and more capable of performing faster measurements, but it needs to be calibrated to a stable central measurement point.

'Classical' relative gravimeter devices such as the Scintrex CG-5 measure variations in gravity by watching the position of a mass suspended on a spring. They are typically small devices easily movable by a single person, and are very rugged meaning that they can be used in quite extreme environments. The length of the spring drifts over time as it stretches and deforms and so it constantly needs correcting.

Superconducting gravimeters currently give the most sensitive gravity measurements available, down to the region of 1 nGal [38]. They employ a metallic sphere that is levitated by two superconducting wire rings cooled to 4 K. The current applied to the rings is extremely stable since superconductors have zero resistance. The ring generates a magnetic field used to cancel the downward gravitational force [39]. However, this is still a relative measurement so a central reference point still needs to be used.

Micro-G LaCoste FG5 Absolute Gravimeter The FG5 is the most widely used device for portable absolute gravity measurements. No other device is currently in production and so its stated accuracy of 2 µGal is only by comparison to other FG5 gravimeters. It works by using an optical interferometer to track the acceleration of a reflective cube that is dropped for 20 cm in an evacuated chamber. The cube is caught at the bottom and raised to the top to repeat the measurement. Since this is a mechanical device, no two FG5 instruments give exactly the same measurement, even in the same location, and so periodically have to be brought together for comparison [40] and recalibration. Errors in the positioning of the cube and mechanical wear over time reduce the sensitivity of the device. From the specifications available

online [41], the FG5 weighs 150 kg and is transported in six containers, requiring assembly at the measurement site. Its operating temperature range is only $20 - 30$ °C and so measurements typically take place in a controlled environment such as an air conditioned hut [42].

Cold atom gravimeters, by their nature, give absolute measurements and have they have a greater opportunity to be miniaturised. They suffer neither mechanical drifts nor mechanical wear and tear as there are no moving parts. Since atoms of the same element are identical for everyone, different cold atom gravimeters should give the same result when compared in the same locations. Comparisons can clearly only be made using cold atom gravimeters that are portable.

Other groups have achieved what they dub 'truckable'; or 'transportable' atom interferometers, such as GAIN in Berlin [43, 44], CAG at LNE-SYRTE [45] and work carried out at ONERA [46], Stanford [47] and groups in China [48, 49]. As the terminology suggests, these are typically suitable only for transport within a vehicle and are not truly 'portable' in the way that a suitcase is portable. The GAIN device is of particular note because it has performed mobile gravimetry comparisons with the FG5, and has recorded a level of sensitivity higher than the FG5 [50].

1.3 The iSense Project

iSense (Integrated Quantum Sensors) is a European Union funded project with the goal of combining research and technological developments from across Europe to create a platform upon which portable cold atom devices could be constructed. The members of the collaboration are listed in appendix A. The steps included are the shrinking of the vacuum system, magnetic coils, laser system and optics, and all of the required electronics. The first realisation of iSense is the building of a portable cold atom interferometer that is robust enough to perform gravity measurements in the field with input from only one or two people.

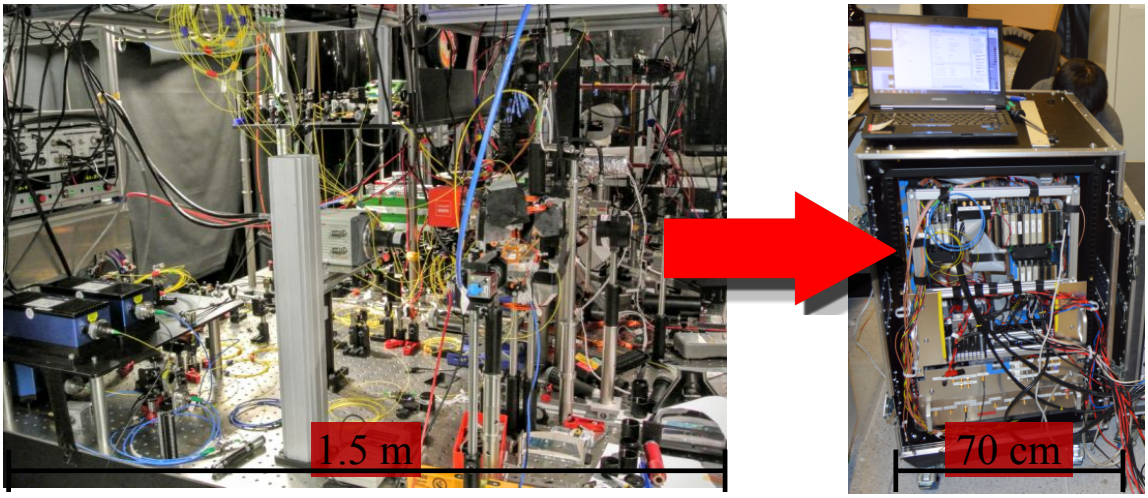

Figure 1.1: Shrinking a cold atom experiment from an optical table to a portable device.

This thesis covers the development of the iSense demonstrator, the characterisation and integration of all the novel components into a working, portable cold atom platform for atom interferometry.

1.4 Statement of Contributions

The construction of a device as complex as iSense involves many parties. The subsystems described in chapter 3 were developed by members of the iSense consortium; the lasers by FBH and UHH, the electronics by LUH, and the atom chip assembly by UNott. Birmingham designed the vacuum chamber and the complete integration of the subsystems into the quantum technology platform.

The author performed the integration of the subsystems detailed in chapter 4 into a benchtop cold atom system. This work involved taking the components developed by the other institutes, characterising them and then integrating all into a single cold atom platform. In particular the author developed the optical delivery system, the interfaces between the light and the vacuum chamber, between the components and electronics, and the experimental control interface. Following the integration of the components into an operational system that generated a cold atom cloud; the atom interferometry, the

optimisation of the system and the packaging was continued by the team of the author, C Rammeloo and L Zhu, of which the author was the senior student. L Zhu focussed on the optical molasses optimisation and C Rammeloo led the packaging of the system into a portable device.

The transportation of the device and the measurements performed in Brussels were carried out by this team of doctoral students. The details of the portable system are found in chapter 5. The results presented in chapter 6 are also the product of this team. The discussion of portability and future improvements, and the analysis and the discussion of the results given in this thesis are the work of the author.

The author's supervisor, K Bongs, who was leader of the iSense project, and V Boyer were involved in and aided the project throughout; along with that of two consecutive research fellows in charge of all atom interferometry activities at Birmingham, T Valenzuela, who led the initial transition from an empty laboratory to magneto-optical trapping, and then M Holynski, who led the push from the benchtop to the portable system.

CHAPTER 2

THEORY

In this chapter an overview of some of the key theoretical points behind the experiment is presented. This is by no means comprehensive and other sources [51, 52] go into far greater detail, but it is hoped that this outline will provide enough of a foundation to understand the needs and operation of the system and the requirements of the components used to construct it. First will be a description of the preparation of the atomic cloud, which involves laser cooling and magneto-optical trapping processes. This is followed by a description of the most common method of atom interferometry, leading into its use to measure gravity. Finally, some alternative methods are described, as these have influenced the design of the system and are under consideration for implementation in the future.

2.1 Cold Atom Cloud Preparation

Gravity measurements using atom interferometry require light-atom interactions and evolution periods that take place over hundreds of milliseconds. The sensitivity of gravimeter schemes in which the atoms are in freefall increases dramatically with longer times. The velocity of an atom – in one dimension – with mass m can be calculated from its temperature T with

$$v = \sqrt{\frac{k_{\mathrm{B}}T}{m}}, \tag{2.1}$$

where k_B is the Boltzmann constant. At room temperature (≈ 300 K), atoms travel at around $v = 300\ \mathrm{m\,s^{-1}}$. This velocity means that individual atoms would pass out of our interaction region in times less than 100 µs; a timescale that is useless for precise gravity measurements using atom interferometry where timescales of hundreds of milliseconds are typical. Collisions between atoms at this velocity also collapse the quantum state used in atom interferometry, ruining the measurement. Laser cooling of atoms is the method that is used to reduce the velocity of a large number of atoms so that they become a useful and controllable resource for an atom interferometer. Laser cooling reduces the velocity of the atoms to the region of a few $\mathrm{cm\,s^{-1}}$ allowing for interactions to take place over a much longer time. We describe the velocity spread of the atoms in terms of a temperature since the average kinetic energy of the atoms $\langle E_k \rangle$ can be written as

$$\langle E_k \rangle = \frac{1}{2} m \langle v^2 \rangle = \frac{3}{2} k_B T,$$

where m is the mass of the atomic species, $\langle v^2 \rangle$ is the RMS velocity of the atoms. Room temperature is around 300 K and a laser cooled sample reaches a temperature of tens of microkelvin.

2.1.1 Laser Cooling

Laser cooling requires an atom that has two energy levels which can be addressed by a cycling optical transition. A cycling transition means that the atom cycles between two energy levels continuously as long as the atom is subject to a light field near enough to resonance. An atom in the ground state will absorb a photon from the light field with an energy equal to the separation of the internal energy levels. This leads the atom to have a change of momentum in the direction of the propagating light field. Since the atom cannot exist forever in the excited state it subsequently returns to the ground state by spontaneously emitting a photon in a random direction. Due to the closed nature of the transition, this process will continue and the atom will receive a push that averages to be

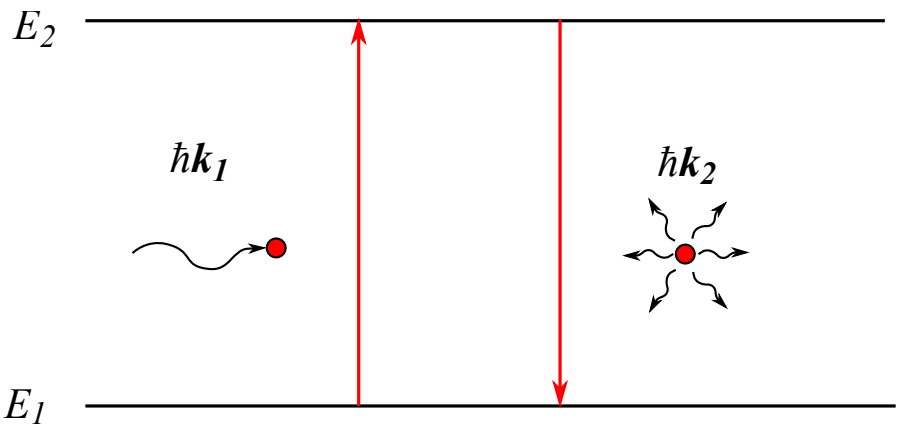

Figure 2.1: Absorption and emission process used in the laser cooling of a two-level atom with a resonant light beam. The atom absorbs the photon from the light field and gains its momentum. It then spontaneously emits a photon to return to the ground energy level. This photon is emitted in a random direction resulting in a net reduction in the momentum of the atom in the direction towards the light source.

in the direction of the light field.

The Optical Molasses

The optical molasses technique is called so because opposing light beams are used to create a region that appears viscous to the atoms, like moving through a thick molasses (treacle/syrup). The method cools atoms through exploiting the Doppler effect in which an atom in motion 'sees' the frequency of a light field shifted depending on its velocity.

To implement an optical molasses we use counter propagating light beams that are set to a frequency lower than the resonant frequency of the transition - we call them 'red detuned'. Due to the Doppler effect, an atom that is in motion towards the source of one of the light beams will see the frequency shifted upwards back towards resonance with the opposing beam shifted down in frequency. The energy levels are not infinitely narrow lines, but instead have a width that has a Lorentzian shape. This means that the frequency of light needs only to be near to resonance, in that case the atom will absorb a photon from the light field and the momentum of the photon is given to the atom. This is depicted in figure 2.2 for one dimension.

The use of a cyclic transition causes this process to occur repeatedly, leading to a

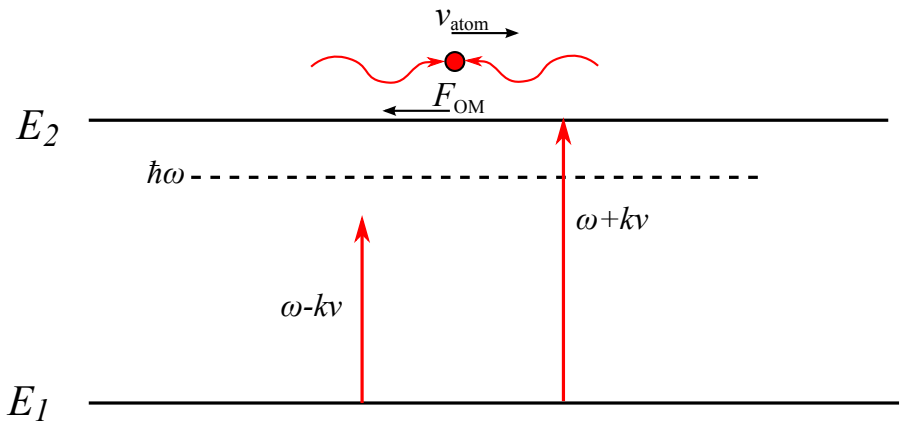

Figure 2.2: Optical molasses method in one dimension. Two opposing laser beams that are set to frequency ω that is lower than the transition frequency are used. An atom moving towards one beam with velocity v will see the frequency of that beam shifted towards resonance by $+kv$ while the other is shifted further away by $-kv$. The lines depicting the energy levels E_1 and E_2 in reality have a Lorentzian linewidth meaning that the light does not have to be exactly on resonance to be absorbed.

greatly reduced velocity along the axis of the light field. Obviously, if only a single pair is used, only atoms travelling along one dimension will be cooled [53]. In practice this can be used to create a focussed beam of atoms. The setup was extended to three dimensions by Chu et.al. in 1985 [54] who applied opposing light fields in three orthogonal axes. The central region where the beams overlap becomes a three dimensional optical molasses, cooling atoms that are travelling in all directions.

In one dimension, the force on the atom caused by the absorption and subsequent emission of a photon from the light field by an atom with a velocity v is given by

$$\mathbf{F} = \frac{\hbar\mathbf{k}\Gamma}{2}\frac{s_0}{1+s_0+\left[2(\delta+\omega_D)/\Gamma\right]^2}, \tag{2.2}$$

where s_0 is the saturation parameter, the ratio of beam intensity to saturation intensity of the transition I/I_{sat}, $\delta = \omega_{\text{laser}} - \omega_{\text{transition}}$ is the detuning, Γ is the linewidth of the excited state – given by the inverse of the lifetime of the state – and $\omega_D = -\mathbf{k}\cdot\mathbf{v}$ is the Doppler correction to the frequency due to the fact that the atom is moving. In essence this force is the scattering rate of the light on the transition multiplied by the momentum transferred by the photon to the atom ($\hbar\mathbf{k}$). Adding the forces from two fields in opposing

directions (with opposite wavevectors, $\mathbf{k}$ and $-\mathbf{k}$) $\mathbf{F}_{\mathrm{OM}} = \mathbf{F}(\mathbf{k}) + \mathbf{F}(-\mathbf{k})$ and removing the high order terms gives the resulting optical molasses force in 1D

$$\mathbf{F}_{\mathrm{OM}} \cong -\beta \mathbf{v}, \tag{2.3}$$

where

$$\beta = \frac{8\hbar k^2 \delta s_0}{\Gamma \left(1 + s_0 + (2\delta/\Gamma)^2\right)^2}. \tag{2.4}$$

This is a velocity dependent force. Atoms with velocities near to zero feel no effect and continue to travel unopposed but atoms with higher velocities will experience a force opposing their motion as they will observe the light from one beam shifted towards resonance. The force has a shape such that it only affects atoms with a range of velocities about zero. Atoms with higher velocities will escape the cooling regime altogether without being affected by the light. The effective range of the optical molasses force is called the capture velocity and it can be estimated by $v_c \approx \Gamma/k$ [52, p.190]. Take note that the atoms are not confined in any way by the optical molasses force, once the atoms have been slowed they will continue to move until they escape the cooling region altogether.

There is a theoretical limit on the temperature that can be reached using laser cooling; this is called the Doppler temperature. This limit arises due to the fact that the light beams also cause some heating of the atoms due to the randomness of the direction of the spontaneous emission from each scattering event. Over the large number of scattering events that are involved in the laser cooling process, this balances to a non-zero kinetic energy and equivalent temperature governed by the linewidth of the transition. The Doppler temperature limit is given by [51]

$$T_D = \frac{\hbar \Gamma}{2k_{\mathrm{B}}}. \tag{2.5}$$

As an example, for the cooling transition in ^{87}Rb, the linewidth is $\Gamma = 2\pi \times 6.066$ MHz

[55] which gives a Doppler temperature of $T_D \approx 145$ µK.

Soon after the first realisation of a 3D optical molasses, it was found that without using any additional cooling techniques the temperatures that could be reached were surprisingly lower than this 'limit' [56] and could even reach an order of magnitude lower than the Doppler temperature. One explanation of the reason behind this is that the models used to calculate the Doppler cooling limit do not take into account the effect of the polarisation of the beams. This leads to an additional cooling force, likened to Sisyphus pushing a boulder up a hill and having it eternally roll back down. The fact that it is not a true two-state system, since the atoms used are multi-levelled, also has an effect [57].

2.1.2 The Magneto-Optical Trap

The optical molasses force does not provide any spatial confinement of the atoms and it only cools a small range of atoms that are already low in velocity and near resonance. In order to trap atoms, a magnetic field is added on top of the optical molasses light to create a Magneto-Optical Trap (MOT) [58]. This takes the form of a quadrupole field with a well defined zero that increases linearly away in all directions. The MOT can capture a larger range of velocities than an optical molasses, allowing us to collect and cool a greater number of atoms and keep them confined to a small region of space around the minimum of the magnetic field.

The addition of the magnetic field causes a position dependent shift of the (non-zero) m magnetic sublevels of the energy state due to the Zeeman effect. The shift in energy is given by $\Delta E = \mu_B g m B \hbar$ [51] where μ_B is the Bohr Magneton, g is the Landé g-factor of the energy level and B is the magnitude of the applied magnetic field.

Here it is important to introduce the description that a σ^- transition is defined as one in which one unit of angular momentum is removed from the atom by a circularly polarised beam. This takes the form of a shift to a lower numbered m sublevel in the excited state, such as $|E_1, m = 0\rangle \rightarrow |E_2, m = -1\rangle$. A σ^+ transition adds one unit of angular momentum

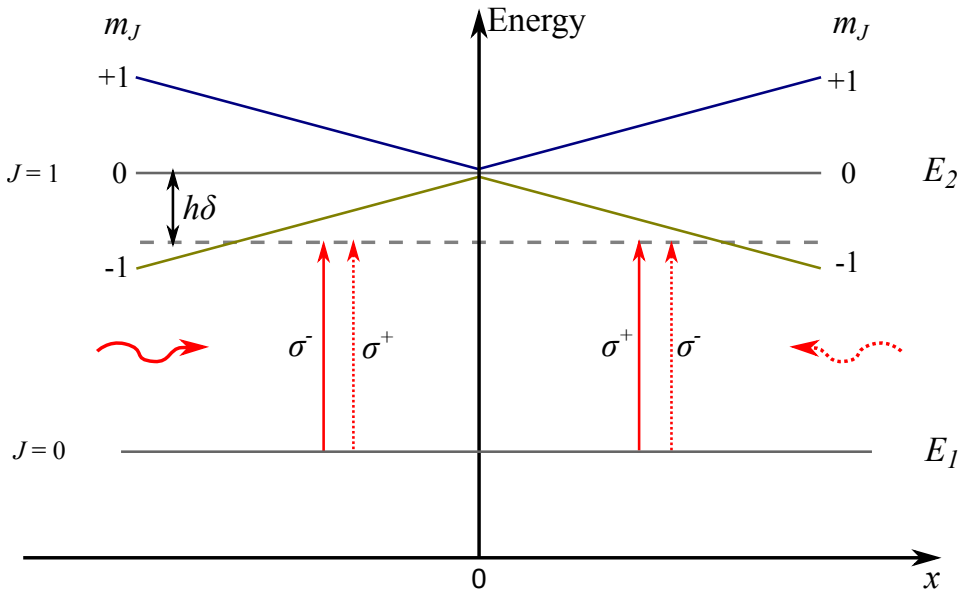

Figure 2.3: Simplified magneto-optical trapping principle in 1D for J = 0 → J = 1 transition with opposing laser beams at detuning δ below the transition frequency. In this case both beams are configured with the same polarisation with respect to the light propagation. The beam from the left (solid line) is polarised to address a σ^- transition for $x < 0$ and σ^+ for $x > 0$. The beam from the right (dotted line) is σ^- for $x > 0$ and σ^+ for $x < 0$. The applied magnetic field alters the energy of the m_J states such that the $m_J = -1$ state is shifted towards resonance either side of zero. An atom at $x < 0$ will absorb a photon travelling from the left and gain a momentum kick towards $x = 0$, alternatively an atom at $x > 0$ will receive a kick from the right, back towards $x = 0$. This results in a position dependant force that causes the atom position to tend towards $x = 0$.

and thus increases the m number, for example $|E_1, m = 0\rangle \rightarrow |E_2, m = +1\rangle$.

The effect of adding this magnetic field combined with circularly polarised cooling light causes a force acting on the atoms towards the centre. A simplified model of the effect is illustrated for 1D in figure 2.3 and described here. In this simplification the system is a $J = 0 \rightarrow J = 1$ transition, and as such the ground state E_1 is magnetically insensitive. This is not the case in reality since atoms have much more complicated structures due to their non-zero J values, causing hyperfine splitting in both upper and lower J-levels into F-levels that are then split into the magnetic sublevels m_f. The process, however still works in much the same way because optical pumping causes the ground state of a real atom to be, in effect, reduced to a single level.

Two opposing light beams polarised with the same handedness (rotation direction of

the electric field as viewed by the source) are set at a frequency lower than the transition frequency by a detuning δ. An atom on the left of the diagram ($x < 0$) sees the light of the beam from the left to be polarised for a σ^- transition and the beam from the right as σ^+. Since the $m_J = -1$ level is shifted towards resonance by the magnetic field the atom will absorb a photon from the left beam and undergo a σ^- transition, gaining a momentum kick towards $x = 0$. In the case of an atom at $x > 0$, the beam from the right is now polarised for σ^- and the left beam for σ^+. This time the atom will absorb a photon travelling from the right and gain a momentum kick towards $x = 0$ [59].

Experimentally this is typically realised for three dimensions by using six counter-propagating beams and a pair of circular wire coils with current flowing in opposing directions as shown in figure 2.4a. The magnetic field used typically has a gradient near the minimum of around 10 $\mathrm{G\,cm^{-1}}$ [52, p.194], although this can vary for different systems. One handedness of circular polarisation is used for the two beams along the axis of the coils and the other for the remaining four. This is due to the direction of the magnetic field – in that it is directed towards the centre along the axis of the coils and away from the centre in the other two dimensions. This combination generates the directional σ^+, σ^- light around the central region required for the MOT.

2.1.3 Use of an Atom Chip and the Mirror-MOT

For this experiment, we have employed an alternative method for generating this magnetic field by means of an atom chip assembly, the design of which will be detailed in later sections. Through the use of a mirrored surface placed near to the atoms, the number of beams required can be reduced from six to four. This technique is called a Mirror-MOT and it was first developed in the late 1990s in Munich by Reichel et.al. [60]. Two horizontal counter propagating beams and two that oppose each other at 45° from the plane of the chip surface are used. The other two 'missing' beams are created from the reflection of the two angled beams on the gold surface of the atom chip assembly, restoring the cooling and trapping forces in all three axes. Polarisation considerations are maintained by the

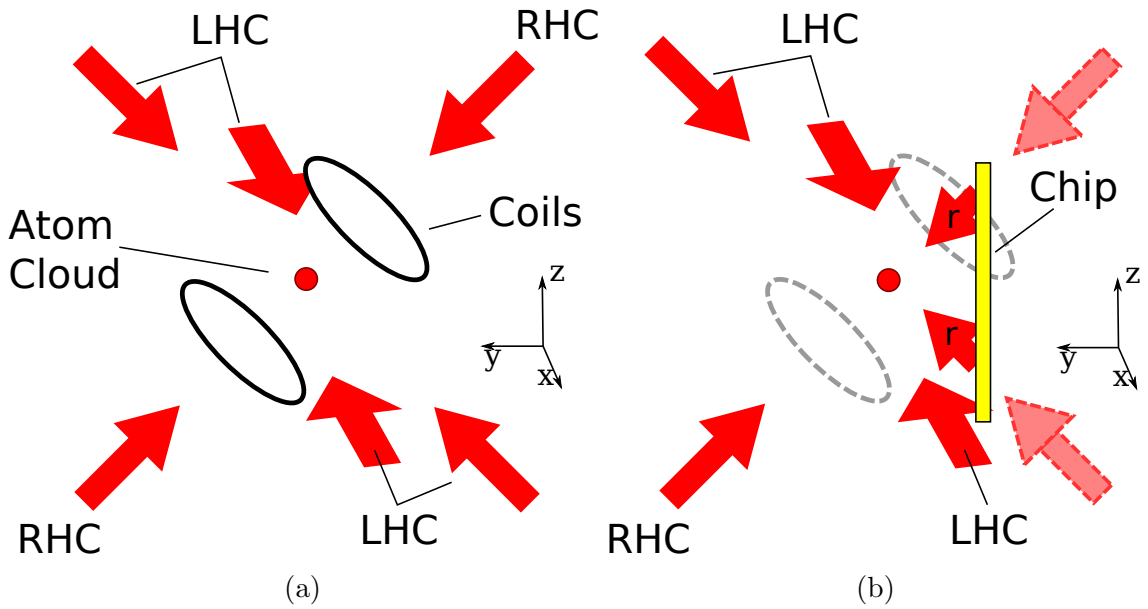

Figure 2.4: Comparison of standard 3D and mirror MOT setups. (a) shows the standard 3D MOT setup with six counter-propagating beams and magnetic coil pair. (b) shows the mirror MOT setup, a mirrored surface is placed in the centre replacing two of the beams (dashed outline arrows) with two reflected beams (labelled 'r'). The chip is also used to generate the trapping magnetic field, removing the need for the coils. LHC and RHC stand for Left and Right Hand Circular polarisation.

rotation caused by the reflection from the surface.

Figure 2.4b shows the setup of the mirror-MOT as in our experiment. The difference from the standard MOT shown beside it is clear - the two beams with a dashed outline have been removed; along with the coils, to be replaced by two reflected beams (labelled 'r') and the chip.

The advantage of using a mirror-MOT, aside from reducing the complexity of the optical system, is that the magnetic fields can be generated much closer to the atoms because optical access is no longer required from the area behind the chip. Placing the coils for generating the trapping field behind the surface of the chip millimetres from the atoms means that the electrical currents needed are much lower. This saves power in multiple ways: firstly lower currents can be generated more efficiently reducing power lost in the power supply, secondly high current in 3D MOT coils can lead to active cooling being needed to prevent the wire from overheating, increasing the size and power consumption of the entire system.

2.2 Atom Interferometry

This section seeks to explain in brief the theory behind atom interferometry as used in this experiment. A much more rigorous explanation can be found in other sources such as Berman [61]. To perform an interferometry experiment using atoms instead of light, we take advantage of the structure of the atom and the fact that there is a probability attached to transitions between energy levels. By tuning the length of a pulse of light we can prepare the atom in a superposition of two energy levels with a probability associated with the pulse length. Since a photon carries momentum, it transfers this to the atom if it is absorbed, leading to a change in the path upon which it is moving.

2.2.1 Rabi Oscillations

When an atom is subjected to an oscillating light field that is on resonance with a closed two-level transition, it begins to cycle between the two states, alternately absorbing from and emitting photons to the beam. This cycling action is called Rabi oscillation and it occurs with a characteristic frequency, called the Rabi frequency, both named afer I.I. Rabi for his work on the basis of the technique in nuclear magnetic resonance (NMR) imaging in the early 20th Century. As a consequence, much of the notation used comes from the NMR field. The oscillations depend on the intensity of the incident light and the amount that it is detuned in frequency from a transition.

For a single photon transition between the ground state $|g\rangle$ and an excited state $|e\rangle$, the Rabi frequency is defined as [62]

$$\Omega_{\text{eg}} = -\frac{\langle e| \mathbf{d} \cdot \mathbf{E} |g\rangle}{\hbar} \tag{2.6}$$

for a resonant transition where $\mathbf{d}$ is the dipole operator, $\mathbf{E}$ is the applied electromagnetic field, with frequency ω and phase ϕ, and takes the form

$$\mathbf{E} = \mathbf{E}_0 \cos(\omega t + \phi). \tag{2.7}$$

.

If the light field is then detuned from the resonance by a frequency δ, the Rabi frequency is corrected by

$$\Omega_{\mathrm{r}} = \sqrt{\delta^2 + \Omega_{\mathrm{eg}}^2}. \tag{2.8}$$

To work out the probability of finding an atom in either state at a certain time, let us consider at time t_0 that the atom's wavefunction $|\Psi\rangle$ exists in a superposition of both states $|g\rangle$ and $|e\rangle$ described by

$$|\Psi(t_0)\rangle = c_e(t_0)\mathrm{e}^{-i\omega_e t}\,|e\rangle + c_g(t_0)\mathrm{e}^{-i\omega_g t}\,|g\rangle\,, \tag{2.9}$$

in which the coefficients $\mathrm{e}^{-i\omega_e t}$ and $\mathrm{e}^{-i\omega_g t}$ oscillate extremely quickly at the laser frequencies $\omega_{e,g}$, and $c_{e,g}$ vary slowly in the case that $\Omega_{\mathrm{eg}} \ll \omega_{e,g}$. If we then apply a light pulse of length τ and detuning δ, the slowly varying coefficients for each state become

$$\begin{aligned} c_e(t_0+\tau) = \mathrm{e}^{-i\delta\tau/2}\Bigg\{ & c_e(t_0)\left[\cos\left(\frac{\Omega_{\mathrm{r}}\tau}{2}\right) - i\cos\theta\sin\left(\frac{\Omega_{\mathrm{r}}\tau}{2}\right)\right] \\ & + c_g(t_0)\mathrm{e}^{-i(\delta t_0+\phi)}\left[-i\sin\theta\sin\left(\frac{\Omega_{\mathrm{r}}\tau}{2}\right)\right]\Bigg\} \end{aligned} \tag{2.10a}$$

$$\begin{aligned} c_g(t_0+\tau) = \mathrm{e}^{-i\delta\tau/2}\Bigg\{ & c_e(t_0)\mathrm{e}^{i(\delta t_0+\phi)}\left[-i\sin\theta\sin\left(\frac{\Omega_{\mathrm{r}}\tau}{2}\right)\right] \\ & + c_g(t_0)\left[\cos\left(\frac{\Omega_{\mathrm{r}}\tau}{2}\right) + i\cos\theta\sin\left(\frac{\Omega_{\mathrm{r}}\tau}{2}\right)\right]\Bigg\} \end{aligned} \tag{2.10b}$$

using the off-resonant Rabi frequency Ω_{r} from (2.8), and with θ being defined by

$$\sin\theta = \Omega_{\mathrm{eg}}/\Omega_{\mathrm{r}}, \qquad \cos\theta = -\delta/\Omega_{\mathrm{r}}, \qquad \text{for } 0 \le \theta \le \pi. \tag{2.11}$$

The phase ϕ that has appeared in these coefficients has been imprinted on the atom by the light field given in (2.7).

In the case of resonant ($\delta = 0$) light incident on an atom in the state $|g\rangle$ the parameters in (2.10) are then ($c_g(t_0) = 1, c_e(t_0) = 0, \sin\theta = 1, \cos\theta = 0$) at a time $t_0 = 0$, and (2.10a)

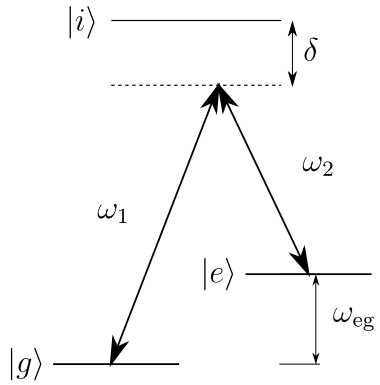

Figure 2.5: Representation of a stimulated Raman transition, a two-photon transition between two hyperfine states $|g\rangle$ and $|e\rangle$ detuned by δ from an intermediate level $|i\rangle$.

is simplified to

$$c_e(\tau) = -i \sin\left(\frac{\Omega_{eg}\tau}{2}\right) \mathrm{e}^{-i\phi}. \tag{2.12}$$

Taking the modulus squared of this and the equivalent for c_g gives the probability of the atom being in each state

$$P_e = \frac{1}{2}\left[1 - \cos\left(\Omega_{\mathrm{eg}}\tau\right)\right] \tag{2.13a}$$

$$P_g = \frac{1}{2}\left[1 + \cos\left(\Omega_{\mathrm{eg}}\tau\right)\right], \tag{2.13b}$$

where τ is the length of the applied light pulse and Ω_{eg} is the effective Rabi frequency as given in (2.6).

It is from here that the terms π and $\pi/2$ pulses originate, used widely in the NMR field. The value of pulse length τ that gives a complete population inversion occurs when $\Omega_{\mathrm{eg}}\tau = \pi$ is satisfied. One method to get an equal probability in each state, is to choose the condition such that $\Omega_{\mathrm{eg}}\tau = \pi/2$.

2.2.2 Stimulated Raman Transitions

A Raman transition is a two-photon process where an atom is transferred between two energy levels via a third virtual level that is far detuned from an intermediate level. The

advantage of this technique is that the momentum transferred to the atom with two photons is much greater than if there was only one. The two levels used are typically separated by gigahertz and the Raman method allows for two terahertz optical photons to be used that have much larger momenta.

A stimulated Raman transition is represented in figure 2.5. Two beams are used with a separation in frequency $\omega_{\mathrm{eg}} = \omega_1 - \omega_2$ equal to the hyperfine splitting. A photon is absorbed from the first beam by the atom, thus changing its momentum in the same direction as the beam; the second beam causes the stimulated emission of a photon in the same direction as that beam. If the two Raman beams are counter-propagating, the momentum transfer given to the atom is proportional to $\mathbf{k}_{\mathrm{eff}} = \mathbf{k_1} + \mathbf{k_2}$ where $\mathbf{k_1}$ and $\mathbf{k_2}$ are the wavevectors of the two Raman beams. For co-propagating beams the momentum transfer becomes near zero since the effective wavevector is now $\mathbf{k}_{\mathrm{eff}} = \mathbf{k_1} - \mathbf{k_2}$.

In practice, we are not dealing with a simple three-level system as discussed previously. Each of these hyperfine states are further split into magnetic sublevels with $\mathrm{m_f}$ numbers. A two-photon Raman transition must keep the change in $\mathrm{m_f}$ number equal to zero. To do this, the polarisation of the light used must also be considered, a depiction of the allowed transitions for σ^+ polarised light is shown in figure 2.6. In co-propagating configuration this is achieved using the same circular polarisation ($\sigma^+\sigma^+$ or $\sigma^-\sigma^-$) for each beam. This method is insensitive to the motion of the atoms and so addresses more of the population, increasing the observed signal, but the sensitivity of the final interferometer will be low due to the small momentum transfer. For counter-propagating beams linear perpendicular (lin$\perp$lin) polarisation is used. This creates a polarisation gradient similar to that created in some sub-Doppler cooling methods consisting of σ^+, σ^- and π polarised light travelling in both directions. Choosing the magnetic bias field to be in the same direction as the Raman light field removes the influence of the π polarisation component. Only the $\Delta m_{\mathrm{f}} = 0$ and ± 2 two-photon transitions are allowed [63], although the $\Delta m_{\mathrm{f}} = \pm 2$ transitions are negligibly weak.

In order to perform an interferometry sequence, the Rabi frequency of this two-photon

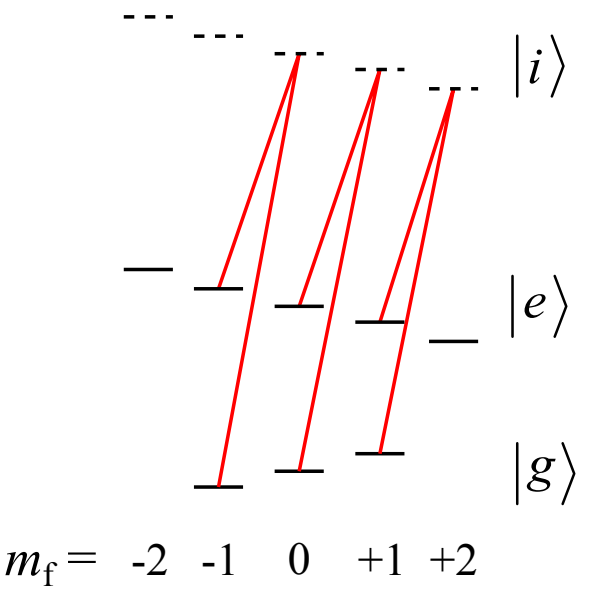

Figure 2.6: Allowed stimulated Raman transitions for σ^+ polarised light. Total change in the m_f number must be equal to zero. The m_f sublevels are shown to be non-degenerate as is the case if there is an applied magnetic field.

transition must be known as it defines the pulse length that needs to be used to prepare the atoms in either state. The Rabi frequency for a two-photon transition becomes [62]

$$\Omega_{\mathrm{eff}} = \frac{\Omega_\mathrm{e}^* \Omega_\mathrm{g}}{2\delta} e^{i(\phi_1 - \phi_2)} \tag{2.14}$$

with Ω_e and Ω_g being the separate resonant Rabi frequencies of the transitions from each hyperfine ground state to the intermediate state $|g, e\rangle \rightarrow |i\rangle$, calculated individually as in (2.6). δ is the detuning of the light from the intermediate level, as shown in figure 2.5. This detuning must be large, typically a few GHz, to prevent any spontaneous emission from the intermediate level.

The stimulated Raman transition is the tool with which we can now build our atom interferometer. A Mach-Zehnder interferometer [64] constructed for optical interferometry uses a beam splitter to send portions of a light beam along two paths, mirrors then redirect the two paths so that they overlap where they are recombined on another beam splitter. Any phase difference between the two beams at the point of recombination changes the distribution of the light intensity between the two outputs of the beam splitter. If the

light is in phase, the peaks of the light wave will overlap giving a maximum of intensity at one output, if out of phase a peak and a trough will overlap giving a minimum signal at the same output. The atom interferometer uses a $\pi/2$ Raman pulse as a beam splitter for atoms and a π pulse as the equivalent of a mirror.

2.2.3 Ramsey Interferometer

Ramsey's original method [9] that continued the work of his advisor, Rabi, used atomic beams and RF and microwave signals to perform interferometry for high precision spectroscopy of the hyperfine states within atoms. Using two $\pi/2$ pulses of microwaves tuned to the hyperfine splitting frequency, an equivalent of the classic Young's double-slit experiment can be realised. It is this method using microwaves that is used in the caesium atomic clocks that are the current frequency standard of the world.

The amplitudes of the Ramsey fringes are described by a function that shares a similarity with the optical double-slit description. The interference pattern observed at the output also exhibits narrow peaks contained within a larger envelope. For the Ramsey interferometer, the population in the upper hyperfine state at the output is described by [52]

$$|c_2|^2 = \left|\frac{\Omega\tau}{2}\right|^2 \left[\frac{\sin(\delta\tau/2)}{\delta\tau/2}\right]^2 \cos^2\left(\frac{\delta T}{2}\right), \tag{2.15}$$

with the sinc^2 function governing the larger scale envelope of the fringes and the $\cos^2$ function the width of the central fringe. Ω is the two-photon Rabi frequency. The width of the central fringe gives the precision with which the frequency of the transition can be determined. It is set by the separation time, T, between the pulses by

$$\Delta f = \frac{1}{2T}. \tag{2.16}$$

For example, in the caesium fountain clocks where the atoms are launched through a microwave cavity for timescales of around a second. When using an ensemble of a million

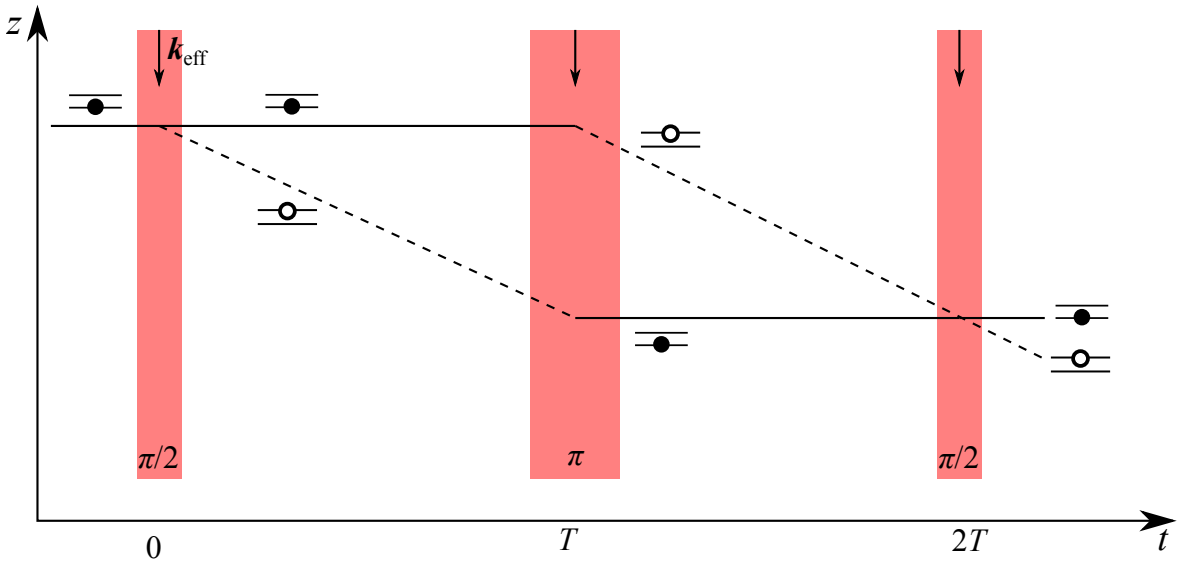

Figure 2.7: Drawing showing the process of a three pulse atom interferometer as first performed by Kasevich and Chu. The circles represent the atomic states on each path. The first $\pi/2$ pulse gives a momentum kick to half of the atoms, causing them to move away. The π pulse inverts this separation and the final pulse recombines the states. An interference pattern is then observed as population differences in the two output states.

atoms, this time is large enough to give a central fringe width of millihertz on a frequency of 10 GHz. This gives a fractional uncertainty on the frequency measurement of around $\Delta f/f = 1 \times 10^{-14}$. Repeating the measurement over time, this can be integrated down to $\times 10^{-16}$. Ramsey fringes can also be observed using a two-photon Raman transition with co-propagating light beams instead of microwave pulses.

2.2.4 Ramsey-Bordé Interferometer

To extend this to optical fields, a four $\pi/2$ pulse sequence was first used and described by Bordé [13, 65] in terms of quantum mechanical splitting of the wave packet across the different paths. The Ramsey-Bordé interferometer consists of four $\pi/2$ pulses of Raman light that transfer momentum to the atoms with a fifty percent probability. As such, two paths are created at the location of each pulse. By sending the final two pulses in the opposite direction to the first, the interferometer is closed and a measurement of population in each state can be observed at the output. In the Kasevich and Chu experiment [12], the central two $\pi/2$ pulses were replaced by a single π pulse that inverted

the populations and acted as a mirror would in optical setups, directing the two paths towards each other. In this case, all three beams are configured in the same direction. A schematic of the process is shown in figure 2.7 if there were no external forces acting on the atoms. The addition of gravity causes the straight paths that are depicted to become parabolic.

For the three pulse interferometer with a constant laser detuning, a phase is imprinted on the atom at each stage ($t_{1,2,3}$) since the atoms are moving with respect to the light field. At the output of the interferometer, the probability of finding the atom in the excited state is

$$|c_{e,\mathbf{p}+\hbar\mathbf{k}}(2T+2\tau)|^2 = \frac{1}{2}\left[1-\cos(\phi_{\mathrm{L}}-\delta\tau/2)\right] \tag{2.17}$$

in which ϕ_{L} is the phase imprinted to the atoms by the Raman laser at each pulse, given by

$$\phi_{\mathrm{L}} = \phi(t_1) - 2\phi(t_2) + \phi(t_3). \tag{2.18}$$

2.2.5 Measuring g with the Ramsey-Bordé Interferometer

The Ramsey-Bordé interferometer can be used for performing measurements of accelerations such as that due to gravity. The configuration in figure 2.7 is used in which the z axis is aligned vertically to the surface of the Earth. Equation (2.17) shows that the probability of finding an atom in the excited state can be chosen by varying the phase of the light pulses applied to the atoms. The addition of gravity causes the wavepackets in the interferometer to gain an additional phase that is different for each path. This leads to a total phase accumulation during the interferometer, due to both gravity and laser pulses, of

$$\phi = \mathbf{k}_{\mathrm{eff}} \cdot \mathbf{g}T^2 - \phi_{\mathrm{L}}, \tag{2.19}$$

where T is the total interferometer time and ϕ_{L} is the phase imprinted by the laser as given in equation (2.18). A gravity value is extracted from the interferometer by varying the phase of the final Raman pulse. This gives interference fringes at the output shown by the changing distribution of atoms in each state at the output. The value at which this laser phase exactly cancels the gravitational phase, meaning that all the atoms are in the lower state, is $\mathbf{k}_{\mathrm{eff}} \cdot \mathbf{g}T^2 = \phi_{\mathrm{L}}$ which gives us a value for gravity. This can also be determined by performing a frequency sweep of the Raman laser during the entire interferometer sequence, since the total phase can also be written as

$$\phi = (k_{\mathrm{eff}} g - \alpha)\, T^2, \tag{2.20}$$

where α is the frequency sweep applied to the laser. An interference pattern is observed by varying α and once again the point where $\phi = 0$ can be used to determine gravity [14, 66].

Equation (2.19) also shows that the phase due to gravity increases with a factor T^2. This means that the further that the atoms fall under gravity, the higher the sensitivity of the device.

2.2.6 Additional Measurement Schemes

In addition to the standard freefall interferometer scheme, the iSense apparatus was designed to be able to experiment with schemes that involve trapping the atoms inside an optical lattice. As mentioned previously, the Ramsey-Bordé interferometer sensitivity scales with T^2 and this can only be increased by allowing the atoms to fall under gravity for longer times. This requires larger vacuum chambers, substantially increasing the size of the whole device. The current extremes of this are the multiple 10 m scale atom interferometers being constructed around the world [1, 67, 68]. Lattice schemes have the potential to give the same or even better sensitivities in a greatly reduced volume. Three such schemes that iSense was designed to operate with are: a Bloch oscillation scheme, a Wannier-Stark ladder scheme and a combination of Ramsey-Bordé and Bloch oscillation

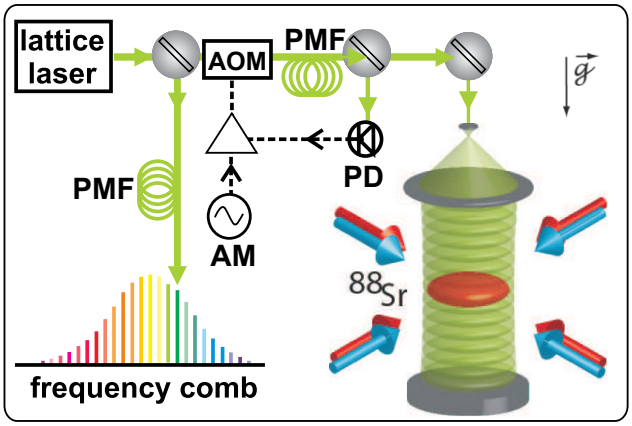

Figure 2.8: Schematic of the Bloch oscillation gravimetry scheme. Image from [70].

scheme.

Bloch Oscillation Scheme

The Bloch oscillation scheme involves loading a cold atom cloud into a vertical optical lattice and measuring the frequency at which they oscillate [69].

The atoms fall under the influence of gravity in the lattice. When they reach a momentum that matches with the reciprocal lattice vector, the atomic wave diffracts on the lattice. This returns them to their initial momentum state through an effective two-photon transition and the process repeats with a characteristic frequency called the Bloch frequency. This frequency depends on the local gravity and is given by

$$\nu_B = \frac{mg\lambda_L}{2h} \tag{2.21}$$

where m is the mass of the chosen atom, λ_L is the wavelength of the lattice light and h is Planck's constant.

In the experiment depicted in figure 2.8 by Poli et al. [70], 10^6 ^{88}Sr atoms at a temperature of 0.6 µK were loaded into a lattice at $\lambda_L = 532$ nm. The uncertainty on the value of the Bloch frequency obtained with this method was $\Delta\nu_B = 1.7 \times 10^{-7}$ leading to a fractional uncertainty in g of $\Delta g/g \approx 10^{-7}$. This value was achieved with the atoms

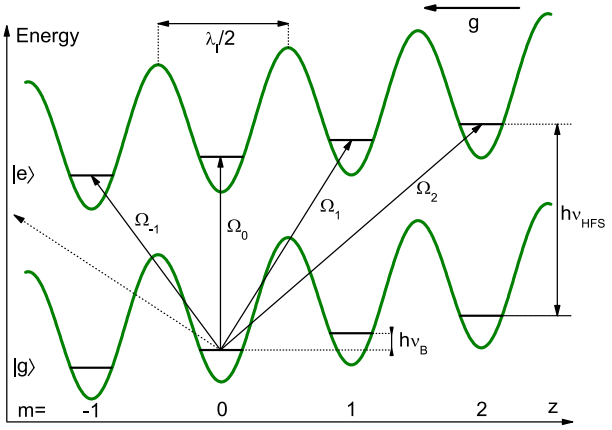

Figure 2.9: Wannier-Stark ladder of states. The Raman laser Ω_n, transfers atoms from the ground state to the excited state in different Wannier-Stark states separated by the Bloch frequency. Image from [71]

only falling by micrometre distances.

To determine the Bloch frequency, the velocity distribution is directly measured with absorption imaging after a period of freefall after switching off the lattice. Another method is to apply an amplitude modulation to the lattice. When the amplitude modulation is performed at an integer multiple of the Bloch frequency it causes the atoms to tunnel to neighbouring lattice sites, increasing the size of the cold atom cloud.

This method requires the use of sub-µK atoms to prevent the loss of atoms from the lattice when using large numbers of Bloch oscillations.

Wannier-Stark Ladder Scheme

The Wannier-Stark ladder scheme also involves holding the atoms in a vertical optical lattice. The oscillating lattice potential and the linear gravitational potential add to give a Wannier-Stark ladder of eigenstates. Each neighbouring state is separated by $h\nu_B$, the Bloch frequency multiplied by Planck's constant. Using Raman spectroscopy the tunneling between states can be observed.

Demonstrations of the method are detailed here [71, 72]. The Raman frequency is scanned and the transition probability is observed at each frequency. The peaks that are seen in the resulting spectrum are separated by the Bloch frequency and a gravity

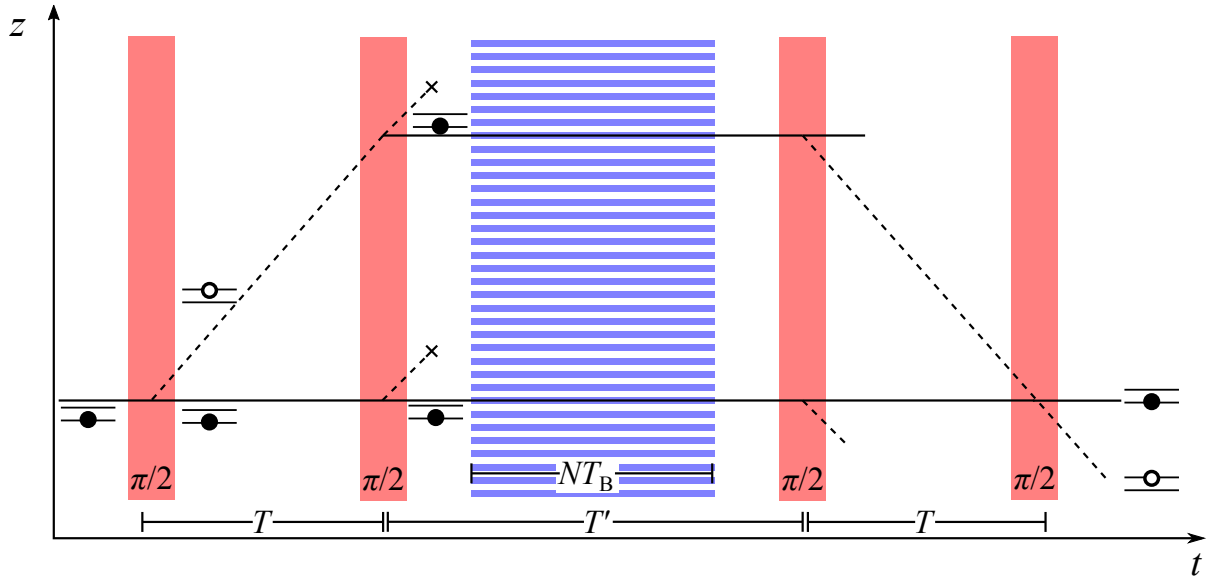

Figure 2.10: Combination Ramsey-Bordé and Bloch Oscillation scheme. The sequence uses the same four $\pi/2$-pulses as a Ramsey-Bordé scheme with the addition of a vertical lattice turned on for time NT_B, number of oscillations N multiplied by the Bloch period T_B. The atoms accumulate phase due to gravity by undergoing Bloch oscillations.

measurement can be obtained from this value in the same way as in the Bloch oscillation scheme, by using equation (2.21). The demonstrated uncertainty on the Bloch frequency with this method is $\Delta\nu_B/\nu_B = 2 \times 10^{-5}$ with the resulting value of $\Delta g/g$ having a similar precision.

Combination Ramsey-Bordé and Bloch Oscillation Scheme

Perhaps one of the most interesting developments in compact atom interferometry schemes comes in the form of a Ramsey-Bordé interferometer where the atoms are held in an optical lattice in between the two central $\pi/2$ pulses of Raman light [73]. The lattice allows the interferometer to accumulate phase due to gravity, meanwhile preventing the atoms from falling. The interferometry sequence is shown in figure 2.10; note that paths under gravity will be parabolic, not straight as depicted. After a vertical launch, an initial $\pi/2$ pulse splits the cloud along two paths and they are allowed to separate over time T. After this a second $\pi/2$ pulse prepares the atoms in the same state, although they are now spatially separated. The lattice is switched on for a time NT_B, where T_B is the Bloch period and

the atoms undergo N Bloch oscillations. The difference in lattice site causes a difference in the phase accumulated by the two clouds that is proportional to the gravity. The atoms are then recombined using two more $\pi/2$ pulses and the interferometer results recorded in the same way by measuring population differences.

In this method the gravity result is recovered in the same way as the Ramsey-Bordé interferometer described in section 2.2.4. There is now an additional phase contribution from the Bloch oscillation region of $k_{\text{eff}} 2N v_{\text{rec}}$ where N is the number of Bloch oscillations and v_{rec} is the recoil velocity of the lattice. This gives the total phase accumulated during the combination scheme of

$$\phi = (k_{\text{eff}} g - \alpha)\, T\, (T + T') - (k_{\text{eff}} 2N v_{\text{rec}} + \Delta\omega)\, T, \tag{2.22}$$

in which the Doppler shift due to gravity is cancelled out by a frequency sweep of the Raman laser at a rate α, and the phase due to the Bloch oscillations is cancelled exactly by a frequency jump of $\Delta\omega$. The sensitivity to gravity due to the Bloch oscillation period grows linearly with T'.

The lattice laser used in the source was 58 GHz detuned to the blue (higher frequency) of the $F = 2 \rightarrow F' = 2$ transition of the D_2 line in ^{87}Rb. In just 0.8 mm of freefall, an accuracy of $10^{-7} g$ has been observed [73]. There are also clear areas for improvement such as frequency stabilisation of the lattice laser and higher quality detection; improvements to these could easily bring this to $10^{-8} g$ or $10^{-9} g$. This scheme also has the advantage that high sensitivity can be achieved with just a microkelvin cloud rather than a BEC. The potential of this scheme led to the inclusion of ONERA as a project partner in the final year of the project to help transfer their expertise.

2.3 Summary

This chapter has presented some of the theoretical background of the project to aid with understanding of the design choices made in the following chapters. The principles of

the magneto-optical trap – and its extension to a mirror-MOT – have been described as the method used to generate a cold atom cloud that acts as the test mass in the system. The foundations of atom interferometry have been presented for performing inertial measurements using the prepared cold atom cloud. Finally, some alternative atom interferometry schemes based on atoms held in optical lattices have been discussed as a base for future investigations into further miniaturisation of cold atom sensors.

The next chapter introduces the physical components of the system and describes their importance in relation to the techniques that have been described in this chapter. The subsequent chapters then detail the integration of these into a portable cold atom interferometry system.

CHAPTER 3

EXPERIMENT SUBSYSTEMS

The main goal of the iSense project was to make a compact system with the lowest power consumption possible in order to show that cold atom experiments have developed far enough to be taken out of the laboratory and into the wider world. This aim was considered at every stage of the project and shaped everything from the choice of components to the design of the vacuum system. Some of our collaborators already lead the field in this through other projects [74]. FBH provide micro-integrated high precision laser diodes, UHH have knowledge of laser system packaging, and LUH design compact electronics. Joining all of this with the atom chip expertise of UNott, a truly portable device began to take shape.

This chapter gives a description of the components developed for the iSense project, and the chapter following outlines the characterisation and integration of components into the final device.

3.1 Rubidium-87

The choice of species of atom is important for the experiment since it defines almost all aspects of the setup – from the choice of laser to the microwave electronic components. In this experiment rubidium is our atom of choice, specifically the isotope of rubidium-87 (^{87}Rb). It has a number of advantages that make it suitable. Historically the use of rubidium stemmed from the fact that it has a useful two-level transition at 780 nm,

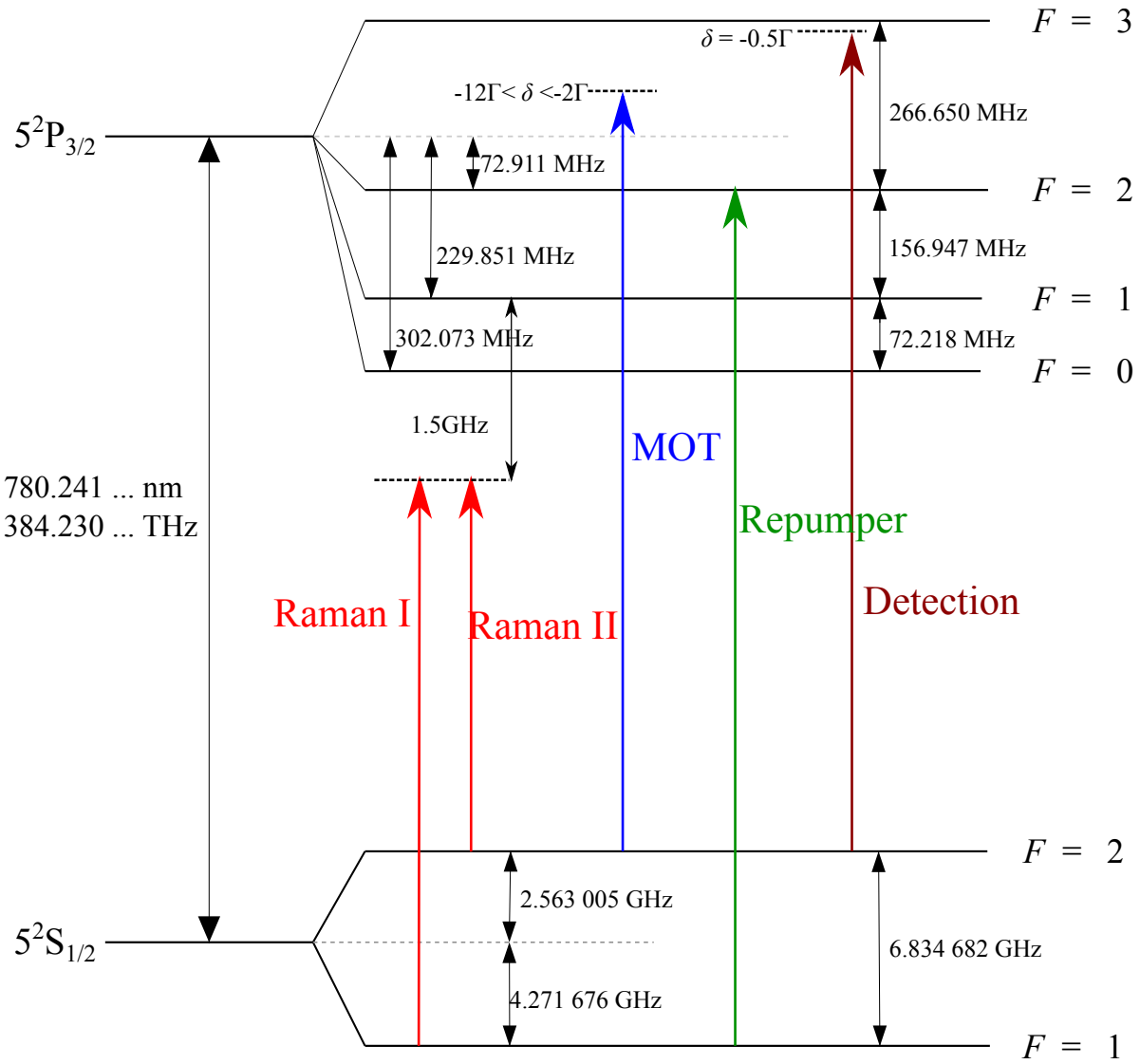

Figure 3.1: Rubidium-87 D_2 transition level diagram. Shown are the frequencies used for the lasers in the experiment and their detunings (δ) from the respective energy levels. Modified from [55].

around the wavelength of the laser diodes used in cd players. This meant that good quality lasers were cheap and widely available to scientists in the 1990s. Due to its single valence electron, its energy level scheme is relatively simple as it acts similar to a hydrogen atom. The hyperfine splitting of its ground energy level is at a convenient frequency of 6.8 GHz, allowing it to be addressed by microwaves or through a two photon Raman transition with two light fields separated by this frequency.

In ^{87}Rb the chosen transition is the D_2 transition between the $5^2S_{1/2}$ ground state and the excited $5^2P_{3/2}$ state that can be addressed by an optical wavelength of 780 nm. More specifically, the transition occurs between the $|F = 2\rangle$ hyperfine level in the ground state and the $|F' = 3\rangle$ level in the excited state, with a red-detuning of a few multiples of the linewidth Γ that has a value of $2\pi \times 6.066$ MHz [55]. Detection also happens on this transition, however the light is tuned to be on resonance.

Using a single laser to address this transition is not enough. Due to the multilevel nature of the atom, this is not a completely closed transition since the transition to each F level has a frequency width that takes a Lorentzian shape. This means that there is a probability that the atom will be excited into the $|F' = 2\rangle$ and $|F' = 1\rangle$ level, from where they can de-excite to the $|F = 1\rangle$ ground level. After this the atom will no longer be resonant with the cooling light field and is removed from the cooling process. This problem is overcome through the use of a second light field that we call a 'Repumper' or 'Repumping' field. This light is tuned on resonance with the $|F = 1\rangle \rightarrow |F' = 2\rangle$ transition from which the atom can return to the $|F = 2\rangle$ ground state.

The Raman transition used for the interferometry is performed with two light fields separated by 6.834 GHz – which is the separation frequency of the two ground states $|F = 1, 2\rangle$. The lasers are then red detuned from the transition to the excited state by a frequency of 1.5 GHz. The large detuning means that the atoms are not likely to be excited into the $|F'\rangle$ levels because this removes the atoms from the Raman cycle. It also creates additional photons from spontaneous emission as the atom de-excites that cause decoherence of the atom interferometer. This provides the intermediate level, which is

not populated, that allows the two-photon transition to occur. All of the frequencies used in the experiment are shown on a level diagram of the ^{87}Rb D_2 transition in figure 3.1 adapted from [55].

3.2 Vacuum System

The vacuum system was the first critical component of the experiment and the rest of the system is designed with this at its heart. A good vacuum is essential for trapping and cooling atoms as any collision with a residual gas molecule will immediately heat up the atoms – meaning that they are then lost from the trap. Reducing the background pressure reduces the number of these collisions that occur. Pressures below 10^{-8} mbar [1] are required for a MOT; BEC experiments reach as low as 10^{-12} mbar. One reason for this difference is due to the large timescales involved in the additional cooling methods such as evaporative cooling that take place over tens of seconds [75]. By comparison our entire experimental sequence is operated on a $0.5 - 1$ Hz repetition rate.

The iSense vacuum system was designed to be lightweight and compact, but with the flexibility to try out the variety of interferometry schemes mentioned in section 2.2.6. The final system consisted of three sections: the main chamber where the experiment takes place, the atom chip assembly for generating trapping magnetic fields and the pumping section used to maintain the vacuum pressure. The size of the chamber was chosen to give a maximum freefall time for the atoms larger than 100 ms that would allow for a best-case sensitivity to gravity using a Ramsey-Bordé scheme of $\delta g/g = 10^{-8}$. It also had to be compatible with the atom chip assembly, ensuring that the minimum of the trapping field and intersection of the cooling beams occurred at the same point.

Magnetic fields can affect the sensitivity of an atom interferometer as they cause additional forces on the atoms indistinguishable from gravity. To reduce this effect, all of the constituents of the vacuum system were chosen to be non-magnetic. The vacuum chamber itself was made from titanium, the holders for the optics were made from aluminium (as

[1] Atmospheric pressure at sea level and room temperature is 1 bar

were the structures for mounting them to the chamber and the structure holding the vacuum chamber), and the screws used for attaching the optics to the chamber were brass. The pumping section was made from 316LN steel as were the large bolts for fastening the vacuum chamber parts together. The atom chip assembly was also entirely non-magnetic even down to the custom flange it was mounted on. The chamber was designed in Birmingham and constructed by RIAL Vacuum. The total volume occupied by the vacuum system is 14.42 l (from the maximum extent: 213.2 mm × 330.2 mm × 204.8 mm). The total weight is just 10 kg, including the chip assembly and the ion-getter pump.

3.2.1 Atom Chip Assembly

A magnetic field has to be generated to add a confining force to the atoms, in addition to the cooling effect of the laser light, to generate the Magneto-Optical Trap. These are normally circular coils placed outside the chamber in anti-Helmholtz configuration and they require high electrical power to create the correct magnetic field gradients since they are so far away from the atoms. The high currents involved often mean that active cooling methods have to be employed to remove unwanted heat. These active cooling methods employ water or oil and, due to the need for reservoirs and pumping systems, require large amounts of both space and power to operate. Heat dissipation will be a problem as these devices get more compact.

Atom chips are capable of generating tight trapping fields close to the atoms and are routinely used to perform RF evaporation to cool atoms to BEC temperatures in record times [76, 77, 78]. A BEC is not required in iSense, but the concept of the atom chip was used to reduce the size and power consumption by placing the coils inside the vacuum and reducing the number of beams required from six to four for a mirror-MOT (see section 2.1.3). The cold atom cloud is typically formed 1-2 mm from the surface in atom chip experiments. For a Ramsey-Bordé gravimeter scheme the Raman beams have to propagate vertically. This means our atom chip assembly must be mounted in such a way that the chip surface is parallel to the vertical and the cold atom cloud forms in front

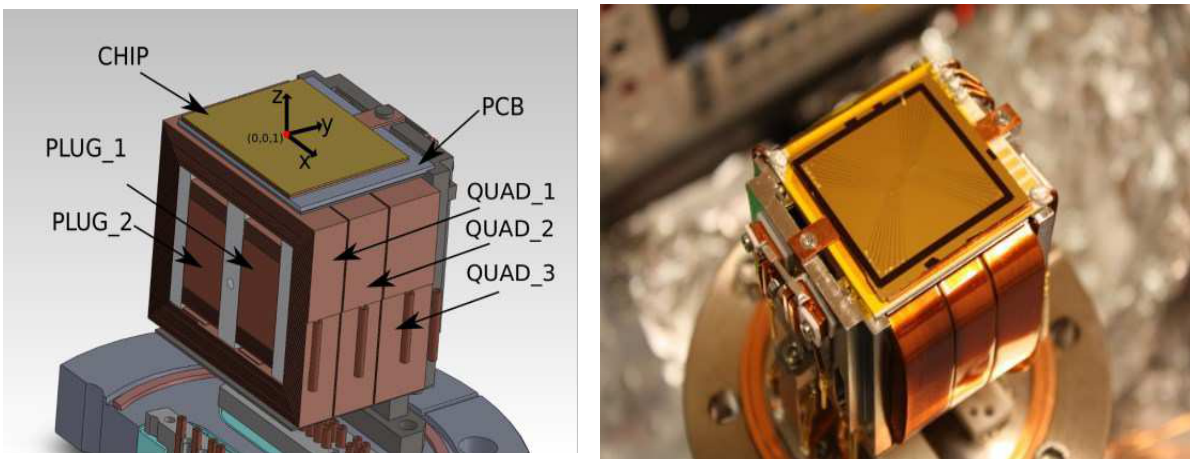

(a) (b)

Figure 3.2: (a) is a labelled CAD rendering of the atom chip assembly showing location of current carrying sections. The PCB layer contains two wire structures. (b) is a photograph of the atom chip assembly before integration into the iSense vacuum chamber. Visible are the rubidium dispenser on the left edge, three of the flat macroscopic wire coils for quadrupole generation and the gold mirrored surface. The DN63CF flange can be seen at the base. Both from Anton Piccardo-Selg [79].

of it. In this orientation, to prevent clipping of the Raman beam by the chip assembly, it was decided that the cold atom cloud must be formed at least 5 mm from the surface, strongly dictating the magnetic field generation requirements and thus the design.

iSense uses a custom atom chip assembly design from the University of Nottingham detailed in the thesis of Anton Piccardo-Selg [79]. To fulfil the system requirements of magnetic field generation that uses only 5 W of power, the first design consisted of a thick copper structure behind the chip surface that did indeed operate at 5 W. The assembly however achieved this at 100 A, which would be difficult to generate efficiently in a portable apparatus.

The second design was created with current requirements of less than 10 A per wire through the use of thinner flat copper wires wound into coils. Figure 3.2a is a cutthrough of a CAD rendering showing the details of the structures. The chip assembly consists of three adjacent coils of flat wire (QUAD1,2,3); the central coil (QUAD2) has the current flow in the opposite direction to the other two (QUAD1/3) to generate a 2D quadrupole field with the required 10 $\mathrm{G\,cm^{-1}}$ gradient near its minimum. Two additional coils (PLUG1,2)

can be used to plug the third dimension or apply a small homogeneous bias field in the x-direction. A five layer printed circuit board (PCB) is placed on top of the QUAD coils. This contains two wire structures (PCB_Plug and PCB_Z) that can also be used to plug the third dimension as with PLUG1,2, and apply an offset to the zero giving the 45 degree tilted, 3D quadrupole field at the required location from the chip assembly. It was found that these PCB structures were sufficient and so PLUG1,2 are unused. The final layer is the gold atom chip. It contains structures capable of performing purely magnetic trapping for cooling to near the critical temperature for BEC creation. In this system, however, it was solely used as a mirror for generation of the mirror-MOT. The gold provides a better than 99% reflection of two MOT beams at 45 degrees for this purpose.

A rubidium dispenser (SAES) is located on the assembly just next to the chip to provide a background gas of rubidium from which we can collect atoms in the MOT. While this helps in compacting the system and the electrical feedthroughs, it will be difficult to replace when it eventually runs out and will require removal of the entire assembly. However, in the 2 years we have been running it, we have not seen significant degradation in the number of atoms that it produces. For example, the current used to operate it began at 3.5 A and has just been increased to 3.6 A to keep the same MOT characteristics.

The final chip assembly can be seen in figure 3.2b mounted to a DN63CF vacuum flange with all required electrical feedthroughs. The flange is a custom construction which is entirely free from magnetic materials. The volume occupied by the completed chip assembly is approximately 7 cm $\times$ 7 cm $\times$ 7 cm.

3.2.2 Main Chamber Section

The main chamber section was constructed from forged grade 5 titanium (specifically the alloy Ti-6Al-4V) for its low magnetic properties, high strength and low density. The fact that the metal is forged is important as it makes a stronger material with lower porosity and trapped gases compared to the alternative casting method. The volume of the main

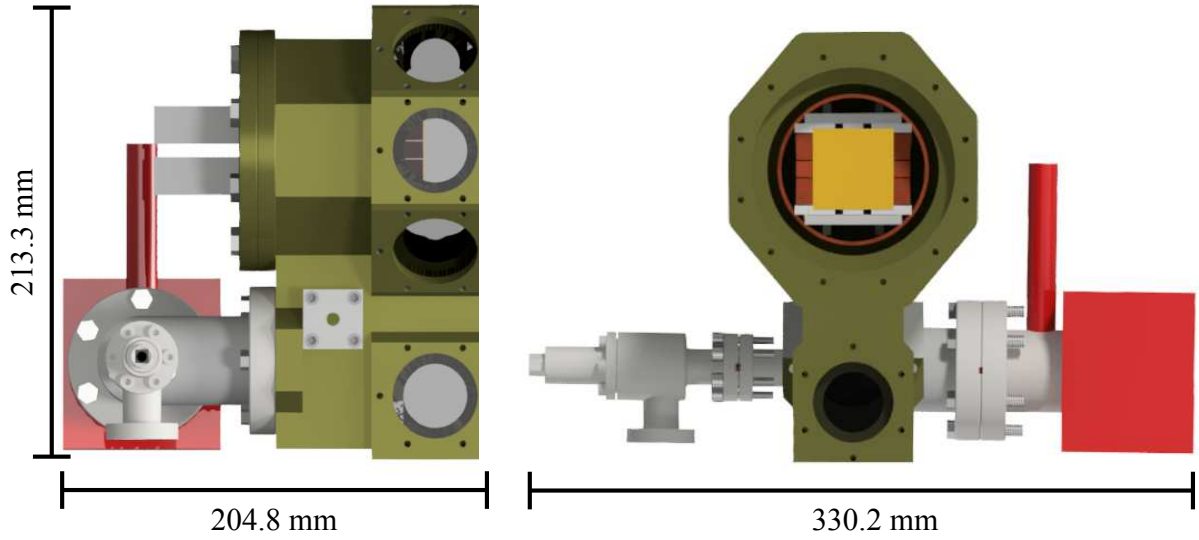

Figure 3.3: CAD drawing of the iSense vacuum system. The total mass including atom chip assembly is 10 kg and its volume is 14.42 l.

section is 3.5 litres with an evacuated volume of 0.9 litres. A complete rendering of the vacuum chamber is shown in figure 3.3. The design consists of an octagonal section with sides of 60 mm and a diameter of 125 mm in which the atom chip assembly is located and where the trapping, cooling and much of the interferometry takes place. Optical access in this section is provided by seven 40 mm windows on the sides, with a clear aperture of 30 mm, and a large 100 mm window, with a clear aperture of 85 mm, on the face of the octagon opposite the chip. A long rectangular section connected by a 35 mm diameter hole below this (on the eighth side of the octagon) is to be used for gravity measurements with a cubic detection section at the bottom. The centre of the cubic section is located 150 mm below the trapping region, giving a maximum freefall time of 170 ms. The cubic section has three 30 mm windows giving the option for both fluorescence and absorption imaging to take place and a final window on the bottom for the Raman beam.

All the windows are anti-reflection coated for 780 nm and mounted at an angle of 5° with respect to the wavefront of the beam. This was done to reduce interference patterns forming on the beams from reflections at the glass surfaces. They are specified for a flatness of $\lambda/10$. The two windows that the Raman light passes through at the top and bottom of the chamber are specified for $\lambda/20$.

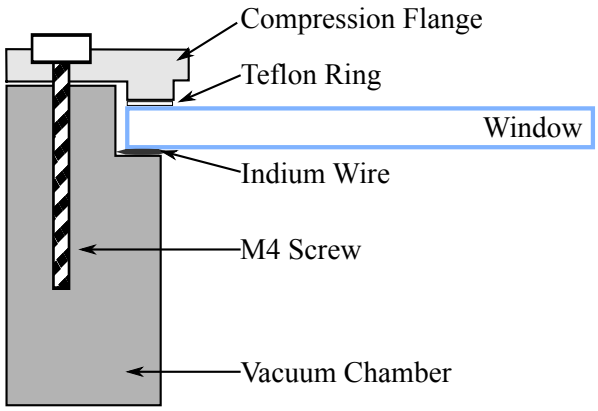

Figure 3.4: Diagram showing the indium sealing technique as implemented in this experiment. The compression flange, Teflon ring and screw are removed after baking, allowing the tapped holes to be used for mounting optics directly to the chamber.

The windows are held in place using an indium bonding technique shown in figure 3.4. A thin ring of indium wire (Goodfellow, purity of 99.999%) is placed between the chamber's titanium and the window, and the glass is then pressed onto the chamber using an aluminium flange with a teflon ring to prevent scratching the window. 1.5 mm diameter wire was used for the large window and 1 mm for all others. The metal surface under the window is milled flat – other sealing methods use knife edges [80, 81] – as this gives the best seal. Indium is a very soft metal, this means that as it is compressed between the window and the metal chamber it fills gaps and bonds the two surfaces together very tightly like a glue. This method does not require large flanges to be remaining after the compression phase, as is normal with other metal bonding techniques. As such it is a very compact way to assemble a vacuum chamber that also allows for optics to be easily mounted directly to the chamber. The seal can be removed by applying heat locally until it melts enough for the window to be removed; this is performed when the chamber is at atmospheric pressure.

3.2.3 Pumping Stage

In keeping with the idea of the compact system, the vacuum pump used was an extremely small and light NEXTorr D100 pump from SAESgetters – it has a combination of a Non-Evaporable Getter (NEG) and a small 6 l/s ion pump to give the same pumping as a

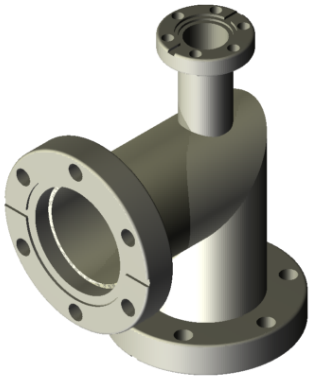

Figure 3.5: Rendering of custom tee designed to reduce the weight of the pumping stage of the vacuum system.

much larger 100 l/s ion pump in a package of just 2.2 kg. It is mounted on a DN35CF flange. A DN16CF valve is used to attach large pumps for the initial pumping down from atmospheric pressure and then for sealing the chamber when the pressure is low enough for the ion pump to take over. These two are connected to the main chamber with a custom tee shown in figure 3.5 that has two DN35CF flanges and one DN16CF flange. The custom tee section allows for the DN16CF valve to be used in conjuction with the pump and the chamber instead of a DN35CF valve. This saves 2 kg on the overall weight of the vacuum system. All of the seals in this section are provided by knife edges and copper gaskets.

3.3 Laser System

The next crucial constituents of a cold atom experiment are the light sources; they need to be stable with a well defined frequency (with a narrow linewidth) which does not drift over time. The lasers are used for the manipulation of the atoms and the readout of the measurement at the end of the experiment sequence.

iSense has four lasers: a master laser that is stabilised to an atomic spectroscopy signal, cooling and repumper lasers for the MOT and a final one for performing the Raman transitions. The cooling laser also doubles as the source of the detection light.

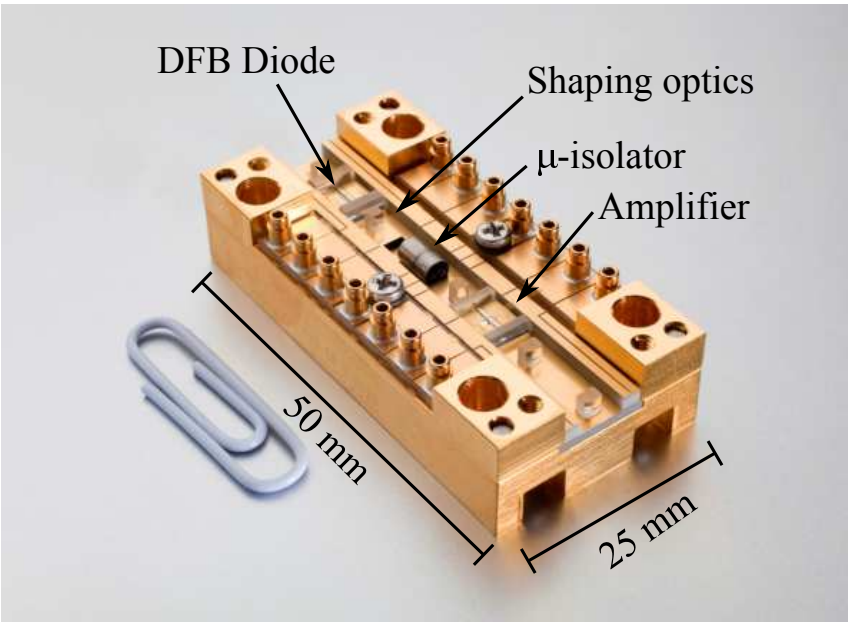

Figure 3.6: The micro-integrated DFB(-MOPA) optical bench used for the master, cooling and repumper lasers.

The lasers used are based on Distributed Feedback (DFB) laser diodes at 780 nm from the Ferdinand-Braun-Institüt in Berlin.

DFB and DFB-MOPA Lasers

The master, cooling and repumper lasers are all very similar in their requirements. Since their use is based on directly addressing an atomic transition that has a natural linewidth of $2\pi \times 6$ MHz the lasers should have a linewidth smaller than this. The DFB diodes used for the cooling and repumper lasers are 1.5 mm long ridge waveguide designs. They produce around 50 mW of optical power with a linewidth of 1 MHz. The master laser DFB chip was 3 mm in length giving a linewidth smaller by a factor of 1.5 [82]. The cooling laser is amplified to 1 W with a power amplifier (PA) that consists of a ridge waveguide-tapered amplifier chip.

The DFB diodes are integrated on compact optical benches made from copper and measuring 25 mm $\times$ 50 mm, as shown in figure 3.6. They contain a small optical isolator (Isowave, I-780-LM, µ-isolator [83]), a collimating lens and some beam shaping optics. The cooling PA chip is integrated on the same compact bench as the DFB diode to

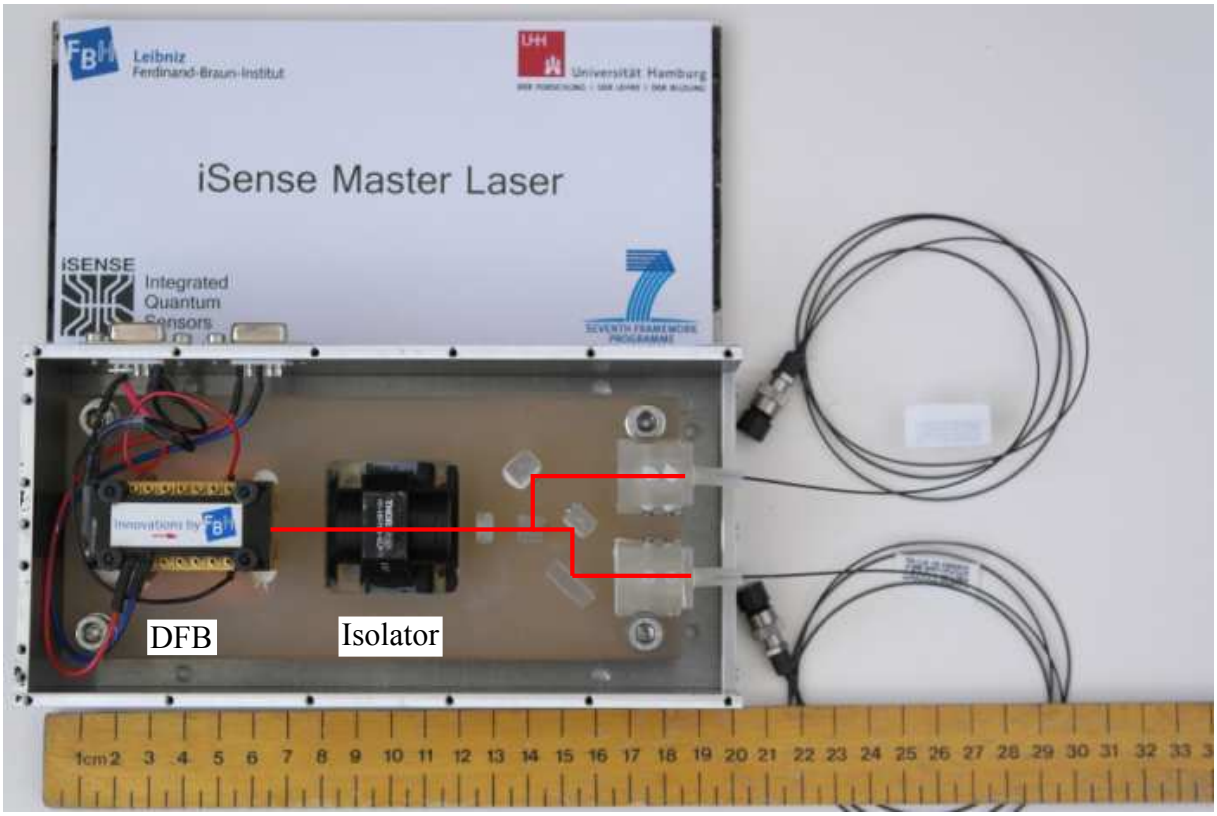

Figure 3.7: Assembled master laser with Zerodur baseplate and optics. Beam path is in red.

provide high stability.

For the cooling and repumper lasers this compact optical bench was mounted in an aluminium box, with a Peltier element between it and the box for temperature control. An additional optical isolator was then placed before a fibre coupler (Shäfter+Kirchhoff) that was attached to the outer panel of the box. For mechanical and temperature stability all the components are laid out in a linear fashion. Some initial fibre coupling was done during the assembly, but this was further optimised in Birmingham.

The iSense master laser, shown in figure 3.7, has two outputs, one to be used for a spectroscopy lock and the other for the offset locking of the other lasers to this. This means that it cannot be integrated in a linear way. In this case the low thermal expansion glass-ceramic Zerodur was used. Compact Zerodur based optic mounts and mounting techniques have been developed to perform this integration [84]. A Zerodur baseplate is used on which are mounted the laser, isolator, polariser, beam splitter, mirrors and

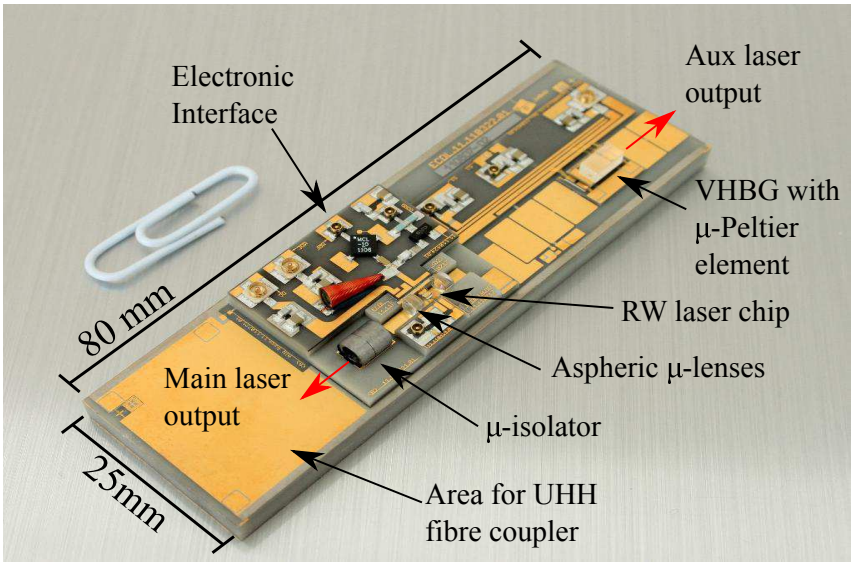

Figure 3.8: Micro-integrated ECDL used as the Raman laser.

Zerodur fibre couplers. Zerodur has such a low thermal coefficient that the baseplate used in the master laser would only expand by around 10 $\mathrm{nm\,K^{-1}}$. However, this also means that it is unable to dissipate the heat generated by the laser. Therefore the copper compact optical bench is only attached to the Zerodur baseplate at each corner. A hole underneath the centre of the optical bench holds a Peltier element, for temperature regulation, that is in thermal contact to the aluminium casing.

Micro-integrated ECDL

The requirements for the Raman laser are far more strict than for the other lasers. It should be as stable as possible and have a narrow linewidth to reduce the amount of spontaneous emission from atoms unintentionally excited into the $5^2P_{3/2}$ state. The high intensities typically used in Raman lasers to allow for short Raman pulses cause power broadening of the transition frequencies; a narrow laser has a lower probability of addressing this broadened transition. The DFB diode linewidth is governed by the length of the semiconductor cavity that produces the laser light; narrower linewidths can be created by increasing this length. It is neither feasible nor economic to construct large DFB diodes so another technique must be used. The decision was made to use a DFB as an External

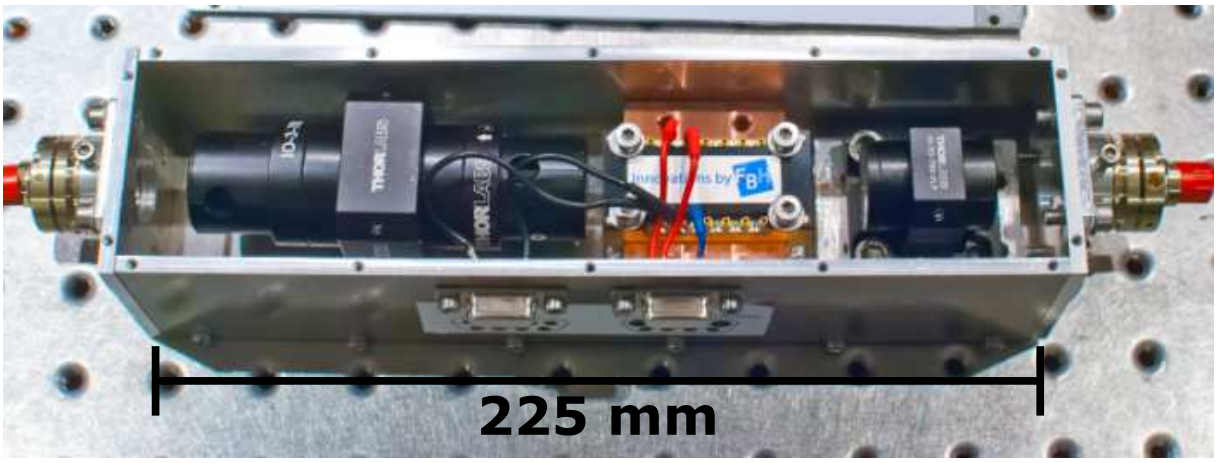

Figure 3.9: Photograph of power amplifier module. From left to right: Output fibre coupler, high power isolator, amplifier chip on copper baseplate, low power isolator and input fibre coupler.

Cavity Diode Laser (ECDL) in Littrow configuration [85] for the Raman beam. This configuration gives a much narrower linewidth than the DFB diode alone by extending the cavity length far beyond the extents of the diode.

In ECDL configuration, a Volume Holographic Bragg Grating (VHBG) is placed behind the secondary port of the DFB to create the external cavity [86, 87]. The wavelength output by the laser can be tuned by varying the temperature of the grating. This temperature variation changes the effective length of the cavity, thus changing the wavelength. The ECDL has an output power of 50 mW (before fibre) at a linewidth of less than 100 kHz. The ECDL was created using a 'next generation' integration concept compared to the DFB diodes for the other lasers. All the components, including a Zerodur fibre coupler, were mounted directly onto an aluminium-nitride bench measuring 25 mm $\times$ 80 mm as shown in figure 3.8. This was subsequently integrated into a smaller aluminium box than the other lasers since there was no need to add any further optics.

Power Amplifier Modules

To increase the amount of light in the Raman beam, two Power Amplifiers (PA) were used, the first being used to fully saturate the second. The PAs have an initial 2 mm long transverse mode section for mode filtering and preamplification followed by a 2 mm

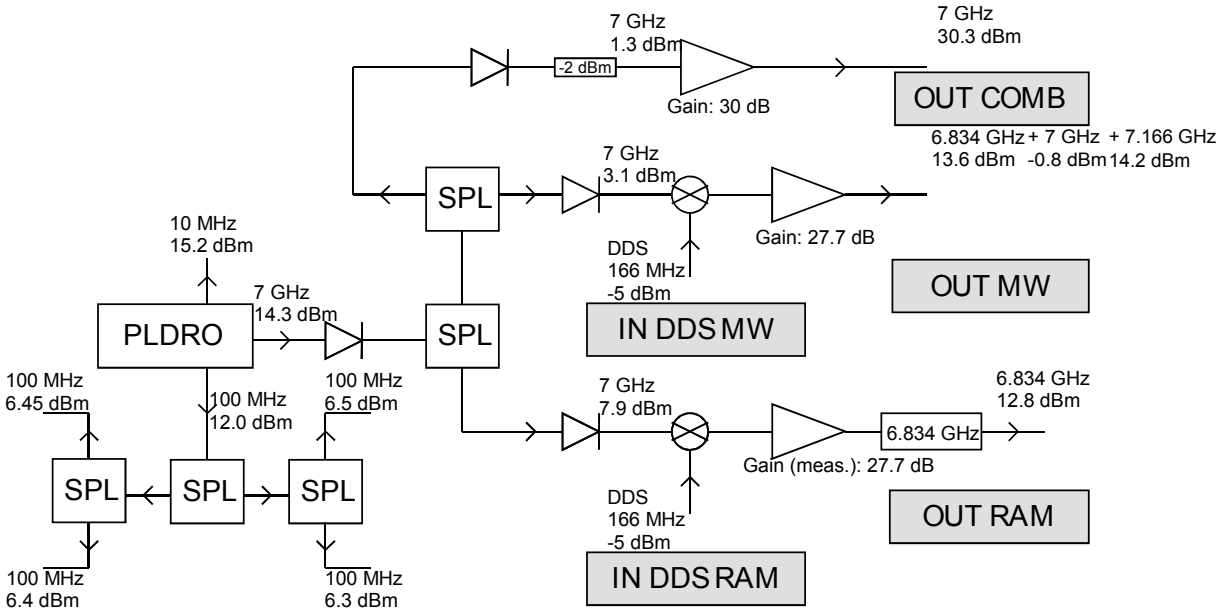

Figure 3.10: Schematic of the PLDRO microwave chain.

long Tapered Amplifier section to provide the majority of the amplification. These were mounted to a copper baseplate in the same way as the DFB diodes. This was placed in an aluminium housing, this time with optical isolators at both the input and the output with a fibre coupler at each end as in figure 3.9. The size of the power amplifier box, excluding fibres, is 225 mm $\times$ 50 mm. The linear design again was chosen to give high stability. The optical power after the isolator is around 600 mW.

3.4 Frequency Chain

To drive a Raman transition, two frequencies of light are required. These are generated by modulating a single laser with an electro-optic modulator (EOM) operating at the separation frequency of the hyperfine levels of the ground state of the atom. The advantage of the modulation method over using two separate lasers is that the two frequencies will always be in phase with each other as they are generated by the same source. Using two lasers would involve ultra stable phase locking techniques adding to the complexity of the system. In ^{87}Rb the frequency separation is 6.834 GHz and so we need a source that can provide this frequency to the EOM. Any variation in this frequency will cause a

change in the effective Rabi frequency of the Raman transition, leading to errors in the interferometry signal. This means that the frequency source has to be very stable.

A high stability frequency chain was produced at SYRTE based on a 7 GHz PLDRO (Phase Locked Dielectric Resonator Oscillator). It has three main outputs: a bandpass-filtered 6.8 GHz for generation of the Raman beams, another 6.8 GHz for use with a microwave antenna and a high power 7 GHz output for generation of large numbers of sidebands with an EOM in order to lock the Raman laser up to 49 GHz away from the master. This was included in the design for future operation of interferometry schemes involving lattices that are aided by large detuning to reduce scattering.

The 6.834 GHz outputs are generated by mixing a 166 MHz signal from a DDS with the 7 GHz signal. This allows us to tune the output frequency very precisely using the DDS. It also means that complex frequency sweeps and jumps of the Raman frequency can be performed by a computer controlled fast DDS. The system also has multiple 100 MHz outputs from various stages that can be used as timing signals to synchronise other electronics in the system. The frequency chain is mounted in a 19 inch rack case. It has aluminium walls of 2 mm thickness to block microwave signals that could leak out and affect the surrounding electronics.

3.5 Electronics

The final major reduction in size was achieved by using electronics that were developed for the LASUS and QUANTUS projects. They have the advantage of being a modular card-based system where each board has a specialist function, all working together to control every aspect of a cold atom experiment. The operating principle of the electronics is shown in figure 3.11. A user-friendly LabVIEW program communicates with the boards through a PC104 interface module containing an FPGA dedicated to synchronising the timing of all the operations of the boards. This allows realtime operation of experimental sequences with high precision timing.

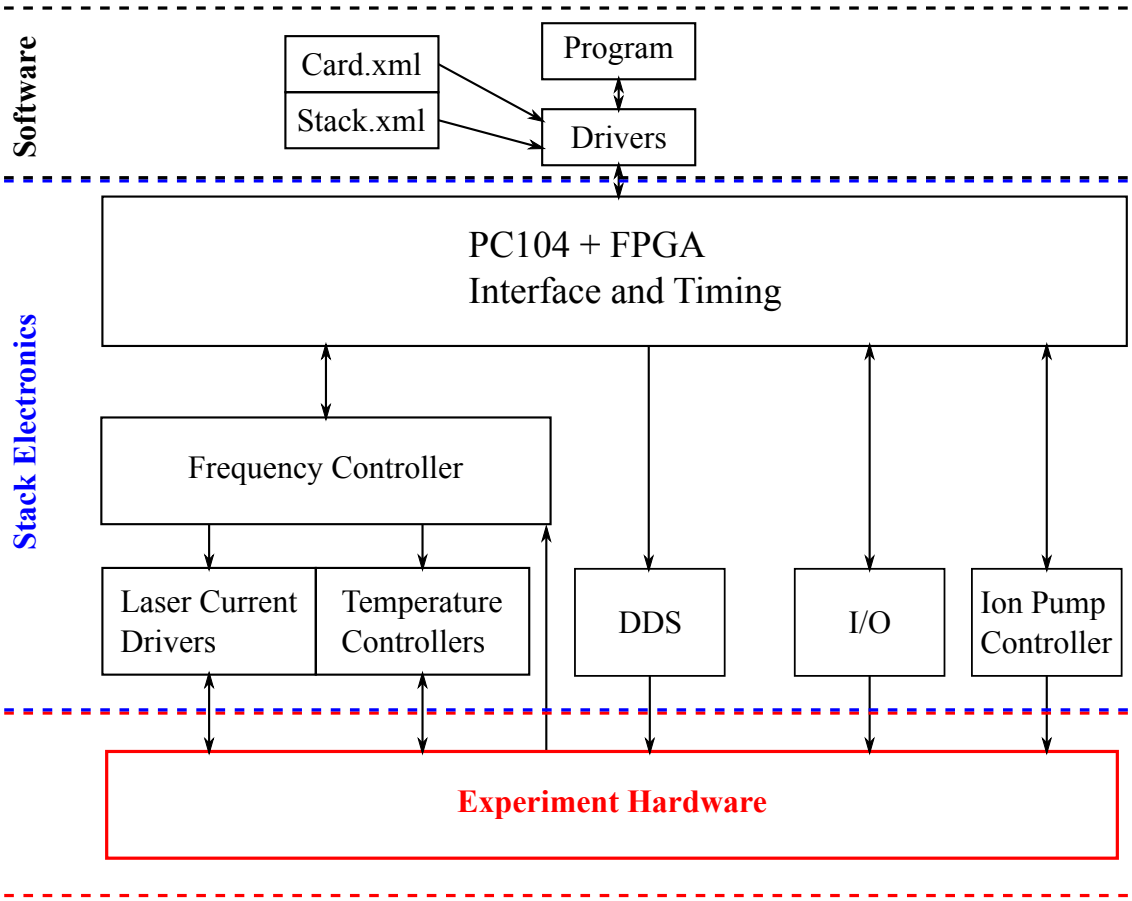

Figure 3.11: Operating schematic of the stackable electronics.

Stackable Electronics

The electronics used are based on PC104 standard 100 mm × 100 mm boards and they have two connectors, one with 64 pins called the 'Digital Connector' which carries the communication signals, triggers and power the boards, and the other a 32 pin 'Analog Connector' that carries the current correction signals between the frequency controller and laser current driver boards to stabilise the lasers. These connectors give each board a minimum height of 17 mm which most boards adhere to, the one exception being the ion pump controller which has a double height due to the high voltage components used.

The FPGA interface board is the master that controls the timing of the other boards through the internal bus, through external digital trigger signals it is also used to trigger the RF switches, fibre switches and the CCD camera of the experiment.

The frequency controller board performs the locking of the lasers and is capable of changing and sweeping their frequencies. It is able to frequency lock one laser to a modulation transfer spectroscopy signal using onboard modulation and demodulation and up to three others with offset locking. Photodiode signals are input and all processing is done digitally by the board. This allows for arbitrary locking of the lasers on any point of the spectroscopy signal. This board connects to the laser current drivers through the analog connector and modulates their current outputs to keep the lasers at the correct frequency. It is capable of frequency jumps and sweeps, and can also be triggered with the FPGA to perform sequences of frequency changes such as applying detunings for optical molasses, or removing them for detection.

iSense used five laser current driver modules that had outputs for two lasers or PAs. The maximum current could be changed physically but normally one was set for high current up to 2 A as required for PAs and the other 300 mA for DFB diodes. Modulation of the laser diode frequency was done by connecting the required controllers to the frequency controller board through one of four pins on the stack analog connector.

Temperature controllers are used to regulate the temperature of the laser diodes. Slow, broad wavelength tuning of the diodes can be done by changing the temperature. Due to

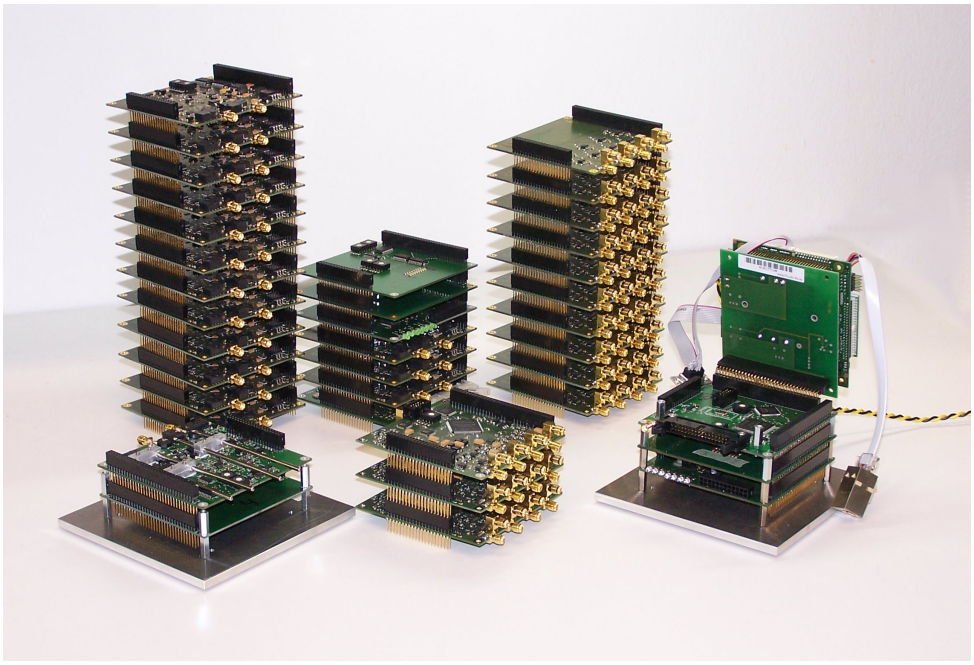

Figure 3.12: Photograph of a sample of the stackable electronics used in iSense, courtesy of Thijs Wendrich.

their importance and their risk of damaging the laser diodes if they ran out of control, they are mostly analogue circuits with only the ability to switch the output currents on and off, and report temperature readings to the computer.

An analog out board is used to send voltage signals to run the chip current drivers. As with other boards, a sequence of changing values can be programmed in and triggered via the stack. It was also designed to control the integrated waveguide structures being developed under iSense at the University of Nottingham. Two DDS boards are used for controlling the Acousto-Optic Modulators. Each has two frequency outputs and are able to perform sequences containing frequency jumps and sweeps. The IonGetter controller simply outputs a 5 kV supply for the NEXTorr pump. A sample image of some boards and how they fit together can be seen in figure 3.12 and – apart from the RF amplifiers for the offset lock and the current drivers for the chip assembly – contain all the electronics needed to run a cold atom interferometry experiment in a volume of 10 litres, by comparison this is less than a 2U 19-inch rack case that has a volume of 13 litres.

Chip Current Drivers

The magnetic fields created by the atom chip assembly are controlled by the current that is flowing through them. High stability current drivers were therefore necessary to generate these fields and have them be stable. The chip current drivers are of a similar design to the stack electronics, in that they are also modular and stackable, however they are capable of operating at the high currents required. This additional stack occupies 6 litres. The current output is controlled using the voltages provided by the analog out boards of the main stack. 1 V at the input gives 1 A output current; the drivers are capable of providing currents between -10 A and 10 A. There are adustable potentiometers to zero any offsets and for setting the three PID parameters which have to be set up for each individual coil. These PID settings were tuned for operation with our chip assembly to give the correct current per voltage and also for optimal switching times with no oscillations. Oscillations in the current through the coils cannot only cause unwanted fields to build up inside the chamber, but could also damage the current drivers. The best switching speed of the coils was found to be less than 1 ms.

3.6 Future Additions

During the initial phase of the project, a number of novel technologies were planned to be included to improve the portability of the device even further. These include optical waveguides that would be used to shrink the entire optical system to a chip-scale device, and a micro-integrated spectroscopy module to be used for stabilisation of the master laser in a compact fashion. The plans are outlined below with the hope that these will be implemented in further iterations of the project, the spectroscopy module in particular should be available in the near future.

3.6.1 Integrated waveguides for light delivery

The delivery of the light from the lasers to the inside of the vacuum chamber uses fibre optic components including fibre coupled AOMs, EOMs and switches. While already much smaller than using free space optics, further reductions can be obtained by using optical waveguide structures with the goal of having the entire optical delivery system on a chip scale. These structures are common for wavelengths of light used in telecommunications, however 780 nm versions are being developed based on aluminium gallium arsenide (AlGaAs) material. Active components include voltage controllable Multimode Interference (MMI) sections for fast light switching to replace the AOMs, and passive Mach-Zehnder Interferometers (MZI) to distribute light instead of using fibre splitters. Originally being developed by the company QinetiQ, development was transferred to the University of Nottingham in 2012. These devices are still under development at the time of writing due to delays caused by the transfer of responsibility, and higher than predicted optical losses observed in initial samples meaning that new mixtures of the AlGaAs substrate materials have to be investigated. Low optical power damage thresholds of less than 100 mW were also observed and have to be fixed in the future. Some initial wafers designs are described here [88].

3.6.2 Micro-integrated Spectroscopy Module

The lasers need to be stabilised to a fixed, well defined frequency. One method to achieve this is to observe an atomic transition through spectroscopy with the laser and constantly make adjustments to the laser to continue to observe this transition. Using their expertise, FBH have designed a micro-integrated modulation transfer spectroscopy setup for iSense in order to carry this out. The design can be seen in figure 3.13 – it contains a miniaturised phase modulator [89] a small rubidium cell and compact optics and photodiodes. Everything is mounted on an AlN baseplate that is slightly larger than that used for the ECDL at 30 mm $\times$ 80 mm. Delays in construction have prevented this module from being integrated within the scope of this work.

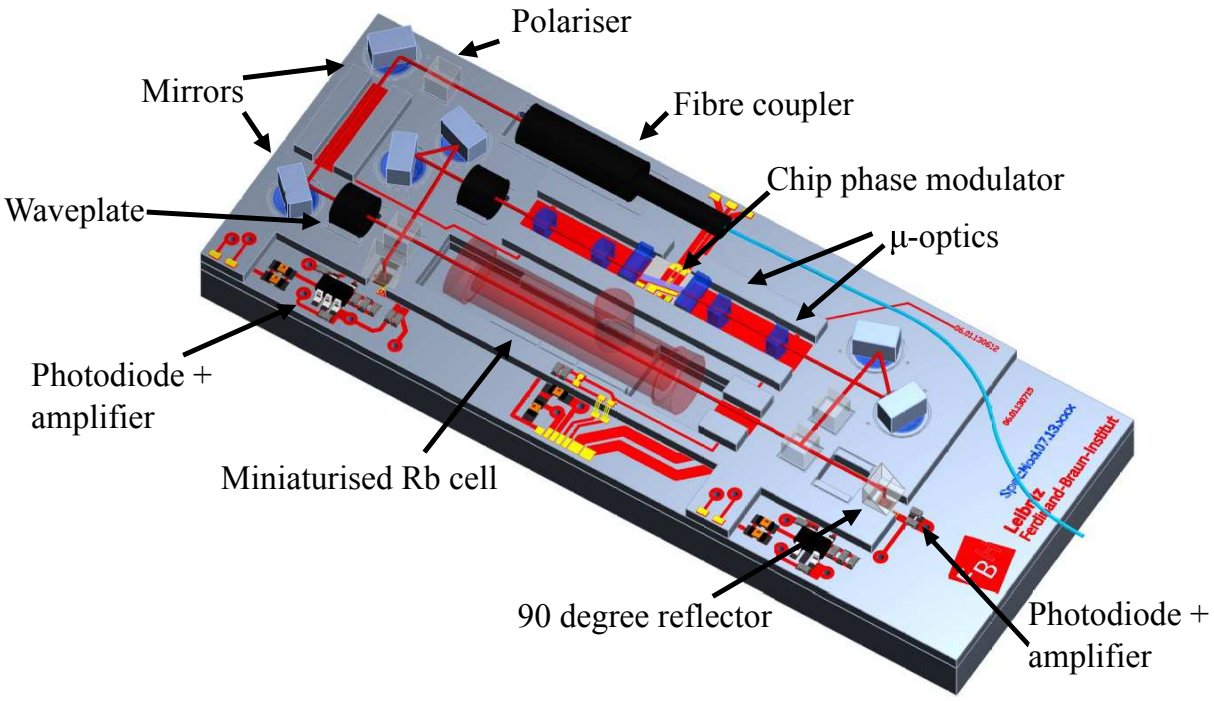

Figure 3.13: The proposed micro-integrated MTS setup from FBH includes miniaturised phase modulator, rubidium cell, optics and photodiodes. Its dimensions are only 30 mm × 80 mm.

3.7 Summary

In this chapter the major components of the experimental system have been described along with their uses and the reasons behind their technical specifications. The design of the vacuum chamber was chosen in order to carry the low power atom chip assembly and also to accommodate a variety of interferometry methods. The diode lasers were used for their proven robustness and stability in harsh environments – the stack electronics for the same reason. The frequency chain was developed to provide an ultrastable 6.834 GHz source for the Raman laser.

The following chapters will detail the characterisation of these components during their integration into a working cold atom system, that is capable of operating both in the laboratory and also after transportation.

CHAPTER 4

COMPONENT INTEGRATION AND EXPERIMENTAL SETUP

As the components described in the previous chapter arrived throughout the course of this project they were integrated when possible, gradually adding features to the system. The author spent time at LUH working on the QUANTUS-II project, an established compact cold atom system, to assist in the advancement of the device and to gain experience about the interface requirements of such a complex system, which shares similarities to iSense [90].

The first stage was work towards generating a mirror-MOT. The first components to arrive were the vacuum chamber and the individual fibre components. Testing and characterisation of these components was then carried out. The atom chip assembly was next to arrive and – while the vacuum system was being baked and pumped down after installing the chip assembly – the fibre components were spliced together into the final system. This allowed the generation of a MOT using commercial lasers and amplifiers (Vortex II and VAMP, New Focus) with their electronics to test the vacuum system with the atom chip assembly and the completed fibre system.

The commercial lasers used for cooling and repumping were then replaced with the more compact counterparts from FBH with some of the LUH electronics for current driving, temperature control and offset locking, keeping one to use as the master laser. After the MOT was achieved, it was then optimised and characterised before focus switched to

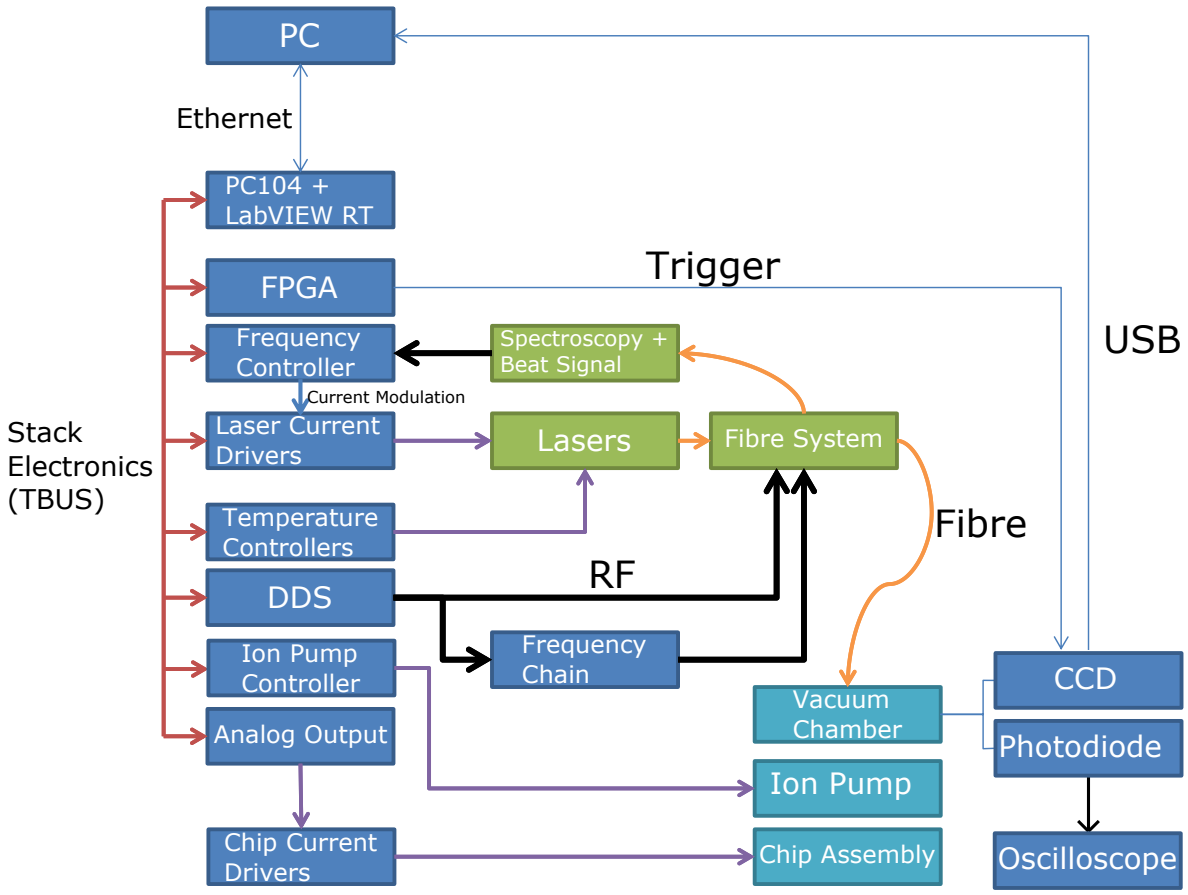

Figure 4.1: Schematic diagram of experimental setup, with the lines showing the connections between the elements. Red is the TBUS communication between the stack electronics. Black is RF and microwave signals, orange is optical fibres and purple is DC currents and voltages. Other connections are triggers, USB for the CCD camera and Ethernet for control of the electronics via a PC.

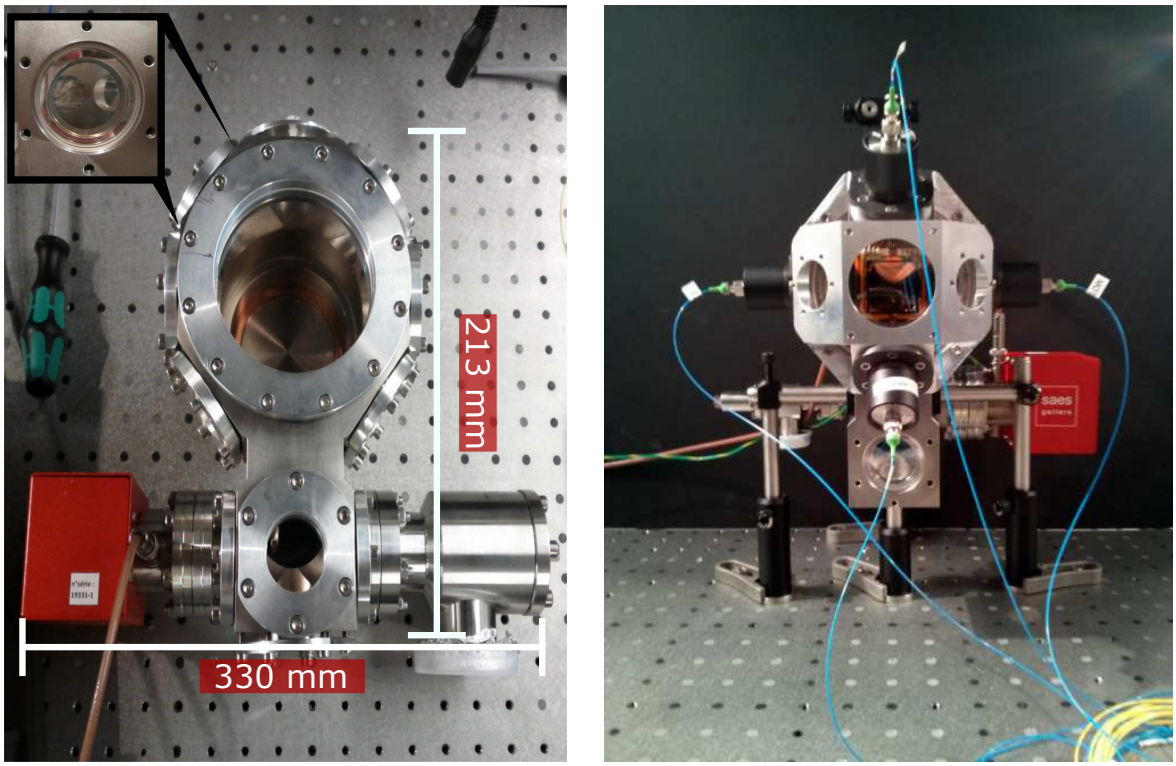

(a) (b)

Figure 4.2: (a) iSense vacuum chamber as delivered without atom chip assembly and with compression flanges still attached. Inset shows indium-sealed window without compression flange. (b) Photograph of completed iSense vacuum chamber, including atom chip and telescopes for delivering the cooling light.

integrating the Raman system and generating the first interferometry signals. The master laser was added after the first interference fringes were observed and was used during the portable operation in chapter 5.

Figure 4.1 shows a schematic diagram of the entire system and how each component is connected. The PC acts as the interface between the user and the PC104 electronics; it is from here that the settings and sequence are programmed. The stack electronics can run the experiment independently once programmed, but image analysis from the CCD currently takes place on the PC due to its higher storage and processing capabilities.

4.1 Vacuum Chamber and Atom Chip Assembly

The first major component to arrive was the vacuum chamber. It arrived in Birmingham from IOGS under vacuum with the windows sealed using indium wire and their compression flanges still attached, a blank flange was placed where the atom chip assembly was to go. Upon turning on the IonGetter pump, a vacuum of around 10^{-10} mbar was achieved after tightening a single bolt showing that it had survived transportation without damage. The vacuum system as it arrived in Birmingham is pictured in figure 4.2a without the chip assembly and with the compression flanges still attached to the windows.

Once the atom chip assembly arrived, we installed it in the chamber. This involved venting the chamber to air, removing the blank DN63CF flange and sliding the chip assembly inside, taking care to ensure the orientation was correct and that none of the wires touched the chamber itself. The flange was sealed using a copper gasket and M8 316LN steel bolts.

After reassembly, the entire system was baked at 80 °C for two weeks while pumping with a Pfeiffer Turbopump. Baking the vacuum chamber is done to remove gas that is trapped in the bulk of the material during manufacture, in order to achieve ultra low pressures inside the chamber. All the individual components had been previously baked under vacuum but the process of venting the chamber to air in an uncontrolled environment introduced air and dirt to the vacuum system, including anything that the chip assembly gained in transportation. The baking temperature of 80 °C was much lower than those typically used but it was necessary to prevent the structures on the chip from melting; the indium seals have a melting point of around 150 °C so temperatures near to this were not used. The original DN34CF size tee-section and valve were also replaced with a custom design made from 316LN steel, allowing for a smaller DN16CF valve to be used, reducing the mass of the system by 2 kg.

After the baking was completed, the valve to the turbopump was closed and the ion pump turned on. The pressure initially showed 10^{-8} mbar that reduced to around 10^{-9} mbar after a single activation of the getter section with a high current source. We

Wire	Current (A)	Voltage (V)	Power (W)
QUAD1/3	6.9	0.7	4.83
QUAD2	2.97	0.2	0.594
PCB_Z	2.82	0.2	0.564
PCB_PLUG	2.02	0.2	0.404
Rubidium Dispensers	3.62	0.7	2.534
Total Power			**8.926**

Table 4.1: Table of values of the current supplied to the chip assembly to obtain the MOT. The total power used in the magnetic field generation was 6.4 W. When including the dispensers this rises to 8.9 W.

could not achieve the same pressure reading of 10^{-10} mbar as before, most probably due to the large surface area of the chip assembly coils and the outgassing due to the materials it is made from. However, lower pressures than this bring no additional benefit for our system, since the atoms will be loaded into the MOT from a background vapour of rubidium at a similar pressure.

To save size and weight, the iSense chamber has no dedicated vacuum gauge. The pressure measurement comes from the output current of the ion pump controller with a conversion given by

$$P = \frac{(0.066 \times I \times (5600/V) \times 1.33)}{\text{PumpSize}}, \tag{4.1}$$

where $V = 5$ kV and PumpSize $= 6\,\mathrm{l\,s^{-1}}$. Due to the difficulties in measuring currents on the nanoamp scale and leakage currents the value is not precise, but it does give a good order of magnitude estimation. The numbers were shown to agree with data taken using the cold atom cloud to check the pressure, these can be seen in section 6.2.3.

The final power consumptions of the chip assembly can be found in table 4.1. These are the values found experimentally when searching for the magneto-optical trap – they are quite consistent with the values measured in Nottingham before integration in the iSense chamber. These measurements are the values given when the wires are connected directly to simple power supplies and thus are indicative of the power drawn only by the chip assembly and not in the current generation. The total power used to generate the magnetic fields was just 6.4 W, with a further 2.5 W used to run the rubidium dispensers.

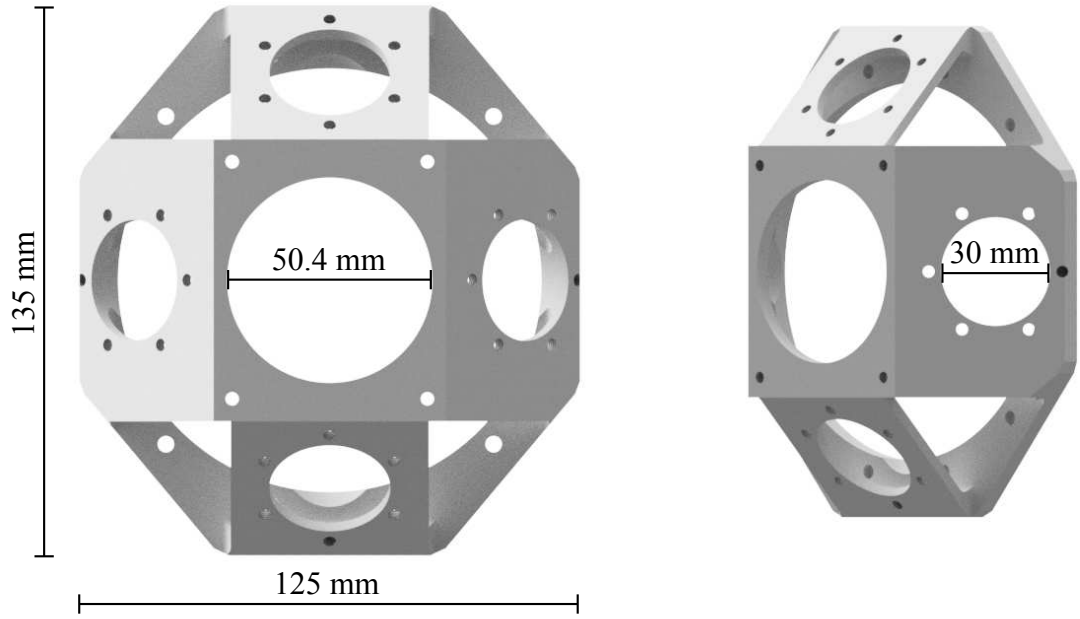

Figure 4.3: Render of mount for attaching optics in front of the large window of the vacuum chamber. The upper and lower positions are for the 45° reflected MOT beams. The horizontal holes are used for mounting the optics for detection.

In comparison, 3D MOT setups used by other experiments in the research group typically need 80-100 W of power to run their magnetic coils.

A structure for mounting optics was designed in aluminium (shown in figure 4.3) and attached directly to the chamber in front of the large window. The two reflected Mirror-MOT beams are attached to this on opposing angled faces, as are the detection beam and CCD camera; the holes are 30 mm in diameter. The large central hole is used for absorption imaging in order to collect the largest amount of fluorescence light possible. The assembled vacuum system with the cooling telescopes attached can be seen in figure 4.2b.

Magnetic field from Ion Getter pump

The ion-getter pump has two permanent magnets attached to it that are required for its operation; these are placed either side of the pump on faces perpendicular to the opening

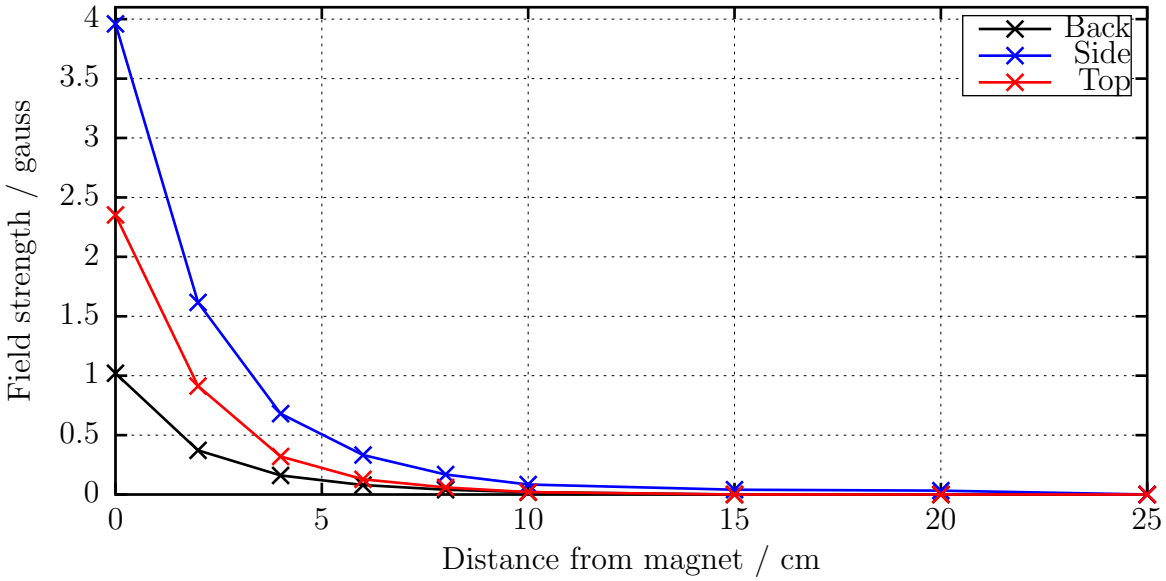

Figure 4.4: Measurements of the magnetic field generated by the permanent magnets of the ion-getter pump.

to the chamber. Magnetic fields can affect precision measurements, so the strength of the field from the magnets was measured using a Hall probe to determine if there would be a cause for concern in this compact system. The results of the measurement are shown in figure 4.4. The field was measured in three directions: the back, opposite to the chamber opening; the side, the axis between the two magnets; and the top, the direction vertical to the axis between the magnets. The measured field from the sides of the pump were the most powerful, reaching 4 gauss at the surface. The fields decay to the room background between 10 cm and 15 cm, the atoms are further than this from the pump magnets and so this should not cause a problem.

4.2 Laser System

The complete design of the laser system is drawn in figure 4.5. There are four lasers and a spectroscopy module for frequency stabilisation to an atomic transition. The light is carried to the vacuum chamber in an entirely fibre optic system, with fibre AOMs and fibre switches used for redirection and intensity control which is described in section 4.3.

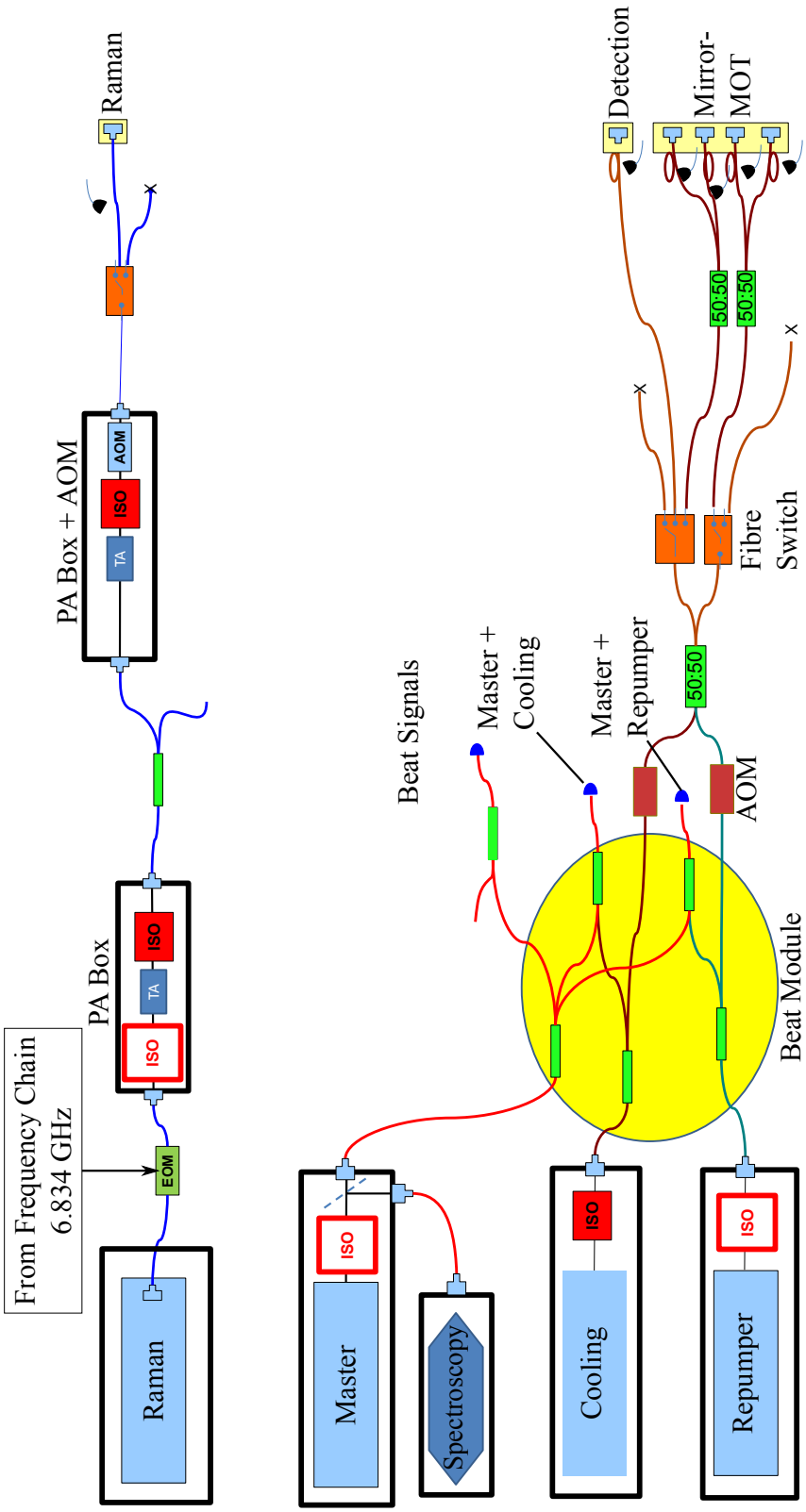

Figure 4.5: Diagram of the complete laser and optical delivery system for iSense.

Master Laser

The master laser was operated at 230 mA and at a temperature of 30 °C giving around 10 mW of power in each of the two output fibres. One output was used for a spectroscopy lock, and the other was used for generating beat signals with the other lasers for offset locking. Due to its design all parts are glued to a Zerodur base and so there can be no simple adjustments – a recoupling had to be done to return to the same power levels in the fibres after there was an issue with a temperature controller. Recoupling involves heating the parts until the glue is pliable and then making the adjustments before it sets.

Cooling and Repumper Lasers

The cooling and repumper lasers worked out of the box with only minor adjustments needed for the coupling of the light into the fibre delivery system. About 300 mW of cooling light was coupled into the fibre system and 20 mW of repumper light. The laser current and temperature settings that give the required output frequencies were then determined by observing the beat signal between them and the frequency locked master laser using a spectrum analyser. The operating temperature was found to be $T \approx 38$ °C for both lasers and the currents 131.4 mA and 184.2 mA for the cooling and repumper lasers respectively.

Both laser boxes were attached to an aluminium baseplate to allow good heat conduction and easy mounting to the optical table before being moved to the baseplate of the iSense apparatus.

Raman Laser

The ECDL is coupled into a fibre using a Zerodur fibre coupler glued directly to the micro-optical bench. This is then connected to a fibre electro-optic modulator (EOM) (PM-AV5-40-PFA-PFA-780, EOSPACE Inc.) that is used to add sidebands at 6.8 GHz from the centre so that the two required Raman frequencies are in the same fibre. The

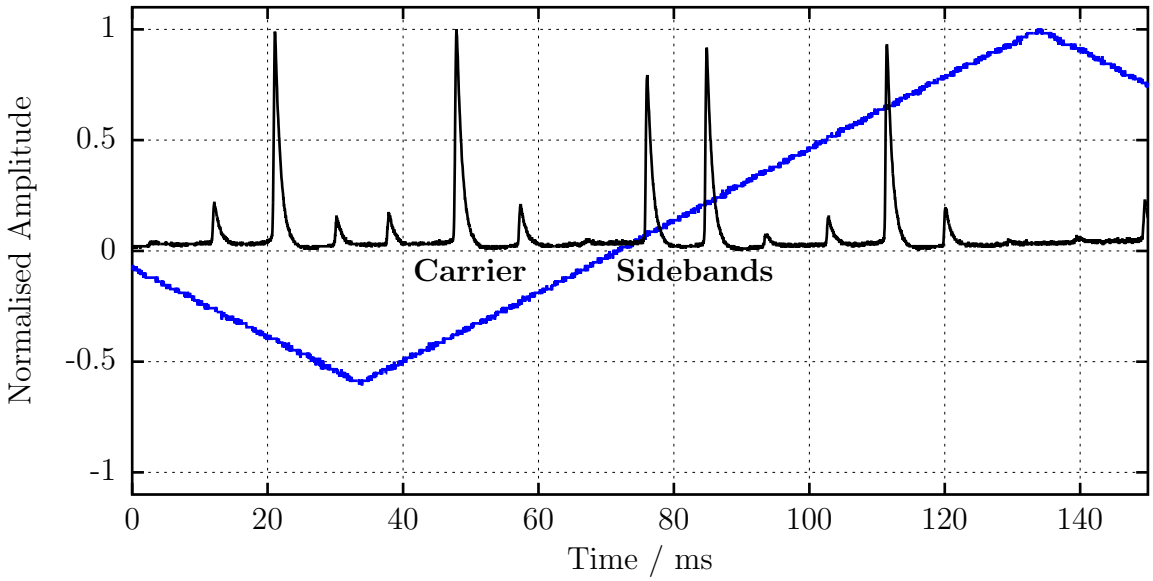

Figure 4.6: Sidebands at 6.834 GHz applied to the Raman laser with a fibre EOM as seen with a scanning Fabry-Perot cavity. A triangular scan with a frequency of 20 Hz was applied to the cavity and can be seen above. The horizontal axis is the observation time of the signals on an oscilloscope.

advantage of this method over using two separate lasers is that there is no need for complicated phase locking to occur between the two as they are from the same source. All that matters is that the microwave source for the EOM is highly stable and precise down to sub kilohertz. The amplitude of the sidebands was measured using a scanning Fabry-Perot cavity (SA200-5B, Thorlabs) with a 1.5 GHz free spectral range (FSR). The spectrum can be seen in figure 4.6, the carrier and sidebands are labelled. Since the FSR is lower than the applied modulation an aliasing effect is seen so that the two sidebands ($\pm$6.834 GHz) appear close to each other. Due to the high power of the modulation signal, additional sidebands can be observed as small peaks. The scan used covers 1.5 FSRs, shown by the appearance of the second carrier peak to the right of the sidebands. The ratio can be controlled by changing the power of the signal used to drive the EOM.

After the EOM there is around 10 mW of light in the fibre; this is not enough for fast Raman transitions suitable for atom interferometry and so the light is passed through two power amplifiers described in section 3.3. The first power amplifier is used at a low current to amplify the light just enough to saturate the second to give a maximum power

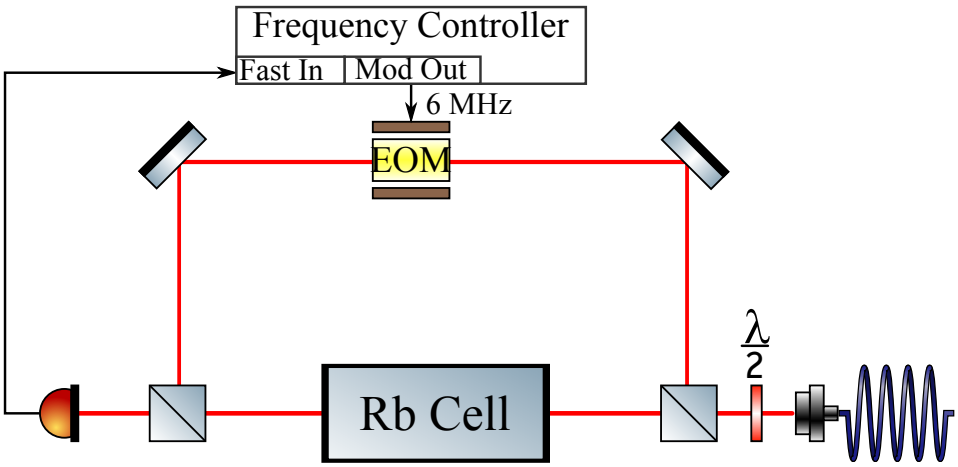

Figure 4.7: Schematic of the modulation transfer spectroscopy setup. The light is separated into two paths, the first passing straight through the rubidium vapour cell onto a photodiode. The other is modulated by an EOM and then travels through the cell overlapping with, but in the opposite direction to, the other.

output of more than 1 W at 780 nm. Following the second amplifier the light passes through an optical isolator and makes a single pass through a free space AOM that is used for fast switching of the light to generate the Raman pulses. The light is then coupled back into another fibre, passing through a fibre switch before entering the chamber. For interferometry schemes involving an optical lattice, large frequency detunings are typical. To lock this laser at detunings up to 50 GHz it was planned that by using high power from the first amplifier, the laser could be modulated with an EOM to generate large numbers of sidebands down to the frequency of the master laser, similar in principle to a frequency comb.

4.2.1 Laser Frequencies

Stable laser frequencies are required for the experiment as the atomic transitions involved depend heavily on the light frequency applied; this is achieved through the use of laser locking techniques. The lasers used are tuned to different frequencies of transitions between hyperfine levels of the D_2 line in ^{87}Rb at 780 nm. The master laser was locked on the $|F = 2\rangle \rightarrow |F' = 3\rangle$ transition in ^{87}Rb using a modulation transfer spectroscopy (MTS) setup [91] – all other lasers were offset locked in reference to this one.

Modulation Transfer Spectroscopy

Modulation transfer spectroscopy [92] is a method of observing spectral lines that are normally washed out by the motion of the atoms. This allows for much narrower laser frequency locks to specific transitions between hyperfine atomic levels. The setup is shown in figure 4.7 – a benchtop version of this design was constructed using standard optics. The master laser was collimated from the fibre and separated into two beams by a beamsplitter with a $\lambda/2$ waveplate to control the ratio of power between the beams. One beam is sent through a glass cell of rubidium vapour and onto a photodiode. The other beam passes through an EOM that is modulated with a frequency of 6 MHz by the frequency controller on the stack electronics (section 3.5) and then sent through the vapour cell overlapping with the first beam but travelling in the opposite direction. The modulation of the second beam is transferred to the first through a nonlinear process via the atoms in the cell. Only a narrow selection of atoms that have near zero velocities in the direction of the beams see both beams, as such it removes the Doppler broadening effect allowing for a much narrower frequency lock. MTS removes 'crossover' peaks that occur at frequencies between transitions in other Doppler-free spectroscopy schemes such as saturated absorption, leaving only the on-resonant transitions.

An optimised error signal recorded from the frequency controller showing the $|F = 2\rangle \rightarrow |F' = 3\rangle$ transition in ^{87}Rb is shown in figure 4.8a. A triangular scan, represented by the red line, is applied to the laser current causing the emitted light to change frequency about the centre of the transition. Two lineshapes are seen as the scan passes the transition in both directions. The signal from the photodiode has been demodulated to remove the 6 MHz added by the EOM in the spectroscopy setup creating the error signal. The electronics lock the frequency to a point on this lineshape, with the usual lock point being at the zero crossing.

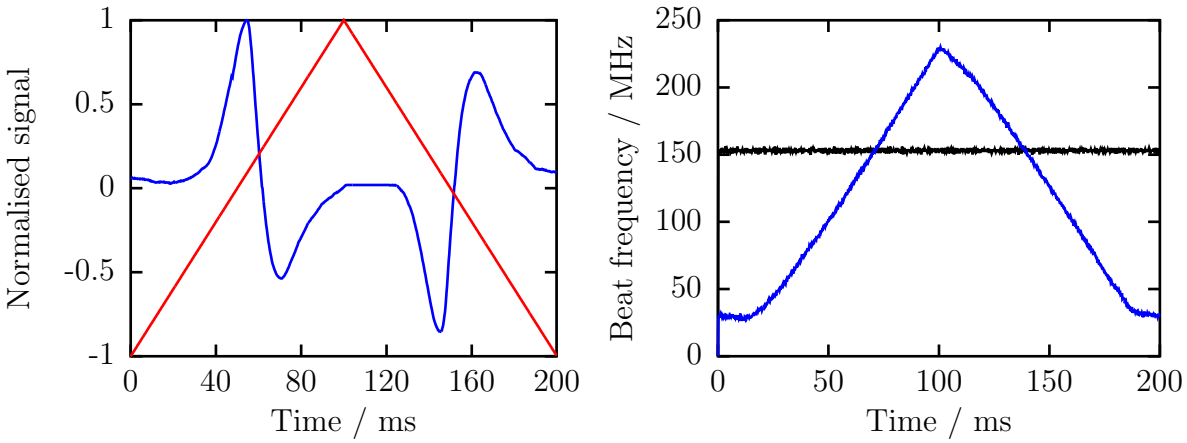

(a) Modulation Transfer Spectroscopy Signal of transition $|F = 2\rangle \rightarrow |F' = 3\rangle$ observed using the stack electronics. Triangular line shows the scan applied to the laser.

(b) The beat signal of the repumper laser with the master, as seen with the stack electronics when scanning the current of the repumper laser (blue line) and when locked (black line). The locked signal has a standard deviation of 1 MHz.

Figure 4.8: Locking signals. The horizontal axes in both subfigures represent the observation time over which the signal variation was recorded.

Offset Locking

The offset lock was provided by the frequency controller board on the stack electronics. A portion of the laser is mixed with a portion of the master laser and then placed on a photodiode, this creates a beat signal at the difference in frequency between the two lasers. Since this frequency is typically in the hundreds of megahertz it can be easily measured with electronics. The beat signal is amplified and sent to one of the fast inputs on the frequency controller using the circuit shown in figure 4.9.

In the frequency controller the beat signal is measured with an onboard frequency counter, a digital PID control then stabilises this value to a setpoint by modulating the current given to the laser diode. A typical signal seen when scanning the cooling laser with respect to the master laser can be seen in figure 4.8b. This shows the frequency of the beat signal being scanned over time. Depending on which side of resonance the scanned laser is, this image appears either pointing upwards for a frequency lower than the resonance 'red-detuned', or downwards for a higher frequency 'blue-detuned'.

The cooling laser was offset locked to the master by observing the beat signal between

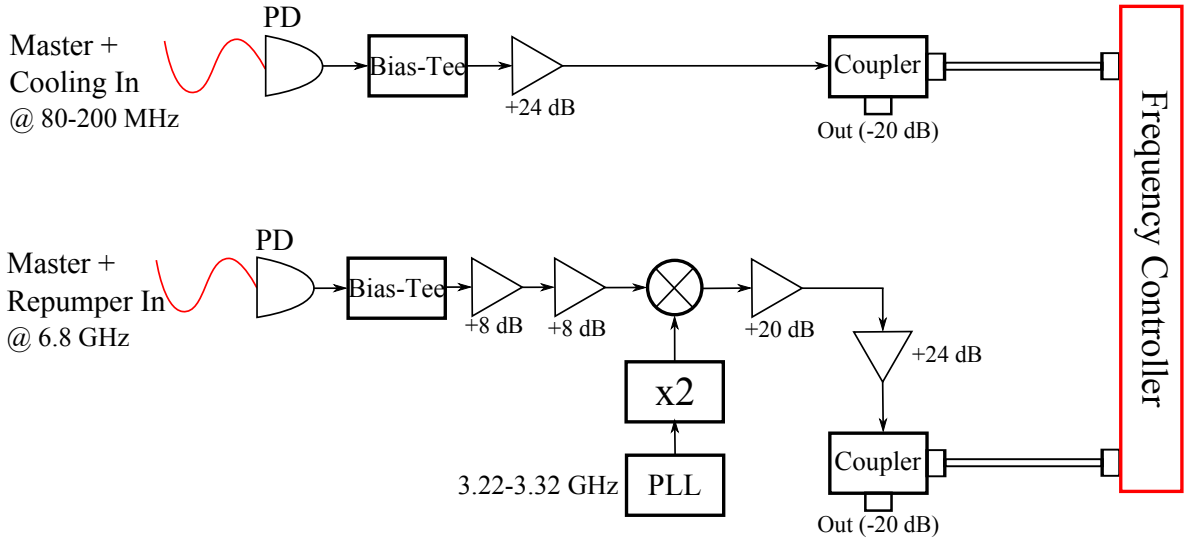

Figure 4.9: Offset lock measurement and amplification module.

them. Since the cooling light passes through an AOM before reaching the atoms, the offset lock point is displaced by 80 MHz to begin. The detuning required for the MOT then has to be added. In our case the MOT with the highest optical density was found at around $-2\Gamma = -2 \times 6$ MHz or twice the linewidth of the transition. The final offset lock position for the cooling laser was 93 MHz. For the detection, the cooling light was used again but the frequency was changed to be on resonance. By optimising a set of absorption images to the highest optical density, the optimum lock point for detection was found to be 83 MHz.

The repumper laser was also offset locked to the master laser in the same way. Since the repumper transition ($|F = 1\rangle \rightarrow |F' = 2\rangle$) is 6.8 GHz away from the master lock transition and the electronics can only measure signals up to 1.1 GHz, the beat signal was mixed with a signal from a 3 GHz oscillator that was multiplied by two, thus creating a peak a few hundred MHz away from the master. The correct value of the repumper lock was then found to be at 153 MHz.

4.3 Optical Delivery System

It is not enough to just generate the light at the correct frequency and stability, it has to be delivered from the lasers to the places it is needed. In this case, the centre of the vacuum chamber.

Where a typical cold atom experiment uses free space optics such as mirrors and lenses to do this, we have used completely fibre optic based components. The advantages of this are that the system should be more robust during transportation as fibre components will not need to be realigned, the complete fibre system is very compact, and the components can be placed almost anywhere within the volume of the package.

The entire system is shown in figure 4.5. The lasers are first connected to a fibre splitter array (Evanescent Optics, Custom) to create beat signals for offset locking, two fibre coupled acousto-optic modulators are used next to control the repumper and cooling light individually before they are mixed with a 50/50 fibre splitter. Two fibre switches (LEONI) are connected to the two outputs of the 50/50 splitter, a 1x2 (one input, two outputs) and a 1x3 (one input, three outputs). One output of each was connected to another 50/50 splitter giving the four beams for the MOT. A second output of the 1x3 is used as the detection beam. A fibre photodiode (OZ Optics) is added before each of the final outputs to give monitoring of laser power in each fibre. The fibre EOM in the Raman laser path can operate over an extremely wide range of frequencies at low RF power giving it an advantage over free-space equivalents. To operate an optical lattice using the Raman laser at high detuning for the schemes that require it, a fibre EOM can be added to generate sidebands at 49 GHz on the light sent to make the beat lock with the master laser.

Light distribution

Two kinds of fibre splitting modules are used in the setup. The 'beat module' that we designed (figure 4.10) combines all lasers for offset locking to the master laser. Three

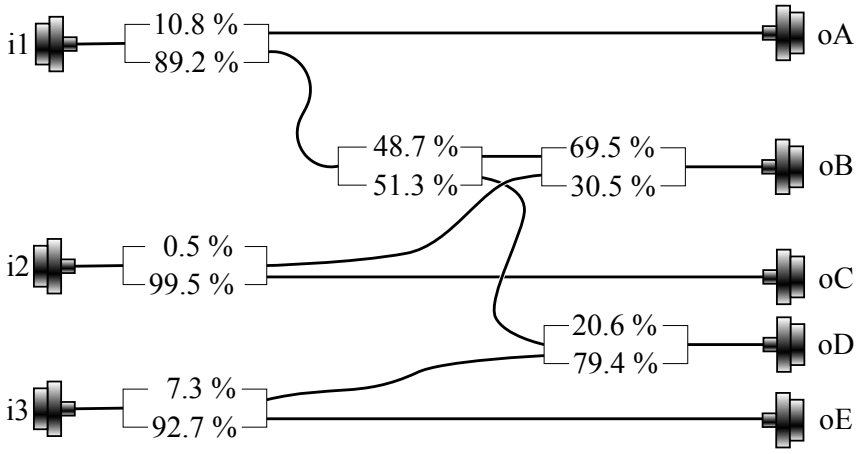

Figure 4.10: Schematic of the laser beat module from Evanescent Optics Inc. The three inputs (i1,2,3) are for the Master, Cooling and Repumper lasers respectively. Outputs oA, oB and oD go to photodiodes for offset locking. oC and oE are the cooling and repumper outputs that eventually go into the vacuum chamber.

outputs (oA, oB, oD) are used for measurement of the beat signal and the other two (oC, oE) send the cooling and repumper light to the vacuum chamber. The ratios displayed are the measured values using the module that was made to our specifications. The remaining three splitters in the MOT system are in 50/50 configuration and the measurements showed this to be true to within less than 1 %.

Fibre AOMs and Switches

Precise switching of the different light beams is necessary for atom interferometry. Two types of switching are required. 'Fast switching' with a switching time less than a microsecond is needed for performing precise state preparation and for the short pulses used for the interferometry sequence that are typically on this time scale. This is achieved using AOMs. An AOM is a crystal in which a travelling sound wave is generated using a piezo-electric transducer usually driven with an RF frequency. The light diffracts from the sound wave at an angle θ dependent on the wavelength of the sound wave Λ and the light λ by the relation $\sin\theta = m\lambda/2\Lambda$. In our fibre AOMs, the $m = -1$ order light is coupled into the output fibre, meaning that the light is downshifted in frequency by the value of the applied RF frequency. The speed of the switching depends on the length of

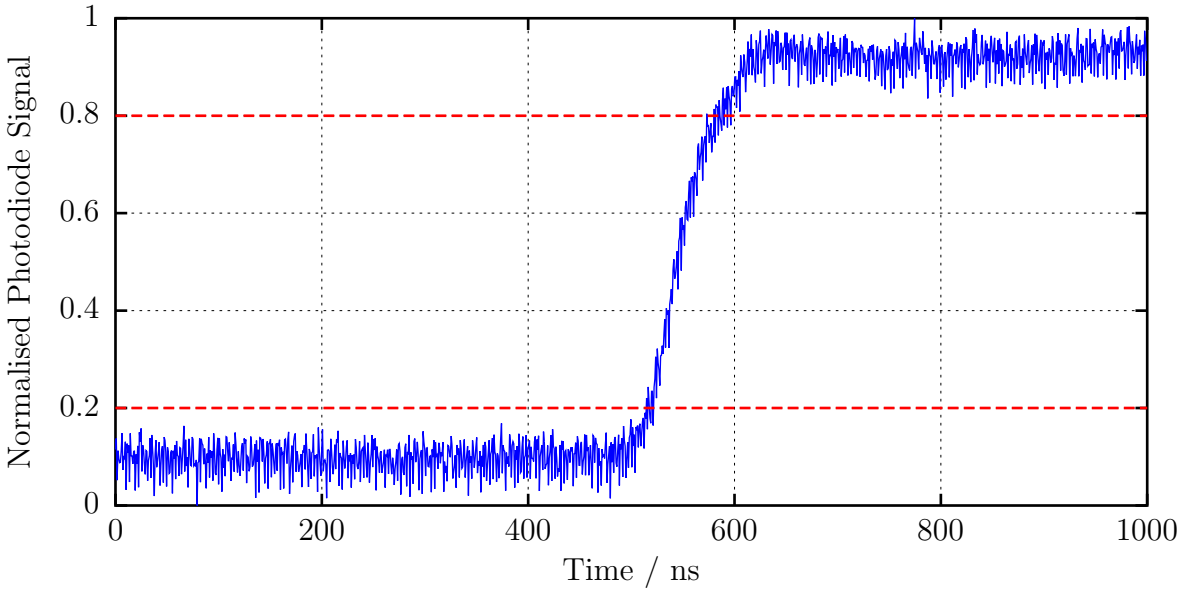

Figure 4.11: Light output from the fibre AOM during switching process. The $20\% - 80\%$ rise time shown by the dashed lines is 70 ns.

time that the sound wave in the crystal takes to cross the light beam. Since alignment of an AOM is key to its power transmission, the fibre AOM adds stability to the system because all the components are fixed in place from the input fibre to the output fibre. 'High extinction' switching is for when total attenuation of unwanted light is desired, for example preventing the light used for the MOT from being present during the interferometry phase. Extra light in this phase would cause light-atom interactions that reduce the signal of the interferometer. This is achieved in other experiments by mechanical shutters, and by us with fibre switches. The fibre switch consists of an input fibre and either two or three output fibres. In between the input and output a glass prism is placed that is attached to a mechanical arm. During switching, the prism is physically moved to redirect the light from the input into the desired output fibre.

The power extinction of the AOM was measured between on and off modes and was found to be just over 50 dB where the specification of the AOM was 30 dB. This means that for a power in the fibre of 500 mW when the AOM is turned off, there will still be 5 µW of light continuing through the system. As a fibre-based alternative to shutters, we used fibre switches from LEONI that give 80 dB power extinction between the channels.

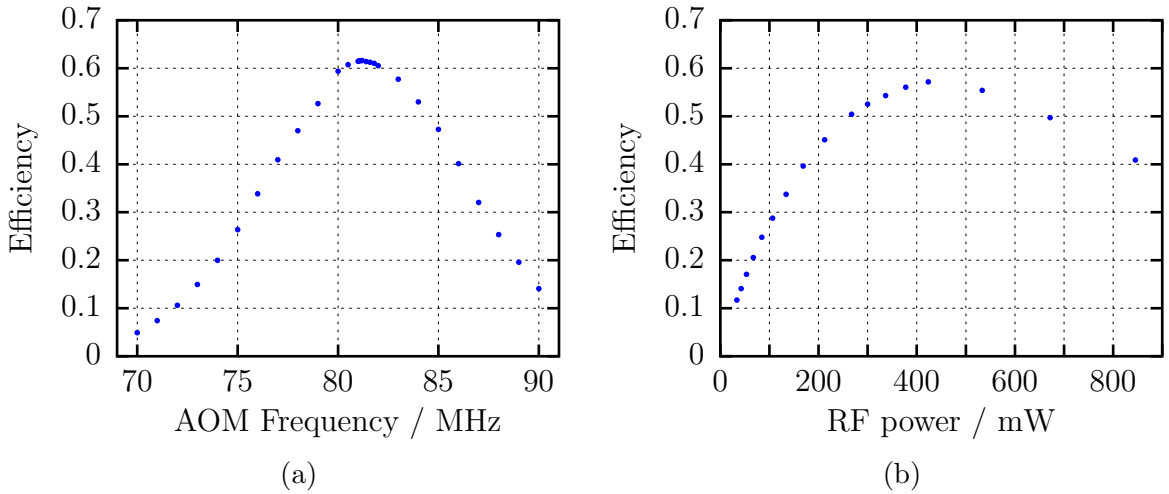

Figure 4.12: Fibre AOM efficiencies. (a) shows output efficiency as a function of applied RF frequency at constant RF power of 450 mW and (b) as a function of RF power for constant RF frequency of 80 MHz.

This, in addition to the 50 dB from the AOM gives a total of 130 dB of attenuation reducing that 500 mW to just 50 fW, small enough not to have an effect on the atoms.

For the fibre AOMs, the designed specifications for peak performance were given as a frequency of 80 MHz and RF power of 500 mW, which would give an efficiency (laser power in vs. laser power out) of 50 %. Measurements of the efficiency as a function of the applied frequency and the RF power were performed and found that the peak efficiency reached a maximum of 61 % when using an RF input of 450 mW and 82 MHz as shown in figure 4.12. For comparison, free space AOMs are capable of efficiencies up to 90 %. The lower efficiency is mostly caused by losses from the coupling at the fibre to crystal interface within the device and a small amount by the fibre to fibre coupler used to get light into the fibre AOM.

Measurements were carried out on the switching time of the AOMs. Using a fast photodiode (Thorlabs DET10A) with a 1 ns rise time the output light from the AOM during the switching phase was observed. The AOM was switched by switching the output of the frequency source. The switching speed was found to be consistently around 200 ns, figure 4.11 shows one fibre coupled AOM switching on with a 70 ns rise time (20 %−80 %), there is a delay between the modulation signal switching and the output of 1 µs. The

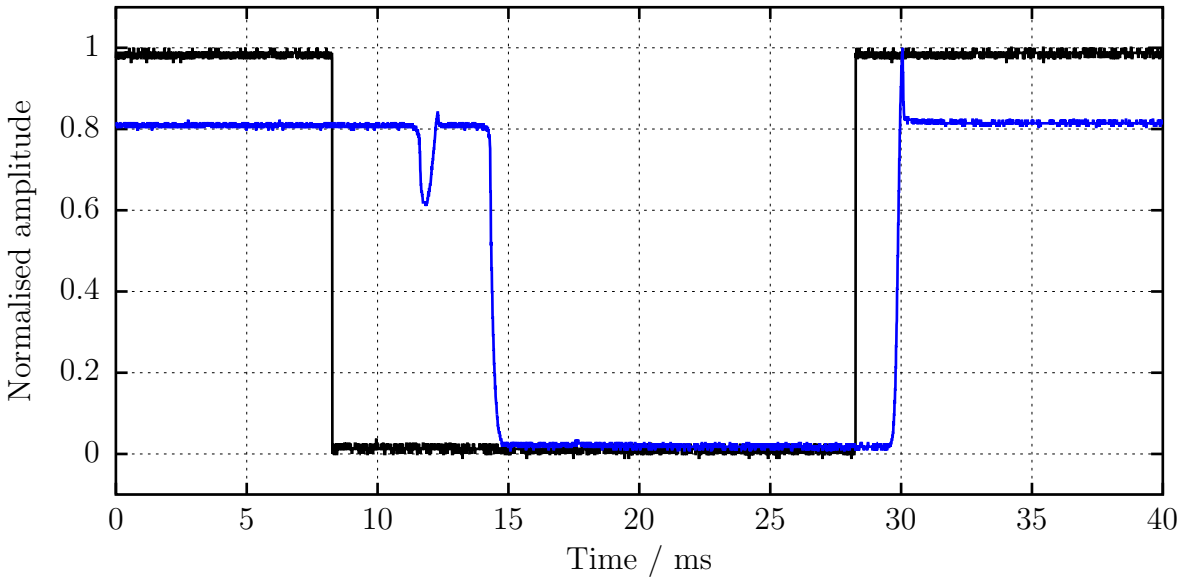

Figure 4.13: 1x3 fibre switch output during switching. Blue shows the signal from a photodiode at the output fibre. Black is the trigger signal. The 'bouncing' effect can be seen on the first switching during the trigger falling edge, extending the total switching time to 4 ms compared to the 1 ms seen on the trigger rise side.

delay is the same for rising and falling so will not affect the length of a light pulse. This shows that the fibre AOMs are suitable for reliably producing short interferometry pulses on the order of a few microseconds.

The fibre switches used had a switching time of between two to seven milliseconds, depending on the configuration. The actual switching takes 2 ms, however a 'bouncing' effect was seen on some switching modes increasing the time to 7 ms. This is caused by the mechanism passing the end point of the switch and bouncing back to the correct position. When the system was assembled into its final form this was considered and the paths on which the bouncing occurred were chosen to be the 'dump' fibres so that it did not have an effect on the atoms.

To assess the robustness of these fibre components, vibration tests were carried out by the University of Hamburg. This involves placing the component on a platform that vibrates to apply forces up to and exceeding 20 times the gravity of the Earth, to simulate rocket launches. Of the components that were tested, only the fibre switch failed and had to be returned to LEONI. The cause was found to be the type of glue used to affix the

prism inside, which was not specified to the high vibration forces. It was repaired by using suitable glue before passing a second test run.

4.3.1 Fibre component integration

Since the components of the fibre delivery system were sourced from separate companies, we had to choose how best to connect them together. We opted to splice the fibres directly since this is the most vibrationally stable and compact option; the typical losses at spliced interfaces are less than 1 %. A fusion splicer (Fujikawa ARCMaster) was used that generates a plasma arc to melt the two ends of the fibres and pushes them together to fuse them into one continuous fibre. The process of splicing involves first removing any connectors and stripping the coatings of the two fibres to be joined down to their cores. The core sizes for all fibre components were ordered to be identical (5.5 µm) to avoid losses due to mismatches at the interfaces. The two ends were then placed in the splicer with care to keep them level, and the controls were used to rotate and align the fibres. All fibres used were single mode polarisation maintaining fibres, so the rotation had to be precise in order to keep the polarisation stable throughout the whole system. The final step was to secure the spliced region with a small metal rod in a section of plastic tubing, that was then heated to shrink around the fibre and prevent unwanted stress on the splice.

Figure 4.14 shows the completed fibre system for master, cooling and repumper lasers. The Raman system was separate and only contained a single splice. As can be seen there was a lot of excess fibre, this was kept in case there was a need to replace any of the components.

The transmission efficiency of the entire fibre system was measured for the cooling and repumper lasers at each output and the results are presented in table 4.2. The input power was measured after the optical isolator and before the fibre coupler. This includes losses due to fibre coupling at the inputs of the system, estimated at 40 %, 1 % loss at each spliced interface, 40 % due to the efficiency of the fibre AOMs and 10 % at the fibre

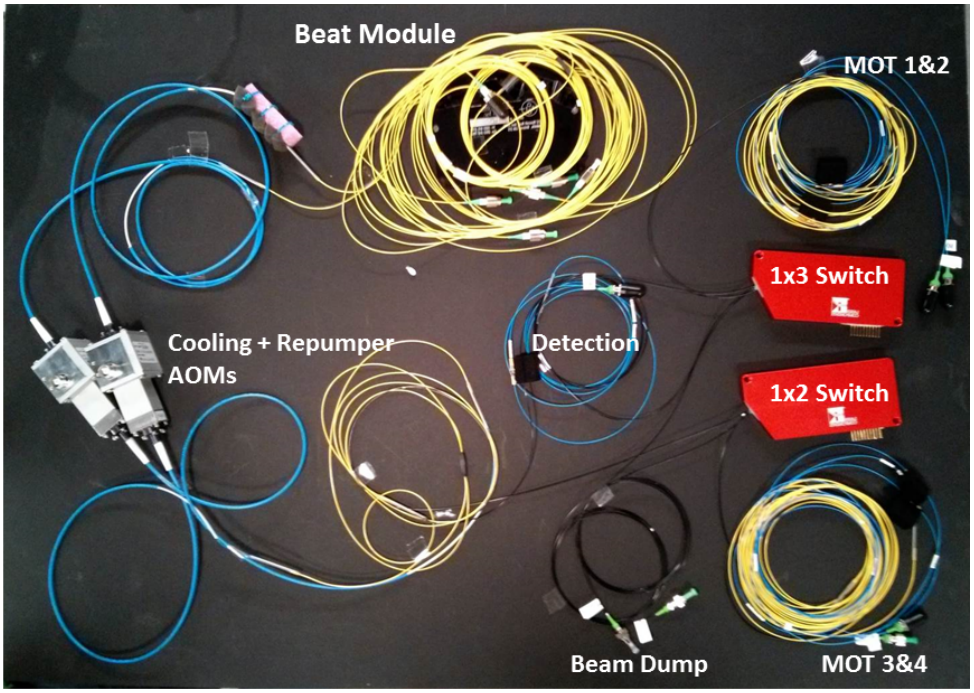

Figure 4.14: Photograph of completed fibre optic delivery system taken immediately after fibre splicing. The system generates the cooling and detection beams and mixes together the beat signals for offset locking.

Output	**Cooling Transmission (%)**	**Repumper Transmission (%)**
Detection	17.5	16.2
MOT1	8	7.3
MOT2	8.4	6.8
MOT3	8.4	7.1
MOT4	8	6.8

Table 4.2: Light transmission efficiency of completed fibre system. This includes coupling losses at the input and the losses inside each component.

switches. For example, for 500 mW of cooling laser power from the diode and after the isolator, each of the four MOT beams would contain around 40 mW of power.

An issue with using a fibre based system was that some polarisation fluctuations arose due to poor alignment of the light injected into the fibre and slight errors in splicing. These were rectified with a polariser that was placed at the output of the fibre before entering the vacuum chamber. Although this 'cleans' the polarisation of the beam, the trade-off is that the polariser converts the fluctuations in polarisation into intensity fluctuations. It was found that the influence of the beam intensity on the atoms was less critical to the experiment than the polarisation and so the polariser was implemented. For future

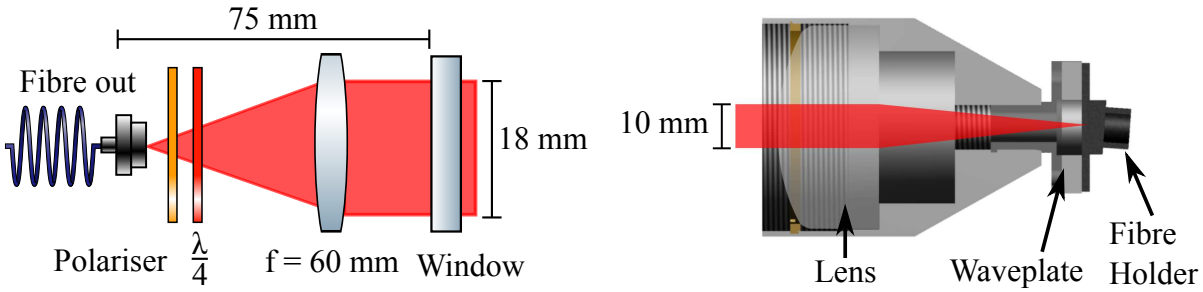

(a) (b)

Figure 4.15: (a) shows a drawing of the collimator used for the MOT beam constructed with off the shelf parts to give a collimated beam diameter of 18 mm. (b) is a CAD rendering of the Raman collimator with $f = 40$ mm lens used to give a collimated beam diameter of 10 mm.

use of this method the addition of an in-line polariser section of fibre such as the FOP-11 from OZ Optics placed at the end of the fibre system should be considered. The setup is also not very adaptable to configurations other than the one planned and so this must be considered during the planning phase of any project looking into this method.

4.3.2 Fibre to Chamber Interface

The final step in the optical delivery system is to collimate the light from the fibre output and direct it into the vacuum chamber. The chamber was designed with mounting screw holes around each window so that optics could be attached directly to the metal. Mounts with the ability to be adjusted were constructed to connect to standard SM1 threaded lens tubes that contained the optics for the MOT beams; another was made for the 40 mm threaded Raman collimator.

For the MOT beams the collimators consisted of a fibre connector followed by a polariser to clean the polarisation of the light from the fibre system, a quarter waveplate to convert the linear polarisation from the fibre into circular polarisation for the MOT and then a single lens with focal length $f = 60$ mm to give a collimated beam with diameter 18 mm. The total length of the MOT collimators, including the fibre connector, was 75 mm. A drawing of the collimator can be seen in figure 4.15a.

For the Raman beam, a collimator was made based on a design from LUH around the

idea of using a single lens. The use of a single lens reduces the possibility for aberrations to be imprinted on the beam from multiple lenses. The collimator uses a single $f = 40$ mm lens (Newport KPA22) with a diameter of 40 mm to collimate the Raman beam to a diameter of 10 mm, a size chosen due to the fact that the cold atom cloud is 5 mm from the surface of the atom chip. If the Raman beam were to hit the side of the chip it could introduce unknown distortions across the surface of the beam. The fact that such a large diameter lens is used for the Raman beam which is only 10 mm across also comes from the desire to reduce wavefront distortions across the profile of the beam. Since the atoms are at a non-zero temperature, they will move into a different part of the wavefront during each Raman pulse, thus being imprinted with a different phase. This causes a washing out of the interferometry signal as it becomes difficult to cancel out the imprinted phase with the final Raman pulse.

A cut through of the collimator design is shown in figure 4.15b. The fibre is held at one end in front of a section that can be rotated and locked with screws used for holding a quarter waveplate. This entire brass section is threaded so it can be screwed into the large aluminium lens holder and locked using a nut. The distance of the fibre end to the lens can be adjusted to collimate the beam with the correct diameter. The lens is fixed in the final section using a threaded brass locking ring. The entire setup is then screwed directly onto an adjustable mount attached to the chamber.

4.3.3 Detection Systems

The initial measurements of the atomic cloud took place in the vicinity of the trapping region. Absorption imaging was used to measure the cloud density and for performing time-of-flight measurements to determine its temperature. Light from a fibre was collimated with a single $f = 150$ mm lens giving a beam of diameter 25.4 mm. The beam was then sent through the large main window into the chamber horizontally at 45° to the surface of the atom chip. The beam is then reflected by the chip and passes through the cloud. Using a beam that is on resonance with the atoms, a portion of the light is

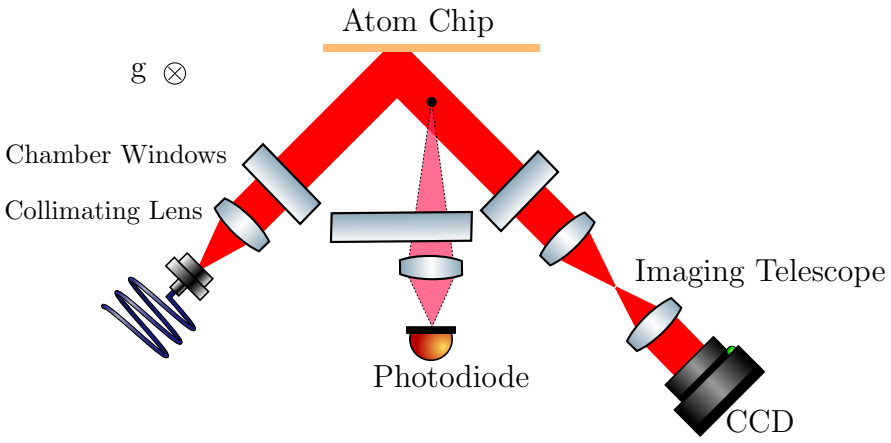

Figure 4.16: Detection setup (shown from above) in the iSense chamber for measurements in the vicinity of the MOT. The detection light is collimated from a fibre and reflected from the atom chip before passing through the atom cloud. A CCD camera is placed opposite to perform absorption imaging. Fluorescence imaging is also available with a photodiode situated at an angle of 45° from the detection beam.

absorbed, leaving a shadow on the beam. After leaving the chamber via the main window, two lenses ($f_1 = 60$ mm, $f_2 = 50$ mm) separated by 10 mm focus the absorption image onto a CCD camera (TheImagingSource DMK31BU03). This ratio of focal lengths means that the cloud size observed on the image is magnified by $m = f_1/f_2 = 1.2$. The CCD chip itself has 1024×768 pixels that are 4.65 µm in size, the whole chip measures 5.8 mm $\times$ 4.92 mm giving a maximum cloud size that we can observe with this system of 4.1 mm. The optical setup can be seen in figure 4.16. Using this reflection method was the optimum solution since the only other horizontal viewports are used for the MOT beams and using a non-horizontal setup would mean that the atoms would drift out of focus as they fall under gravity. The reflection of the cloud can be seen on the image during the loading of the MOT by its fluorescence and so the system was angled so that the reflection and cloud were clearly separated, ensuring that the reflected light did not affect the measurement. The light from the cooling laser was used as the detection light, the lock frequency was changed to be on resonance with the $|F = 2\rangle \rightarrow |F' = 3\rangle$ transition. This means that only atoms in the $|F = 2\rangle$ hyperfine ground state were detected.

Fluorescence imaging looks at the light emitted by the atoms directly as a result of them de-exciting after absorbing light. A single $f = 50.8$ mm lens was placed close to

Board	Number
PC104 Interface	1
Power Distribution	2
Laser/TA Current Driver	5
Temperature Controller	4
Ion-Getter Controller	1
Analog Output	1
Frequency Controller	1
DDS	2
Fan Driver	1
Total Number	**18**

Table 4.3: Complete list of stack electronics used in iSense.

the main window to capture as much of the fluorescent light as possible. An avalanche photodiode from Thorlabs (APD120A/M) was used to view the signal and the output was recorded from an oscilloscope. Fluorescence imaging was used to measure the loading curve of the MOT since it responds much faster than a CCD camera. It is also more sensitive to small fluctuations in intensity and so it was used for viewing the small signal of the population change caused by the Raman beam.

4.4 Electronics

Originally developed as part of the QUANTUS project, the electronics were still in development during the lifetime of the iSense project. As a result of this, we were entering new territory by using the stackable electronics for complete control of the system. The PC104 interface system had not been used to this extent as other projects have mainly used a direct PC to USB interface or a National Instruments PXI-FPGA system. The frequency control, DDS and Analog Out boards were also new for iSense. The final number of boards used is shown in table 4.3.

Boards were delivered when they were completed and integrated when needed. This involved first testing with a USB interface board to learn about the operation of the board in a controlled environment without possible damage to experimental equipment. Then the address of each board was set to avoid conflicts, before adding this information to the

'stack' file (see section 4.4.1) then writing the board functionality into the main LabVIEW program.

Some integration issues were discovered through the course of this project. If too many boards (more than 10) are used in one stack, the clock signal degrades to a point where timing errors occur. This was rectified through the use of an additional stack with its own 10 MHz oscillator where only the bus communication signals are connected between the two. This can only be done with boards that have no need to be synchronized with high precision to the main stack, such as TA current drivers and temperature controllers. The DDS and Analog Out boards also had problems when they were integrated in a stack that contained a laser current driver and a temperature controller in which they simply failed to work. The solution at the time of writing was to keep them in a separate USB stack and connect only the trigger signals from the main stack. This allowed timings of the DDS and magnetic coil switching to maintain synchronisation with the rest of the experiment.

The 1 GB flash memory module that was shipped with the PC104 computer and used to store the operating system and LabVIEW program failed after a year of operation. The cause was surmised to be that too many write operations had occurred on a number of memory blocks. This caused a failure of some of the blocks and the entire drive to break. A replacement drive (DELOCK 54149) was found that implements 'wear leveling' – a technique used to distribute write operations evenly across all the memory blocks, hopefully extending the life of the drive.

The current carrying pins are only rated up to 10 A – with multiple laser amplifiers and temperature controllers being used this can be exceeded, however using separate power supply boards for multiple stacks prevents this from being a problem. In a multiple stack configuration, they can still be combined into a single tower by using connectors with unwanted pins removed if that is desired. Care must be taken as boards can be easily destroyed by connecting the wrong pins together.

The final electronic stacks used for iSense can be seen in figure 4.17 before integration

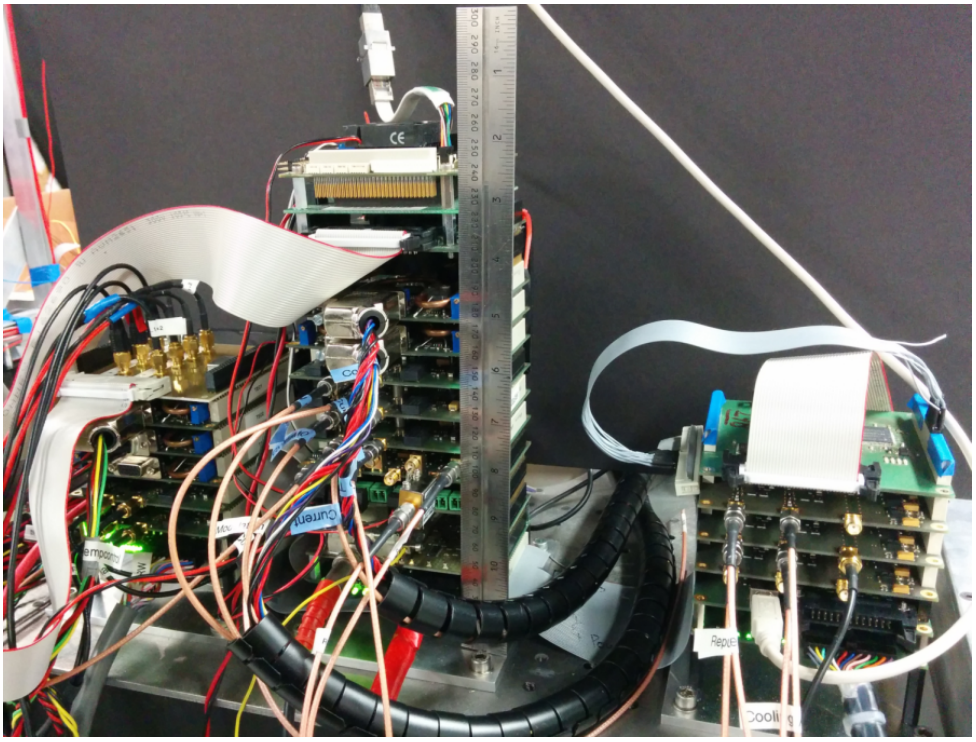

Figure 4.17: Photograph of final iSense stack electronics. The height of the main stack is 265 mm.

in its transport packaging, and a list of the boards used in table 4.3. The main stack (central) has the PC104 computer, FPGA interface, two temperature controllers, laser controllers for the master, cooling and repumper lasers, the frequency control board, fan driver and IonGetter controller. It is flanked to its left by a stack with its own clock containing three temperature controllers and two TA current drivers, at the top is an IDE to SMA interface board for the external triggers. To the right is the USB stack that contains the two DDS and two AnalogOut boards.

Frequency control

One DDS board was used to generate the 80 MHz signals for the two fibre AOMs in the cooling and repumper laser system. The boards give an output of 0 dBm – using an RF amplifier this was increased to the 27 dBm needed for optimum efficiency. Another DDS board controls the Raman AOM and the frequency applied to the Raman EOM. It uses one of the 100 MHz outputs from the frequency chain as a reference clock, to ensure that

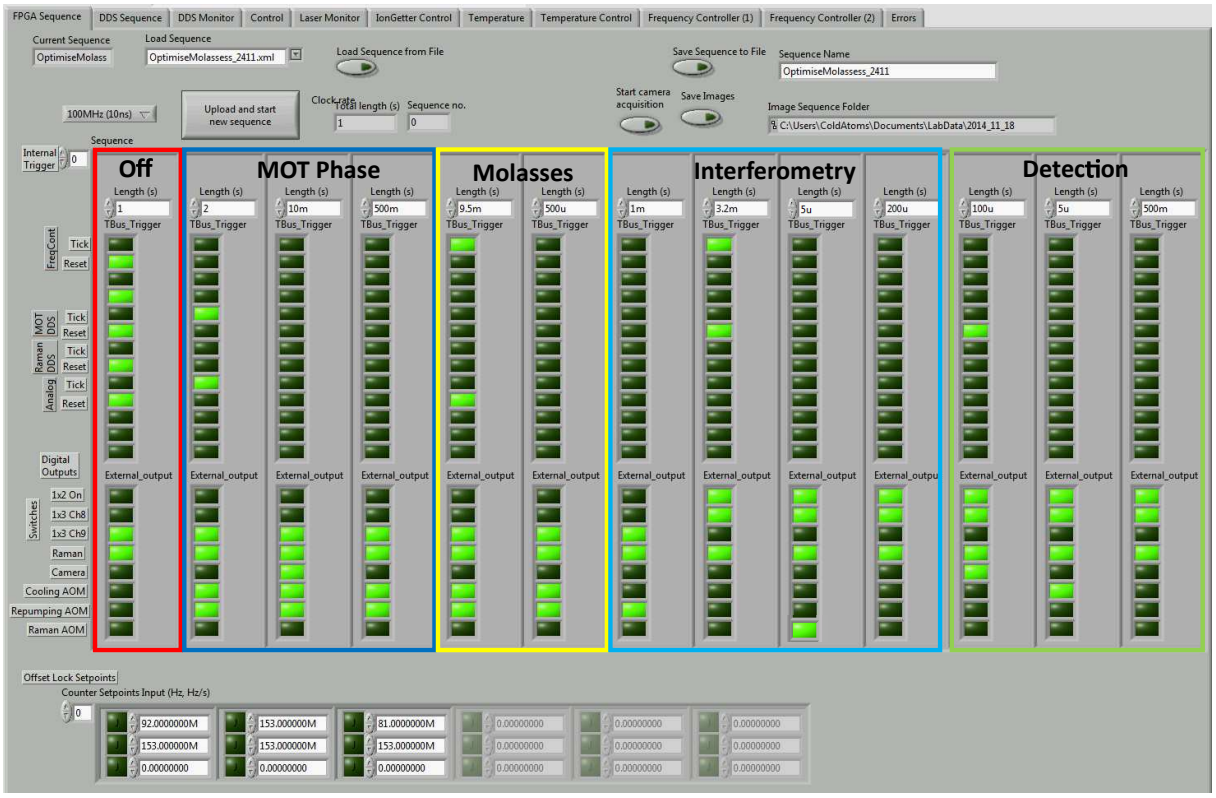

Figure 4.19: Screenshot showing computer control software programmed in LabVIEW. This image shows the panel used to run an experimental sequence. The sections corresponding to the different experimental phases are labelled. Tabs at the top are used for controls that do not need to be changed once set such as laser currents and PID settings.

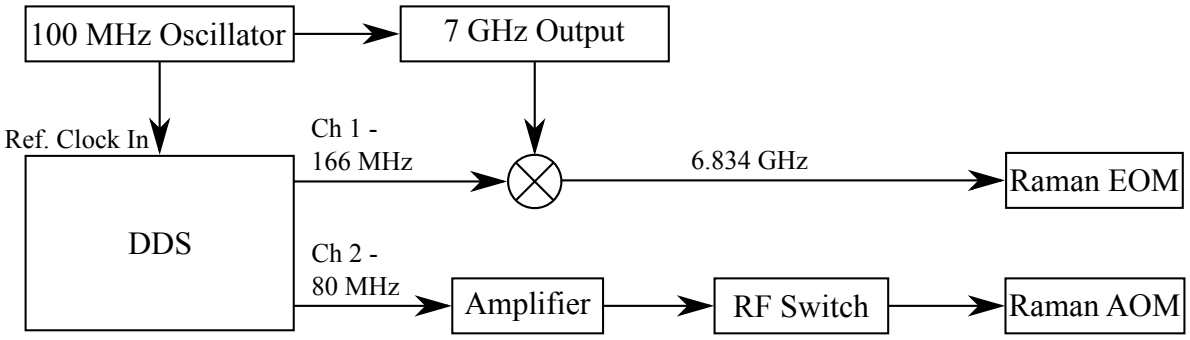

Figure 4.18: Schematic of control system for signal applied to the AOM and EOM in the Raman laser system. The use of the same 100 MHz oscillator as a shared clock signal ensures phase coherence of both modulators.

the Raman frequencies are all well synchronised. The Raman frequency was created by mixing the 7 GHz source from the frequency chain with a 166 MHz signal from the DDS giving a stable 6.834 GHz. The DDS frequency can then be changed and swept to perform the interferometry measurements. The setup is shown in figure 4.18.

It was found that when the DDS was set to zero amplitude there was still a small amount of RF leaking into the output port and being sent to the AOMs. This meant that there was some repumper light at times when there should only be cooling light and vice versa. This manifested itself as ineffective state preparation after the molasses phase. To correct for this, three RF switches (Minicircuits ZX80-DR230+) were added between the DDS (cooling, repumper and Raman) outputs and AOM amplifiers. These were triggered using the digital outputs of the stack.

4.4.1 Computer Control

The stack electronics were controlled via a Kontron MOPSIcdLX PC104 computer mounted at the top of the stack on which the LabVIEW realtime operating system was installed. The user interface was programmed in LabVIEW to enable simple user-friendly control over the entire experiment. A program was created with a tab-based design to control the experiment, the main panel has the experimental sequence control, while further panels control the laser currents, temperature controllers and the frequency locking.

The front panel of the user interface is shown in figure 4.19; this provides simple

programming of sequences. It runs sequentially in columns from left to right. Each column has a time value that tells the system how long it should perform that command before moving to the next column. Below this is an array of green boolean buttons, the top half controls the digital triggers that run down the interface connectors. These are used for triggering stack boards such as the Analog output, to make them change the next value in their table. The lower half controls the eight external triggers for the AOMs, fibre switches and camera. At the bottom of the image are the offset lock setpoint frequencies so that the detuning of the lasers can be changed, these can be set to jump frequency or perform sweeps. Subsequent columns of the table are enabled by the internal trigger. Sequences can be saved and recalled for future use.

The USB stack is controlled with a secondary LabVIEW program that is used for entering tables of values for the DDS and AnalogOut boards; the entries in these tables are stepped through with the internal triggers from the main stack in the same way that the frequency controller is. This ensures synchronisation between all aspects of the system.

In the future, once the experimental parameters are well known, most of these settings should be able to be hidden behind a simplified user interface with an on switch and give an output of the results of the measurement.

Another LabVIEW program controls the camera and can record images from it. The camera is connected to the main PC via USB. The PC is used for this because of the limited (1 GB) storage space and processing power (CPU 800 MHz) on the stack computer, making it unsuitable for image processing tasks. Through the use of a shared variable in the LabVIEW program it can be enabled from the stack computer over ethernet to enter trigger mode and save images when it receives a trigger signal.

4.4.2 Chip Current Drivers

Before the chip current drivers arrived, the coils were powered directly from laboratory power supplies in constant current output mode, a separate one being used for each wire.

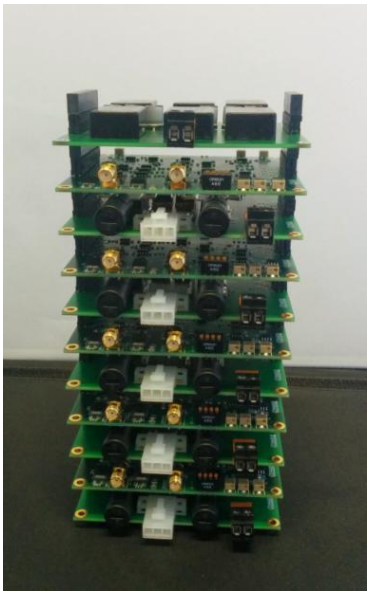

Figure 4.20: Photo of the stack of chip assembly current drivers.

A circuit was made using insulated-gate bipolar transistors (IGBTs) to switch the current to the coils. The IGBTs were triggered using signals from the stack running through an optocoupler circuit to protect the stack from high voltages that can be generated on the other side. The switching characteristics of the IGBTs are given by a varistor that is placed in the circuit.

The chip current drivers employ a PID circuit to optimise the switching time of the current outputs. Potentiometers on the board allow for adjustments to be made as the values will vary heavily depending on the inductance of the magnetic coils used. The first step in this is to ensure that zero output is truly zero. The output is created by the board balancing the positive and negative supply voltages, any mismatch in the supply has to be compensated using a potentiometer on the board. We used a supply voltage of ± 3.3 V to mimic a battery supply such as the one that is planned to be implemented in the future.

A test resistor of a similar resistance to the coil was plugged into the board and then the analog output connected. Two more potentiometers were used to ensure the output current matched the input voltage. The PID settings were then calibrated for switching speed by viewing the voltage across the resistor on an oscilloscope. The final

Coil	Switching time (µs)
PCB_PLUG	170
PCB_Z	190
QUAD2	540
QUAD1/3	750

Table 4.4: Optimised switching times of trapping coils using chip current drivers at the currents required for generation of the MOT.

optimised switching times for each coil are in table 4.4. The longest switching time was for the QUAD1/3 coils due to the large current and higher inductance of those coils. To avoid any possible effects on the MOT caused by the magnetic fields switching off at different times there are two options; the first is to characterise the difference in switching times well and trigger the coils at different times to mitigate the problem, the other is to simply adjust the PID parameters to manipulate the switching times to be the same. We chose the second option as it reduces unnecessary complexity in the experimental control sequence. The final switching time for all coils was chosen to be 750 µs.

4.5 The System in the Laboratory

The integration and testing that has been described in this chapter took place in Birmingham on a small optical table. The culmination of which is shown in figure 4.21a, for reference the size of the table is 100 cm × 180 cm. Although spread out over the surface of the table, the photograph contains all of the lasers, optics and electronics required to operate a cold atom interferometer. It is clear even at this stage that the entire system is extremely compact compared to typical scientific experiments.

It was in this configuration that the cold atom measurements detailed in chapter 6 were carried out. Atoms of rubidium were initially trapped and cooled using this setup and then Rabi oscillations were observed followed by Ramsey interference fringes. Following the successful observation of interference fringes in this configuration, the pictured components were then packaged into a portable system that will be described in the following chapter.

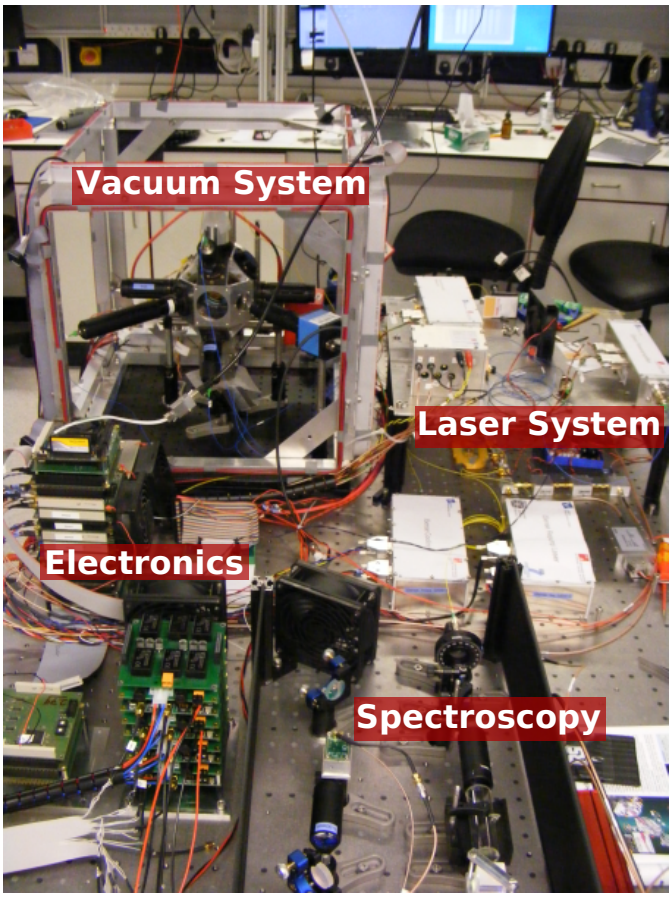

(a)

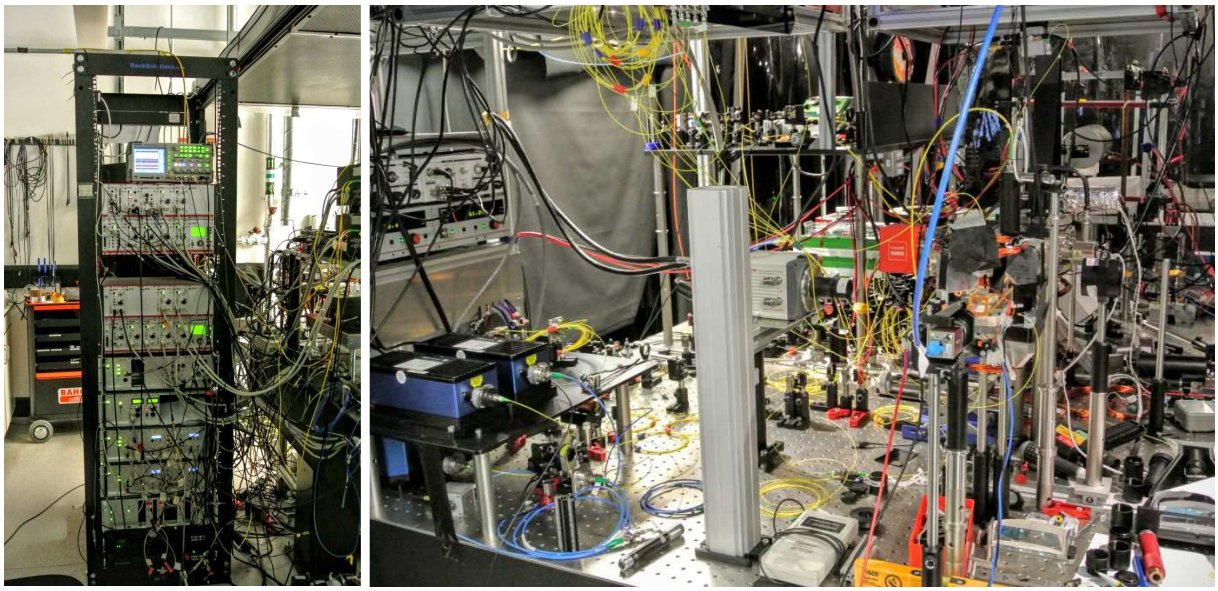

(b)

Figure 4.21: (a) shows the system on an optical table in the laboratory in Birmingham before packaging. Not pictured are the power supplies and the frequency chain. In comparison to a typical cold atom experiment in another laboratory in Birmingham (b), note in particular the rack of electronics pictured is about 2 m in height.

4.6 Summary

This chapter described the overall experimental setup and characterisation of the components that it contains. The atom chip assembly was installed in the vacuum chamber and a stable vacuum pressure of the order of 10^{-8} mbar was achieved. A fully fibre optical delivery system from laser box to vacuum chamber was realised, with telescopes mounted directly to the chamber. The Raman laser telescope gives a beam with a diameter of 10 mm, suitable to prevent clipping by the atom chip. The components of the fibre system were characterised and found suitable for the purpose. Both absorption and fluorescence imaging systems were constructed.

For control of the system, a LabVIEW program was developed that allows for simple entering of experimental sequences. It also controls all laser currents, frequency locking, frequency generation, analog voltage outputs and triggering. Another program records images from a CCD upon receiving a trigger.

The next chapter describes the packaging of these components from a benchtop experiment to a portable device and details of the first transportation and operation thereafter.

CHAPTER 5

ISENSE ON TOUR

The final iSense project meeting with our partners and referees from the EU took place at the West Midlands Region office in Brussels. Since one of the main objectives is to create a portable system, it was decided that this would be the first test of the mobility of the system and also act as a demonstration of the achievements of the project.

Having obtained the first Ramsey fringes in the laboratory in Birmingham, attention immediately switched to packaging the system to achieve the goal of operating the system in Brussels.

This chapter contains the details of the packaged iSense system and its transportable operation. A critical analysis of how suitable the device is for use in various 'real-world' situations is presented, along with details for future modifications to improve the practicality of the system. The results of the atom interferometry measurements recorded with the system in its portable configuration are presented in chapter 6.

5.1 The Packaged System

The iSense system was packaged in a shockproof equipment case; it had dimensions of 100 cm $\times$ 90 cm $\times$ 70 cm and had a 19 inch rack section 16 units high within. This case contained all the lasers, optics and electronics, the frequency chain and the vacuum system. A second smaller box (83 cm $\times$ 67 cm $\times$ 70 cm) containing a UPS (Xi1500, Powersolve) and three power supplies (HMP4040, Hameg) was used to supply the power to

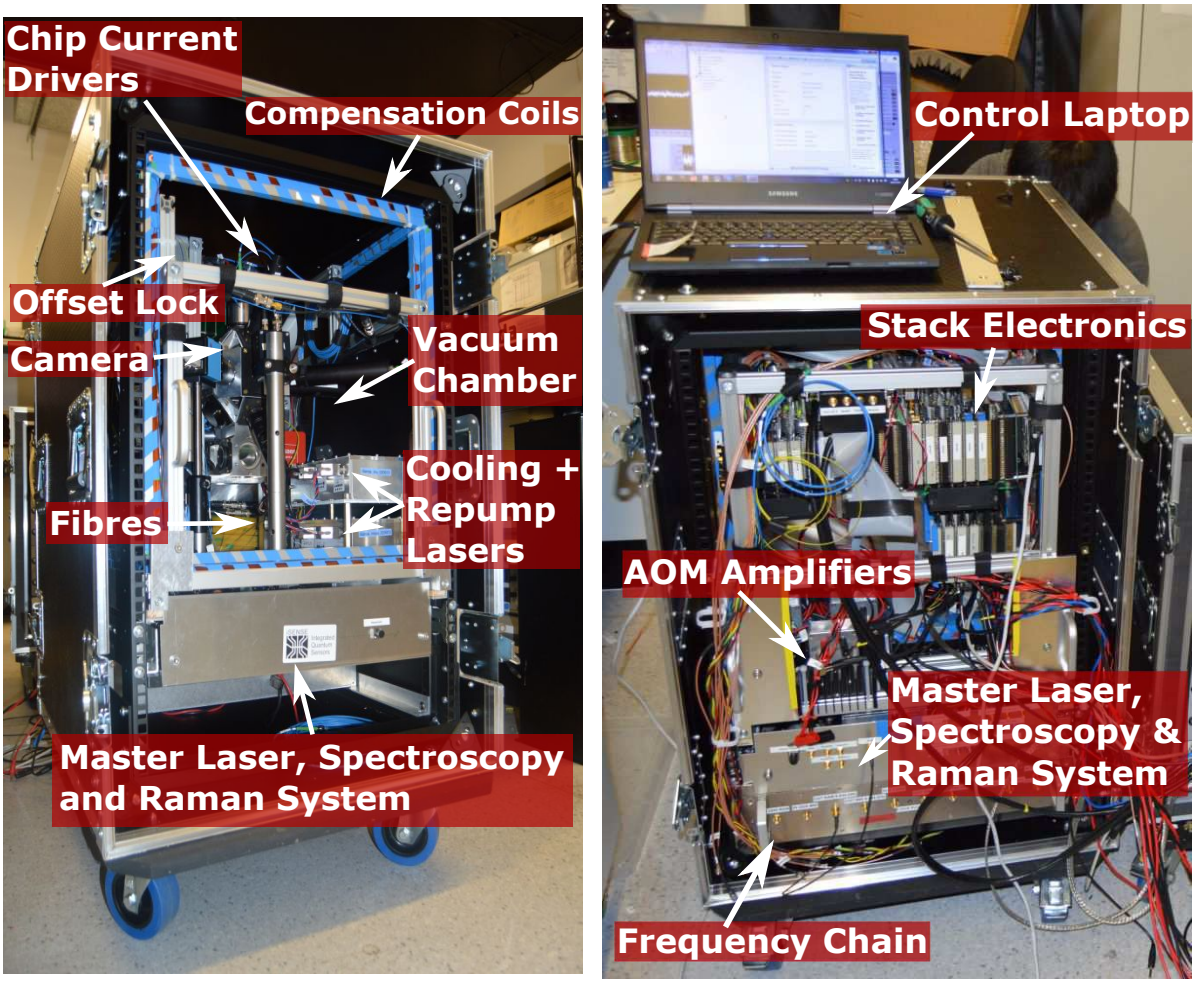

(a) (b)

Figure 5.1: The packaged iSense system. (a) shows the science package from the front with the vacuum chamber, compensation coils, some laser modules and the chip current drivers. (b) shows the reverse where the majority of the electronics are situated.

the experiment. The case with the system mounted is shown in figure 5.1. The upper section contains two aluminium plates of thickness 10 mm, at 90° to each other with the vertical plate set part way along the baseplate. The cooling, repumper and master lasers are mounted on the baseplate along with much of the fibre optic system. The vacuum system is held with aluminium profile, of cross-section 15 mm × 15 mm, between the baseplate and the vertical plate. The majority of the electronics are mounted on the side of the vertical plate away from the chamber so that the plate provides some isolation from the EM noise generated by the electronics. The chip current drivers are mounted to the plate slightly above the atom chip assembly section of the vacuum chamber to give the shortest possible cable length between them and the chip connector, reducing the effect of high current switching on the other electronics.

The benchtop spectroscopy setup was mounted on an optical breadboard that was cut down to fit inside the 19 inch rack dimensions. Rails were attached to the side to give easy access for potential readjustment. The Raman system was also mounted on this board which was then placed below the main chamber section, it can be seen in the picture as the upper of the two silver boxes. This rack unit can be replaced entirely when the micro-integrated spectroscopy setup is delivered because the components can then be integrated in the main upper section. Finally, below this is located the reference frequency chain inside the 19 inch rack box in which it was delivered.

The system was then placed in a minivan equipped to carry two wheelchairs (Peugeot Expert Independence); an extremely small vehicle for transporting an entire atom interferometer system. The UPS can power the experiment by itself for about 1.5 hours but additional power was provided by a 100 Ah car battery using a 12 V DC-230 V AC inverter. This was the smallest solution that could be implemented in the time available but should be easy to compact further. It is also hugely inefficient due to the fact that this setup converts from DC-AC-DC-AC-DC[1]. A setup that generates the DC voltages for the electronics directly from combinations of 3.3 V batteries (Headway LifePO4 38120S)

[1]Battery – Mains Voltage – UPS Internal Battery – Power Supplies – DC Stack Voltages

Component	Volume (l)
Lasers and Amplifiers	12.5
Fibre Delivery System	9.6
Stack Electronics	10.0
Chip Current Drivers	6.0
Vacuum Chamber	14.4
Frequency Chain	8.6
Total	61.1

Table 5.1: List of volume of individual iSense components in litres. The packaged volume was higher at 120 litres.

has been planned but not yet implemented.

5.2 Analysis of Portability of System

The main aspects for a portable device are size, weight and power consumption. All three need to be reduced to make something truly portable; there is no point making a device small and light that requires a power plant to operate it. This section will break down the details of the iSense system and compare them to the Micro-G LaCoste FG5-X – as the device that we are ultimately aiming to best. The FG5-X weighs 320 kg and uses 500 W of electrical power in a volume of 1500 l. A key factor to consider is that there are many clear ways that these can be reduced even further in cold atom devices, some of which will be discussed.

The volumes of the individual components (excluding power supply) are listed in table 5.1. The total volume of these components is 61.1 litres. This is a huge reduction compared to the FG5-X by a factor of nearly 25. The most optimal packaging takes up a larger volume of 120 litres that is 100 litres inside the compensation coils with the additional 20 litres of electronics attached at the back. The greatest improvements here would be achieved through the use of the micro-integrated spectroscopy unit, a reduced number of lasers and further reductions size of the electronics. The weight of the section containing the vacuum chamber, electronics, the optical delivery system and some of the lasers weighs just 53 kg with a further 10 kg added by the frequency chain and spectroscopy

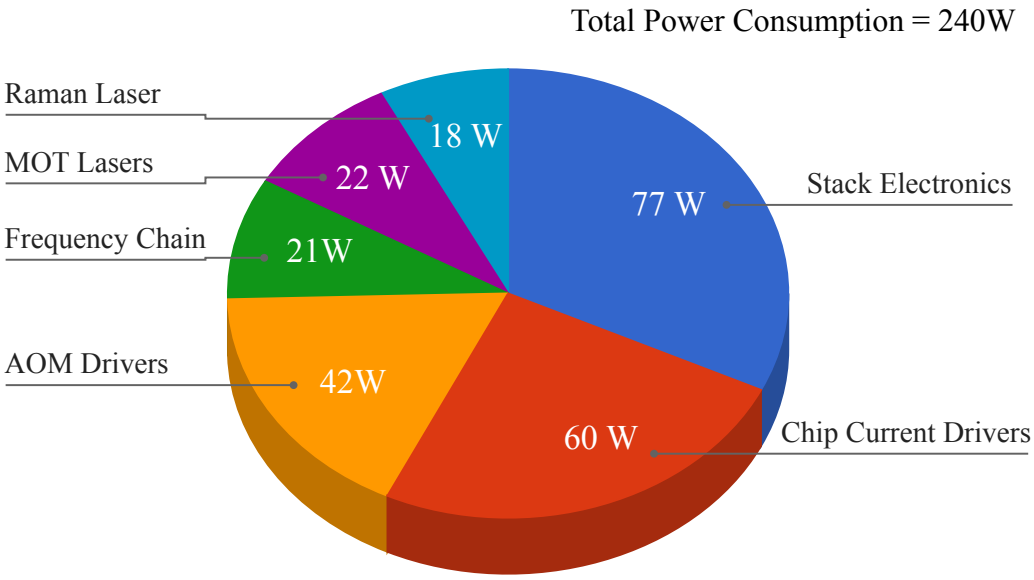

Figure 5.2: Total electronic power consumption of the iSense apparatus during operation separated into key sections, in watts. 'Stack Electronics' includes the base running costs of the electronics, the PC104 computer and the ion pump.

Quantity	**FG5-X**	**iSense**	**FG5-X/iSense Ratio**
Weight	320 kg	63 kg	5.1
Volume	1500 litres	120 litres	24.5
Electrical Power	500 W	240 W	2.1

Table 5.2: Comparison of key features of FG5-X and iSense.

rack units. A total of 63 kg shows a factor of five improvement on the 320 kg FG5-X. Taking into account the transport case that was around 20 kg, this is still a four times weight reduction. The fact that it comes packaged in a single case instead of six and requires no assembly aside from connecting the power supply and the laptop with an ethernet cable (this could be easily replaced by a wireless connection) is an advantage.

The power required to run the iSense apparatus is listed by component area in figure 5.2 and comes to a total of 240 W, less than half of the FG5-X. The largest consumers of power are the chip current drivers and the stack electronics that includes the temperature control of the lasers. The relatively high base running costs of the stack electronics are due to their modular nature and the main draw is the FPGA used on each board. The high current, low voltage generation performed by the chip current drivers is quite inefficient. The comparison to the FG5-X can be seen in table 5.2.

5.2.1 Improvements to Portability in Relation to Future Applications

Different applications of cold atom devices have different constraints on the specifications of the system. For uses such as gravity field mapping and inertial sensing that take place in trucks, submarines and aeroplanes, size and weight are of greater concern than power consumption. However, for space applications power consumption is the biggest concern.

One of the major size constraints in iSense is the vacuum chamber due to the desire for it to be adaptable, the use of the atom chip assembly and the 100 ms free fall time. Single beam magneto optical traps have been demonstrated [93, 94, 95] using reflective gratings or mirror setups and are promising for reducing the size of the vacuum system of a cold atom experiment, but are yet to demonstrate optical molasses temperatures low enough for precision interferometry. Combining these ideas with one of the trapped interferometry schemes described in section 2.2.6 could begin to yield chip scale atom interferometers. A pumpless glass vacuum chamber [96, 97] could be used to reduce the weight of the vacuum system to less than 5 kg. Adding the planned components of the system would increase the portability of the system. The miniaturised spectroscopy setup detailed in section 3.6.2 would remove the need for the rack module where the benchtop version is currently situated. This would reduce the size by 10 litres and the weight by 5 kg.

The current mounting solution contributes almost half of the total weight of the system. The aluminium base and back plates that the vacuum chamber is mounted on are substantial, with a thickness of 5 mm they total nearly 20 kilograms. The aluminium profile that is used to fix the components also add to the volume of the system. 3D printing can be used to create lightweight plates and mounting structures because parts with the same strength can be printed using much less material.

For applications in space such as Earth observation or testing the universality of freefall, power consumption is the biggest problem to overcome. The SSTL-X50 is a compact (and comparatively cheap) satellite platform from Surrey Satellite Technology

Ltd. It is used for many Earth observation missions such as NigeriaSat [98], therefore it would be suitable for a cold atom gravimeter for mapping the Earth geoid. It can carry a payload of up to 91 litres, weighs 45 kg and can supply up to 85 W of power as standard, with higher powers available using additional solar panels. iSense is already a suitable size at 61 litres and close to the required weight at 63 kg that can be easily reduced using the methods mentioned before. However, the 240 W power consumption is on the edge of feasibility.

The main power draws of iSense are the chip current drivers, AOM amplifiers and the stack electronics. The AOMs can be reduced in number by optimising the laser system design, or through the use of a single laser source. The chip current drivers are inefficient because they supply a few amps of current at low voltages (< 1 V). High voltages are more efficient to generate than currents so a redesign of the magnetic field generation is required. Even more compact vacuum systems as previously described could use smaller anti-Helmholtz coils at much reduced currents due to their proximity to the atoms. Due to their modular nature, the stack electronics use a lot of power (77 W). A redesign of the electronics into a single module would remove redundancies in the system such as the multiple FPGAs and reduce overall power consumption – this is possible now that the exact requirements for operation are well understood.

A reduction in the number of lasers would not only save in terms of size and weight, but also power consumption because temperature control is one of the major power draws. Single laser atom interferometry schemes have been realised [99, 100] with telecom lasers at 1560 nm that are frequency doubled. All the required light frequencies are generated using fibre EOMs that use very little power. The advantage of using telecom systems is that they have received a huge amount of funding and so are highly stable. Compact fibre lasers with highly efficient optical power amplifiers are easily available at telecom wavelengths. The main drawback of this method currently is the wavelength conversion from 1560 nm to 780 nm as there are only a couple of companies in the world producing the required fibre coupled conversion modules (NTT, Gooch&Housego). Compared to other

telecom devices the wavelength conversion modules have a low Technology Readiness Level (TRL), meaning that they are not yet ready for widespread deployment in devices.

Clearly, there are obvious ways to improve the already significant portability of iSense even further. This demonstrates how close we are to future uses of quantum sensors outside of the laboratory and in vehicles such as cars, planes and spacecraft.

5.3 Transportation

The apparatus was driven to Brussels and attempts were made to operate it whilst in motion. The extremely compact form factor of iSense and travel via the Eurotunnel allowed us to stay with the equipment at all times, to the extent that we even attempted to run the MOT in the tunnel, although this unfortunately eluded us in both directions. Due to a delay at the border[1], unrelated to the apparatus we were unable to operate the system during the crossing. The UPS repeatedly cut out when driving over bumps in the road. The cause of this was discovered in Brussels to be a loose 'kill switch' wire on the UPS and this was easily repaired. This meant, however, that the experiment was without power for much of the six hour journey to Brussels – a worry for maintaining good vacuum in the chamber as the ion pump would not be running. On the return journey we discovered a broken ground cable meaning that we could not lock the lasers. This was a learning experience in that we now know that for portable experiments we will need to find better methods to attach wires to connectors, reduce the amount of plugging and unplugging we have to do during transport through further size reductions, and better protect the cables from stress. These were only minor issues that were fixed quickly and easily when stationary.

[1]It was actually easier to get two black boxes with cables running between them into France than a Chinese PhD student who, at the insistence of the French border police, we had to leave in their care in Folkestone. He later caught up via a flight from London Heathrow to Brussels.

Figure 5.3: Photomontage showing stages of assembly and transportation of the iSense apparatus from benchtop in Birmingham to portable in Brussels.

Figure 5.4: Photo of the iSense apparatus running a MOT autonomously (shown live on screen to the right) in the West Midlands office in Brussels.

5.4 Operation in Brussels

Upon arrival iSense was unloaded from the van, through the car park and into the office on the sixth floor and we proceeded to check the components. The vacuum returned to 10^{-9} mbar in a few minutes proving that the chamber had survived the transportation, even when operating only on a passive pump. The MOT was regained within an hour after arrival – the time required for the lasers to warm up – with a further hour needed to modify the compensation fields for the new environment to improve its shape and optimise the molasses phase. Figure 5.4 shows the iSense apparatus successfully running a MOT in the office in Brussels. The power supply box is on the left, and the science package in the middle and the large screens on the right were part of the venue itself. We then looked to observe the influence of the Raman laser on the atoms and subsequently recreate the Ramsey fringe pattern we found in Birmingham. Some further optimisation of the molasses using the compensation coils was done. It was difficult to regain the same level of compensation achieved in Birmingham before packaging. This might be due

to the isolators in the laser boxes and all the electronics close to the vacuum chamber causing varying magnetic fields near to the atoms. Magnetic shielding of the vacuum chamber is recommended for future portable tests. The Raman laser system required some recoupling to regain the amount of power needed and corrections to the polarisation were made, however atom interferometry was observed with very little further effort required. An additional brief demonstration was performed at the Royal Society venue of Chichely Hall, near Milton Keynes, during the transportation back from Brussels to Birmingham. For this final demonstration only two people were used to move and operate the system, thus showing that we are moving closer to a truly one-man portable device.

5.5 Summary

The entire system has been packaged from a setup occupying an optical table into a portable configuration of dimensions 100 cm $\times$ 90 cm $\times$ 70 cm with the main science package weighing just 63 kg in a volume of 120 litres. The system fits inside a large car/small van, it is capable of being transported by two people, and operated only by a single person. The iSense device is evidence that a quantum technology system can be made portable. The goals of operating a device of this kind on a plane, truck or spacecraft have been discussed and are within the grasp of quantum devices in the near future with iSense being a key factor in demonstrating that this can be possible.

The iSense device in its fully portable configuration has been successfully demonstrated to the European Commission and the UK quantum technology community to much enthusiasm. Seen by many government and industry figures as a key demonstration of the future capabilities of quantum technologies, it has contributed greatly to the awarding of the UK Quantum Technology Hub in Sensors and Metrology to the University of Birmingham [1]. The sizable reduction from a laboratory full of optics and electronics for typical quantum experiments is one thing, but iSense is also of a similar scale to even 'classical' devices with clear improvements that can be made to increase portability and usefulness

[1] www.birmingham.ac.uk/qthub

even further.

The system has been operated successfully after transportation and has performed atom interferometry outside of the laboratory in an office 570 km from its origin. The detailed results of the operation of the instrument both before and after transportation are presented in the following chapter.

CHAPTER 6

COLD ATOM AND INTERFEROMETRY RESULTS

The ultimate test of whether the novel components outlined in the previous sections can come together and provide a platform for portable cold atom systems is, of course, cooling atoms and then manipulating them. The realisation of the Magneto-Optical Trap (MOT) of ^{87}Rb inside the Birmingham vacuum system using the atom chip assembly, the FBH lasers and the stack electronics was the first step. The first MOT created is shown in figure 6.1.

Once this was achieved, the focus shifted to observing the cold atoms undergoing Rabi oscillations under the influence of the Raman laser. Atom interferometry sequences were performed and Ramsey fringes that describe the microwave transition in ^{87}Rb were measured. The results of the measurements performed after transportation to Brussels are also presented, demonstrating the robustness and portability of the experiment.

The two main characteristics of a cold atom cloud that are of interest in this experiment are the number of atoms contained within the cloud, and its temperature. The more atoms we have at a low temperature, the better the interferometry signal will be.

6.1 Experimental Sequence

The complete experimental sequence that was used to perform a Ramsey atom interferometer is shown in figure 6.2, beginning after the loading of the MOT. It shows the

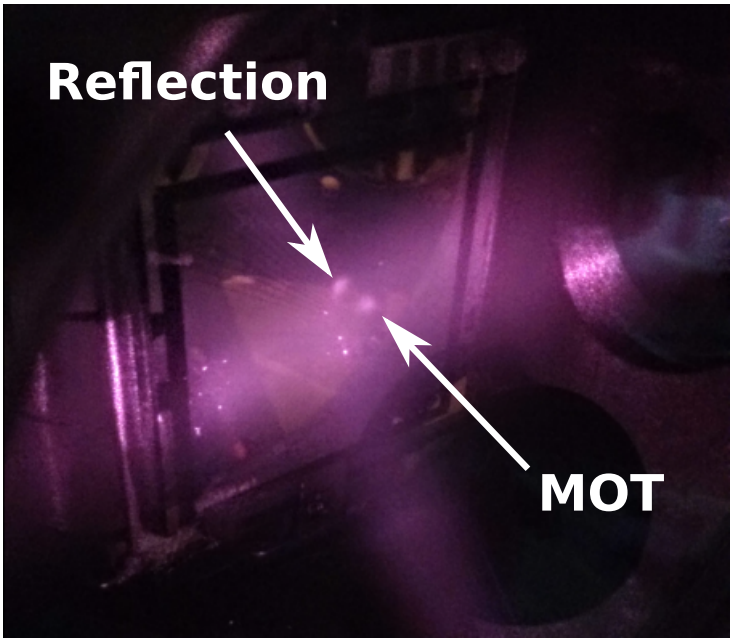

Figure 6.1: Photograph of first MOT obtained in iSense chamber. The MOT beams are visible due to fluorescence of ^{87}Rb in the beam path and the small detuning at the time. The MOT and its reflection in the chip surface can be seen as bright spots in the centre of the image.

frequencies and intensities of the lasers and power in the coils, along with the length of time each was on for. It consists of a MOT loading phase with the MOT coils on and lasers at cooling and repumper frequencies. Then the coils are switched off and an optical molasses phase is used to cool the atoms further involving frequency and intensity manipulation of the MOT beams. The cooling and repumper light is then switched off for the interferometry phase. A Ramsey interferometer is constructed involving two pulses of the vertical Raman beam. The detection then takes place.

6.2 The Mirror-MOT

The cooling and trapping techniques described in chapter 2 were implemented to create a cold atom cloud that was used as the test object for the atom interferometer.

Four MOT beams containing both cooling and repumper frequencies were used, each with a diameter of 16 mm and a power of 10 mW. This gave an average intensity at the intersection of $I_{\text{total}} = 30\ \text{mW}\,\text{cm}^{-2}$. Using a magnetic field gradient of 10 $\text{G}\,\text{cm}^{-1}$, the

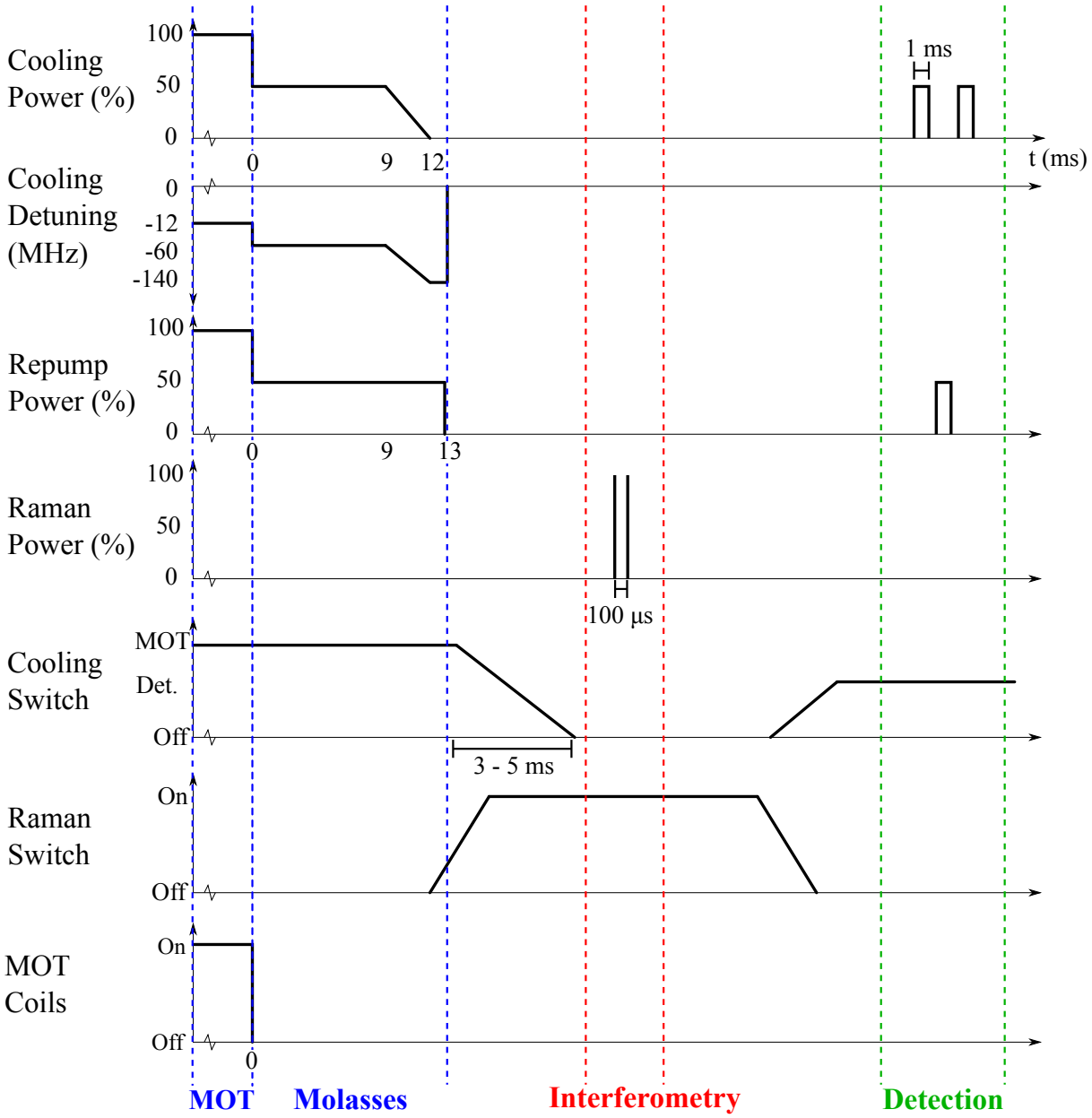

Figure 6.2: The full timing sequence of the experiment showing laser frequencies and intensities for each section. $t = 0$ is at the end of the MOT phase that lasted for 2.3 s. This is followed by 12 ms of optical molasses and then the interferometry phase. Depicted is the sequence used for Ramsey interferometry; a gravity measurement would use at least three pulses of Raman light over a total time of 100 ms or more. The final section is the detection of the state after the interferometer.

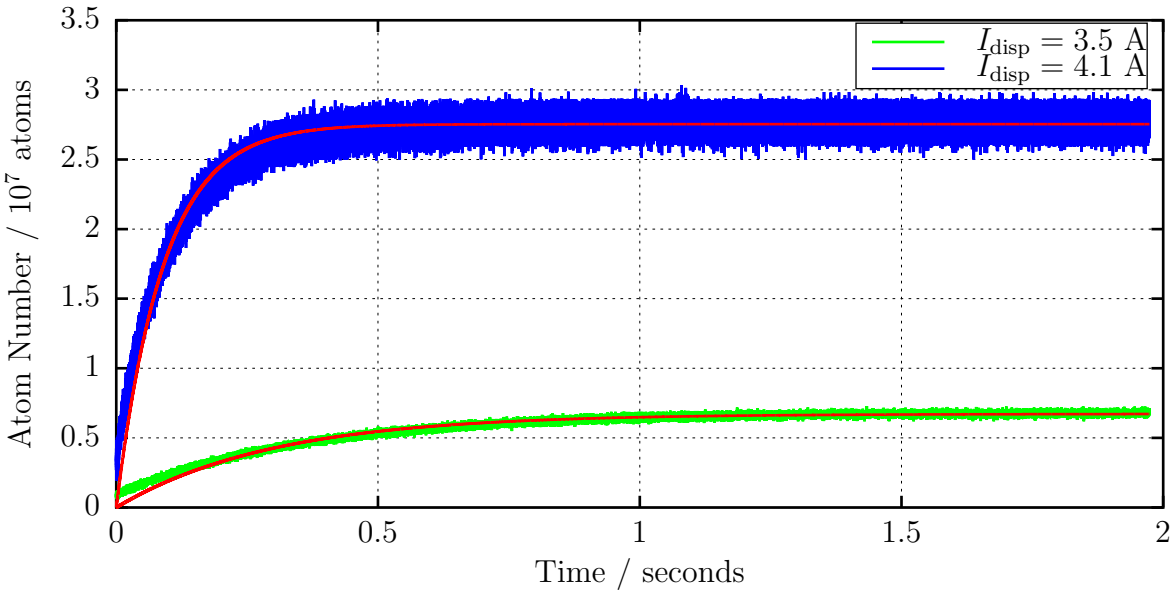

Figure 6.3: MOT loading curve from fluorescence with photodiode for two different values of dispenser current.

detuning of the cooling light was changed to find the value that gave the cloud with the highest optical density. The best value was found to be 12 MHz lower than the $|F = 2\rangle \rightarrow |F' = 3\rangle$ transition, a detuning of -2Γ where Γ is the linewidth of the transition. The repumper laser was set on resonance with the $|F = 1\rangle \rightarrow |F' = 2\rangle$ transition throughout.

6.2.1 Measurement of MOT Loading Rate by Fluorescence

Adjustments to the alignment of the beams, the amount of rubidium in the chamber and the magnetic field changes the rate at which atoms are loaded into the MOT. A photodiode was used to measure the fluorescence of the MOT as atoms were collected, the details of which – including the conversion from photocurrent to atom number – can be found in appendix B.1. Two loading curves, recorded with optimal beam alignment, are shown in figure 6.3 for two different dispenser current; 3.5 A and 4.1 A. The red lines show fits to the datasets using the function

$$N(t) = N_{\text{eq}} \left(1 - \mathrm{e}^{-\frac{t}{\tau}}\right), \tag{6.1}$$

where N_{eq} is the atom number at equilibrium and τ is the 1/e loading time in seconds for times greater than or equal to zero. This arises as a solution to the MOT loading rate equation

$$\frac{dN(t)}{dt} = \alpha P_{\mathrm{Rb}} - (\beta P_{\mathrm{Rb}} + \gamma)\, N(t), \tag{6.2}$$

in which α is the trapping cross-section of the MOT, β is the cross-section for collisions with the background rubidium atoms and γ is the rate of loss for collisions with non-rubidium atoms. P_{Rb} is the rubidium partial pressure in the vacuum chamber. The terms on the right hand side of equation (6.2) are αP_{Rb} that describes the rate at which atoms are added to the MOT from the background vapour, $\beta P_{\mathrm{Rb}} N(t)$ and $\gamma N(t)$ give the loss rates due to collisions with rubidium atoms and non-rubidium atoms respectively [101].

The blue data is for a dispenser current of 4.1 A; this gave the fastest loading rate and the highest final number of atoms. At this current the MOT loads to $(2.75 \pm 0.18) \times 10^7$ atoms in 350 ms. This current will be used for performing gravity measurements due to the increase of the signal to noise ratio granted by the higher number of atoms available for the interferometer, adding a 150 ms interferometry phase to this loading time will allow for a repetition rate of 2 Hz when operating as a gravimeter.

The other data shows the results using a reduced dispenser current of 3.5 A. This current was used for the optimisation of the system due to the desire to prolong the life of the dispenser. The remaining results in this chapter were performed at this setting. At a dispenser current of 3.5 A, the MOT loads for 2 s reaching a final atom number of $(6.7 \pm 0.7) \times 10^6$ atoms.

6.2.2 Absorption Imaging of the MOT

Using a beam of light that was on resonance with the cooling transition and a CCD camera, absorption images of the MOT were taken to measure its properties.

An absorption image taken 3 ms after the switch-off of the MOT with a 5 µs pulse

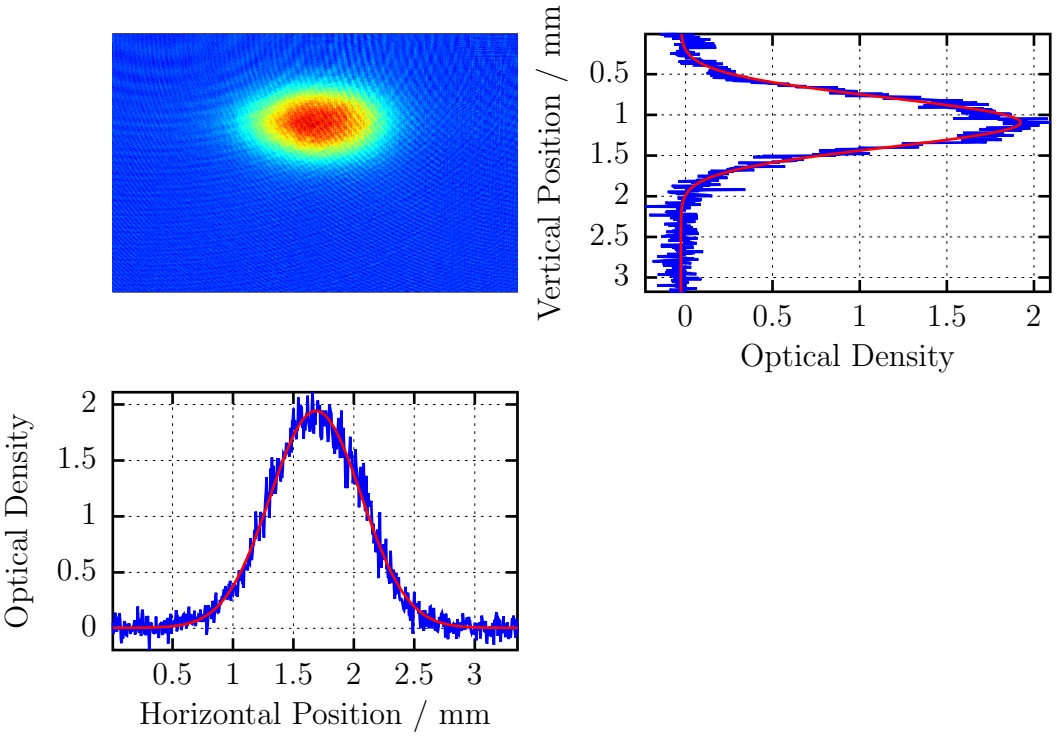

Figure 6.4: False colour absorption image of the MOT after 3 ms of freefall time along with cuts in both axes along the centre. The optical density yields an atom number of 7.15×10^6. The dispenser current used was 3.5 A, the MOT field gradient was 10 G cm^{-1} and the cooling beam detuning was -2Γ.

of detection light is shown in figure 6.4. The dispenser current used was 3.5 A, as stated previously. The 3 ms delay is due to the speed of the fibre switch used to transfer the light from the MOT ports to the detection port. Two one-dimensional slices are taken from the 2D image perpendicular to each other and show the profile across the centre axes of the cloud. A fit with a 1D gaussian was performed to get the peak optical density and size of the cloud. The cloud has a $1/e$ diameter in the horizontal direction of $\sigma_x = 0.66$ mm and $\sigma_y = 0.75$ mm in the vertical, the elongated shape is usual for a mirror-MOT. It has a peak optical density of 1.98 in the centre. The optical density was integrated over the entire cloud and converted (for the conversion from optical density to atom number, see appendix B.2) to get the total number of atoms $(7.15 \pm 0.18) \times 10^6$ atoms. This is within errors of the value recorded by fluorescence imaging ($(6.7 \pm 0.7) \times 10^6$), and acts as a confirmation that the conversion from photodiode voltage to atom number is correct.

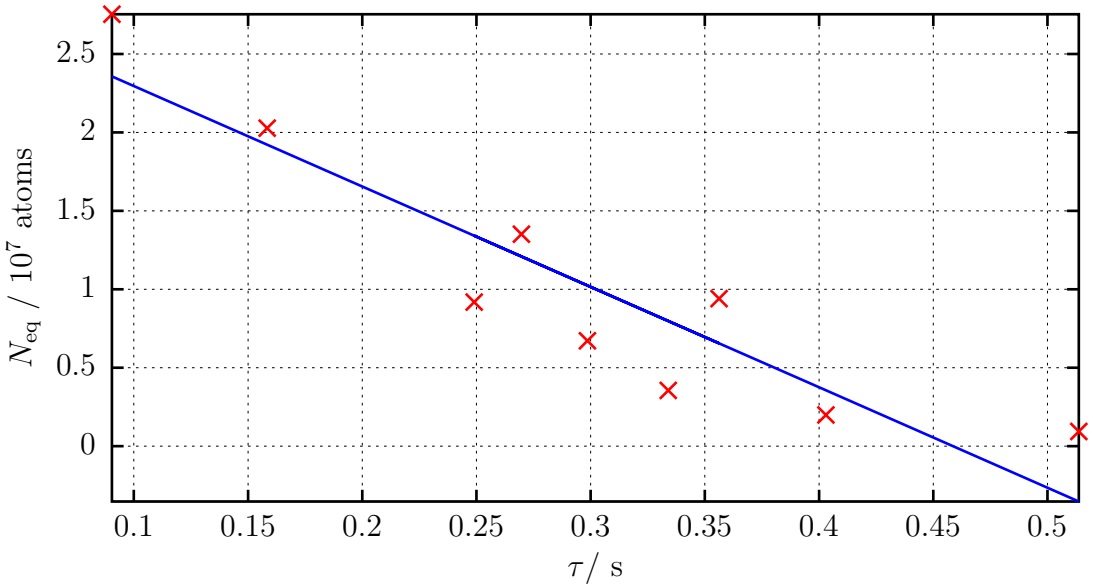

Figure 6.5: Plot of number of atoms in trap at equilibrium, N_{eq}, against the 1/e MOT loading time, τ, in seconds.

6.2.3 Pressure measurement with the Mirror-MOT

The loading time and final atom number can be used to calculate the pressure in the vacuum chamber at the location of the MOT. As there is only a small conductance path between the ion pump and the centre of the chamber, this method can be used to check the values of pressure given by the ion pump controller. The method that was used is described in [101], it is capable of separating the pressure caused by the rubidium vapour and that from the residual background gases. The current applied to the dispensers was changed and the loading curves recorded. The final number of atoms reached at equilibrium N_{eq} and the 1/e loading time, τ, as in equation (6.1) for each curve were calculated and plotted against each other. The result is shown in figure 6.5, and the data was then fitted with

$$N_{eq} = \frac{\alpha}{\beta}(1 - \gamma\tau)\,. \tag{6.3}$$

which arises from (6.1) and (6.2), while removing P_{Rb} [101].

The fitted values from (6.3) are used to extract the pressure due to rubidium and the

background. The ratio α/β gives the highest value of N_{eq} that is possible due to the partial pressure of rubidium in the system. γ can be used to find the pressure due to non-rubidium atoms. This was extracted from the relation $\gamma/P_{\mathrm{base}} = 3.7 \times 10^7$ Torr^{-1} s^{-1} from [102], assuming that the main particles remaining are hydrogen. This gives a value for the non-rubidium partial pressure (or base pressure) of

$$P_{\mathrm{base}} = 5.9 \times 10^{-8} \text{ mbar}.$$

By comparison, the reading on the ion-getter pump controller during this measurement was 2×10^{-8} mbar. This base pressure value is important to know because it sets the limit of the lifetime of the MOT that can be achieved in our system.

6.2.4 Mirror-MOT temperature measurement

The temperature of the cold atom cloud was measured using time of flight imaging, where the size of the cloud is recorded at different times after being dropped. The velocity distribution of the cold atom cloud at µK temperatures can be described by a Maxwell-Boltzmann distribution. As it evolves in time after being released from the trap, the distribution of the cloud – regardless of its initial shape – will become Gaussian. The rate at which the cloud expands gives an indication of the kinetic energy of the atoms, and thus its temperature, T by

$$\sigma_{\mathrm{f}}^2 = \frac{k_{\mathrm{B}}T}{m}t^2 + \sigma_{\mathrm{i}}^2 \tag{6.4}$$

where m is the mass of an atom, k_{B} is the Boltzmann constant, $\sigma_{\mathrm{i,f}}$ are the initial and final standard deviations of the cloud – assuming that it is Gaussian – and t is the free fall time.

In this case we used absorption imaging with a CCD to take images at millisecond intervals after releasing the cloud from the trap. Since this is a destructive method of imaging, the cold atom cloud will be destroyed by the detection light and has to be

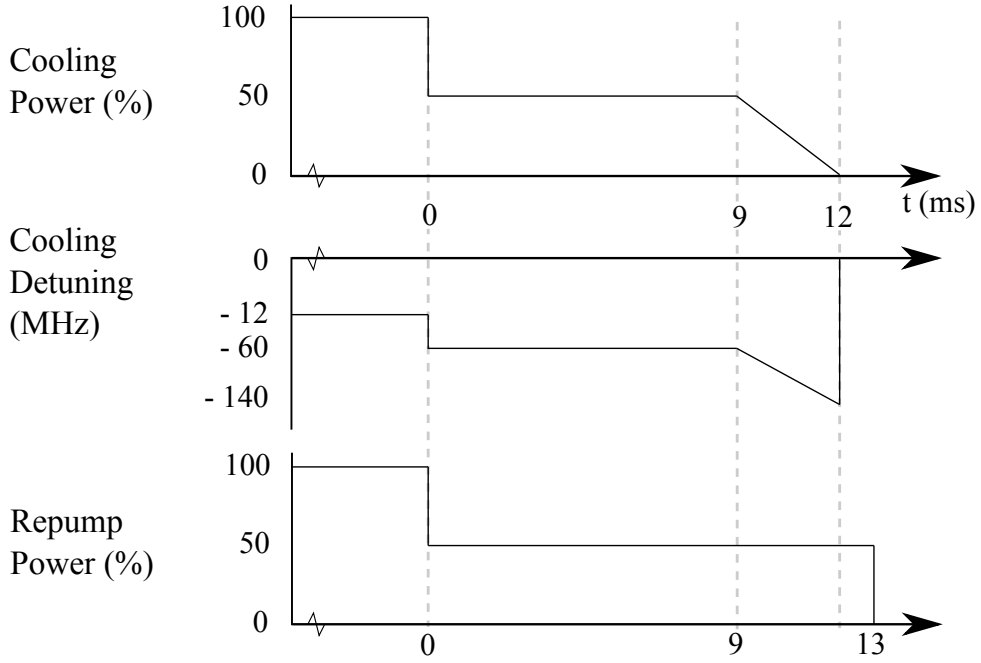

Figure 6.6: Sequence showing laser power and detuning involved in optical molasses phase to reach sub-10 µK cloud temperatures. Repumper detuning was constant at 0 MHz

reformed after each measurement. As for the optical density measurements, projections were taken across the centre of the cloud in two dimensions and a Gaussian was then fitted to them to extract the standard deviation along both axes.

The values of σ^2 were plotted against t^2 for the horizontal expansion and fitted with (6.4). The temperature was extracted from the gradient of the fit giving a value in the horizontal direction of 152 ± 19 µK. In the vertical direction the result was 167 ± 11 µK giving an average temperature of

$$T_{\mathrm{MOT}} = 161 \pm 11 \text{ µK}. \tag{6.5}$$

This is just above the Doppler limit for ^{87}Rb of 145 µK and is a typical temperature found in a MOT [103, 104].

6.3 Optical Molasses

The MOT gives a dense cloud with a high number of atoms at a relatively high temperature of 160 µK. To reach a temperature below tens of µK that is suitable for atom interferometry purposes, an optical molasses (section 2.1.1) phase was used. During this phase, the magnetic field used for the MOT was turned off and only the cooling and repumper light remained.

Optimisation of the optical molasses involves finding the best values for detuning, beam intensity and duration, along with the best way to perform changes, whether by stepping, jumping or ramping the values. The background magnetic field also has to be well compensated by applying an opposing field, as this limits the final temperature.

The MOT coils were switched off first, leaving the cooling and repumper light on. The detuning of the cooling laser was increased to -12Γ and the power reduced to 50% for 9 ms before ramping the intensity to zero and detuning to -23Γ over 3 ms. The repumper was left on for an extra millisecond to prepare the atoms in the $|F = 2\rangle$ state. The efficiency of this transfer was verified by detecting on the $|F = 2\rangle \rightarrow |F' = 3\rangle$ transition with and without this extra 1 ms of repumper light. This was then cross-checked by using a pulse to blowaway the atoms in the $|F = 2\rangle$ level followed by a repumper to move any atoms that were left in the ground state to the upper state before finally performing the detection of the upper state.

6.3.1 Optical Molasses Temperature Measurement

The expansion of the cloud in the horizontal direction as a function of freefall time is presented in figure 6.7, which shows a comparison between the temperature of the cloud after the MOT phase and then after a fully optimised optical molasses. Each point is an average over five measurements and the error bars show the standard error of the values [105].

The rate of expansion is clearly much faster after only the MOT, the cloud becomes

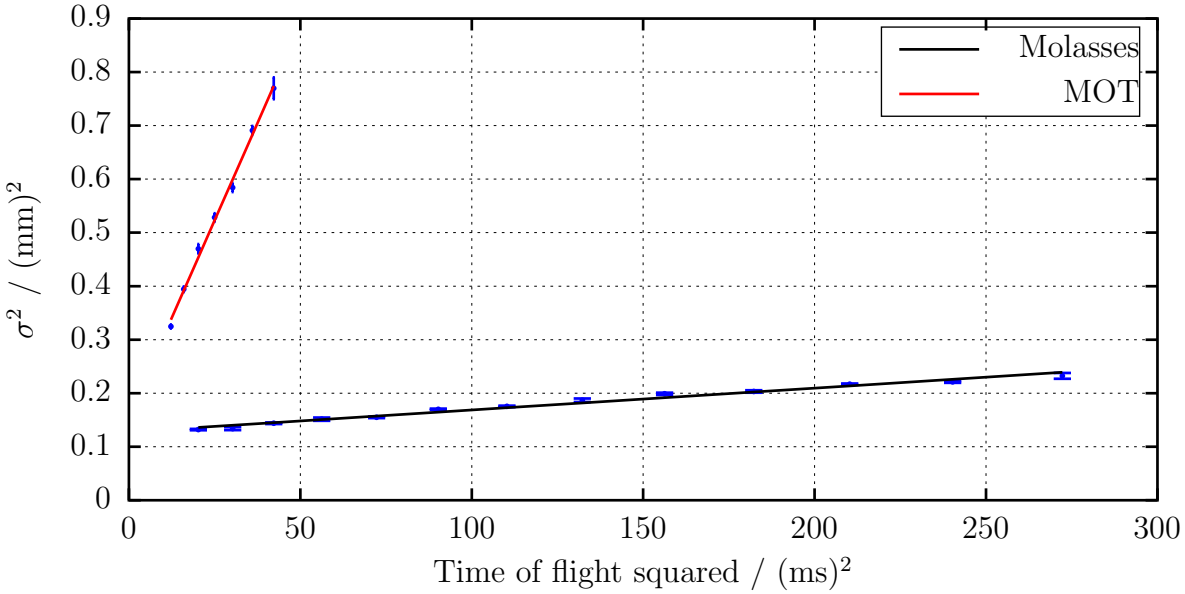

Figure 6.7: Comparison of the expansion of the cold atom cloud after MOT phase and optical molasses phase. Plotted is the standard deviation squared (σ^2) of a Gaussian fit to absorption images of the cloud in the horizontal direction, against the time of flight squared (t_{tof}^2). Each point is the average of five measurements and the error bars are the standard error of the data [105]. A clear difference can be seen in the expansion of the cloud after the two different phases. The MOT temperature is around 160 µK and the best molasses temperature is around 4 µK.

undetectable at $t_{\text{tof}} = 6.5$ ms since its density becomes too low. The optical molasses phase reduces the temperature of the atoms cloud a substantial amount to just 4.2 ± 0.5 µK, evident by the much longer times that the cloud is visible for. The corresponding data for the vertical direction give a temperature of 4.6 ± 0.3 µK. The averaged temperature after the optical molasses is thus

$$T_{\text{OM}} = 4.4 \pm 0.3 \text{ µK}. \tag{6.6}$$

This temperature result shows that our atom chip setup can easily produce cold atom clouds that are suitable for atom interferometry experiments. Non-chip-based, non-BEC atom interferometers typically aim for $1 - 2$ µK. Temperatures much lower than the 4.4 µK achieved will be hard to reach because it requires extremely good compensation of the magnetic field, a task made more difficult by the proximity of the atoms to the metallic structures of the chip assembly. As the wavefront across the Raman beam is not perfectly uniform, for precision measurements a colder cloud is usually desired so that the atoms see the same section of the beam front at each Raman pulse.

The next step in most cold atom gravimeters is to perform velocity selection using a long ($20 - 50$ µs) Raman pulse. This takes a small section of the cloud with a velocity spread corresponding to nanokelvin, in the direction of the Raman beam. This velocity selection is performed with a Raman pulse with a frequency width smaller than those used in the interferometer to ensure that these atoms will remain on resonance during the sequence. The colder the initial cloud, the more atoms will be selected with this pulse and a balance has to be struck between atom number and temperature. It is planned and expected that iSense will use this method when optimising the gravity signal.

6.3.2 Analysis of Chip Molasses Temperature

It is believed that the optical molasses temperature recorded here is the coldest ever reported using an atom chip setup, with an average temperature of 4.4 ± 0.3 µK. Other

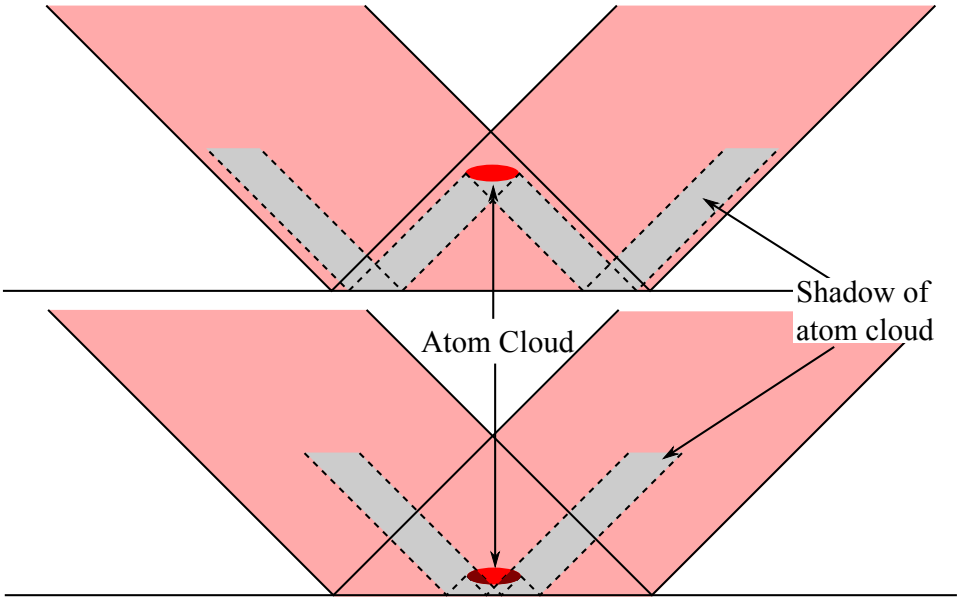

Figure 6.8: Depiction of shadow cast by cold atom cloud (red oval) as possible reason behind low optical molasses temperature. The upper drawing shows the cloud as in this experiment, far from the chip surface. The lower image shows the cloud much closer to the chip, sections of the cloud are shadowed by other parts of itself (dark red sections).

atom chip experiments, even after optimisation, do not reach lower than around 8 µK [106, 107, 103]. It must be noted that these experiments perform further cooling through alternative methods to create Bose-Einstein Condensates and as such little emphasis is usually placed on cold optical molasses.

The main difference between these experiments and iSense is that the cold atom cloud is generated at a distance of 5 mm from the surface of the chip, while the others are at 1-2 mm. This larger distance could mean that the light that is reflected from the chip surface has a better beam quality. Since small magnetic field gradients could still be present in the chip assembly, even with non-magnetic materials, the increased distance could reduce the effect of these fields. The benefit of this is that the magnetic field can be better compensated in this region.

The larger cloud to chip separation could also prevent the cloud from casting a shadow on itself as depicted in figure 6.8. This would cause an imbalance in the forces of the optical molasses phase across the entire cloud, thus preventing low temperatures being reached.

Further verification of the temperature of the cloud will be achieved by performing a

velocity-selective launch and observing the fraction of the cloud that is launched [108].

6.4 Atom Interferometry

Now that the atoms have been cooled to a low enough temperature, we can proceed with performing atom inteferometry. This requires precise control of the Raman beam down to the microsecond time scale, precision on the frequency difference between the two Raman beams that is below 1 kHz, and with no (or very small) laser frequency, intensity and polarisation changes.

The first step towards atom interferometry is to observe an influence of the Raman beam on the atoms. As discussed in chapter 2, a two-photon Raman transition is a cyclic process whereby the atom undergoes Rabi oscillations between the two hyperfine ground states via a third 'intermediate' state when subject to a light field. By varying the length of the pulse, the population distribution in the two hyperfine ground states changes with a period that is governed by the intensity of the beam and its detuning from the $|F = 1\rangle$ level in the $^5\mathrm{P}_{3/2}$ excited state. Once this oscillation period is known, then the Raman beam can be used to control the superposition of the two states to construct an interferometer.

6.4.1 Interferometry Sequence

The sequence of cooling, repumper and Raman light pulses used for the interferometry phase is shown in figure 6.9 along with a representation of the distribution of the atoms between the two hyperfine ground states. At the end of the optical molasses phase, the repumper light was left turned on for 1 ms so that the atoms were prepared in the $|F = 2\rangle$ level. The atoms at this stage are distributed through all five m_f states within $|F = 2\rangle$. The Raman beam was then applied for pulses of microsecond timescales in the Doppler insensitive mode (both beams from in the same vertical direction and circularly polarised). This co-propagating mode addresses the atoms regardless of their motion and therefore

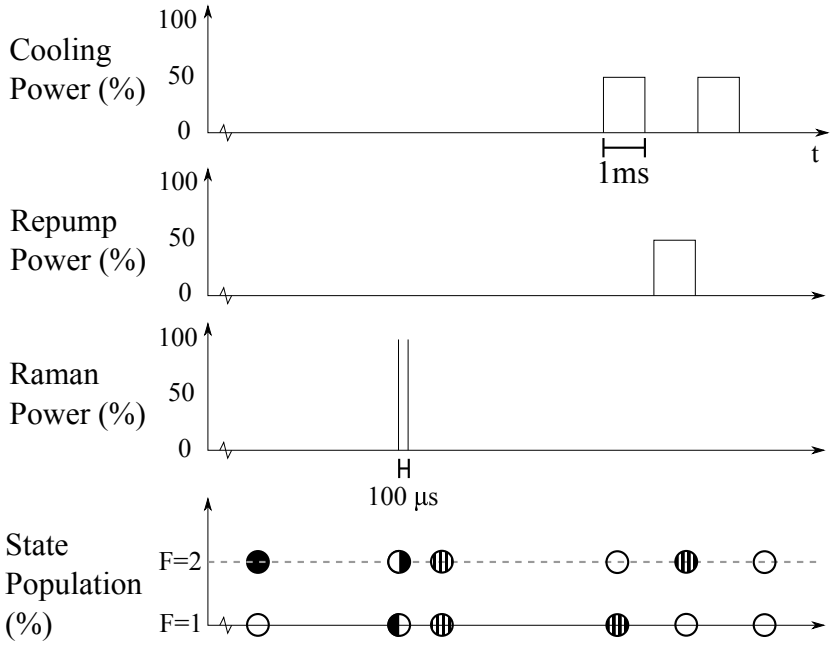

Figure 6.9: Ramsey interferometry sequence. The method for observing Rabi oscillations is identical except that the second of the two Raman pulses is removed. The lowest diagram shows the approximate distribution of the atoms between the two ground state hyperfine levels.

increases the observed signal. This Raman pulse had the effect of transferring atoms from the starting level of $|F = 2\rangle$ and into the previously empty $|F = 1\rangle$ hyperfine ground level. We chose the atoms in the $m_{\rm f} = 0$ magnetic sublevel to be addressed by the Raman laser because it is insensitive to magnetic fields[1]. This was achieved because the frequencies of the $m_{\rm f}$ levels in our system were separated by the Zeeman effect created by a non-zero magnetic field. This meant that a maximum of a fifth of the total number of atoms could be transferred with a π pulse.

After the Raman pulse a 1 ms blowaway on the $|F = 2\rangle \rightarrow |F' = 3\rangle$ transition was used to remove the non-transferred atoms. A further 1 ms of repumper light was used to move the atoms transferred by the Raman pulse into the detectable $|F = 2\rangle$ level and then fluorescence imaging was performed with a 1 ms pulse of detection light. This method of moving atoms between states was chosen because it gave a decreased shot-to-shot noise.

[1]This is true to first order since the energy shift of the hyperfine level for weak magnetic fields is given by $\Delta E = \mu_B g_F m_{\rm f} B\hbar$, and clearly $\Delta E = 0$ for $m_{\rm f} = 0$, see section 2.1.2 and [55].

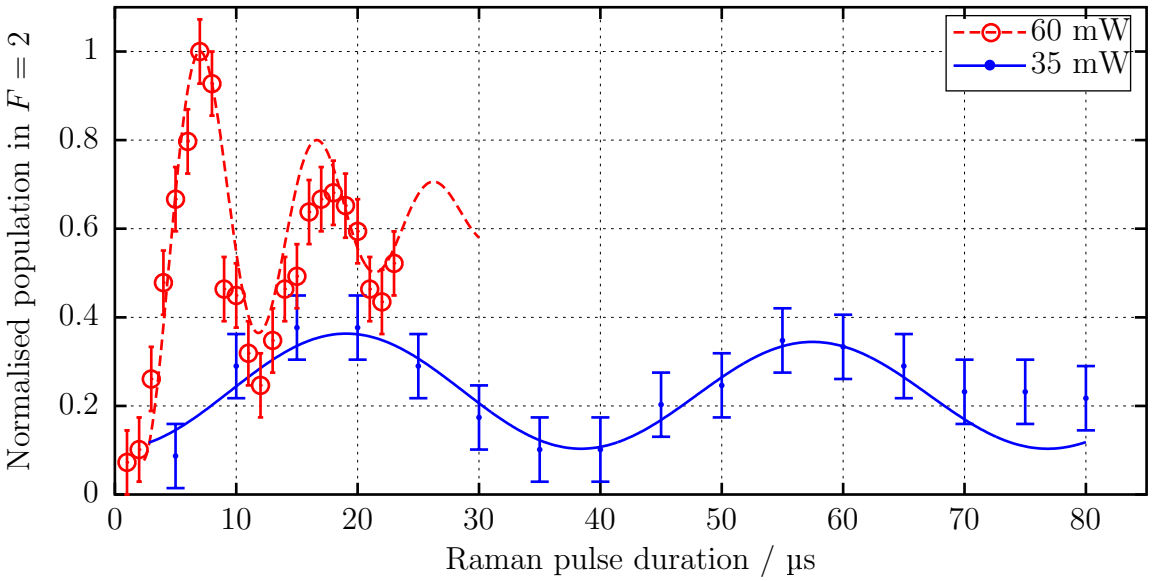

Figure 6.10: Rabi oscillations observed using two different values for power in the Raman beam at a detuning of −1.5 GHz. The red circle and dashed line were recorded using a total beam power of 60 mW and show a fitted Rabi frequency of 505 kHz. The blue points are for 35 mW and show a lower oscillation frequency of 164 kHz.

6.4.2 Rabi Oscillation Results

The first observations of Rabi oscillations in the iSense chamber are shown in figure 6.10; the values shown are normalised to the largest photodiode signal that was recorded during the measurement. The intensity of the Raman laser was fixed and the length of the pulse varied. The ratio of the Raman sideband to carrier frequency was chosen to be equal. The Raman laser was set at a detuning of 1.5 GHz, verified using a wavemeter. The red circles show a total Raman beam power of 60 mW used that corresponds to a power of 20 mW in each of the three frequencies in the beam. The Raman pulse length was increased in steps of 1 µs until the signal degraded at 23 µs. A damped version of the probability of finding atoms in this state after a Raman pulse (see equation (2.13)) was fitted to the data and is shown as the red dashed line for the high power data and as the blue line in the case of the low power. The fitted Rabi frequency for the high power is 505 kHz, corresponding to a π-pulse time of 6.2 µs. The blue trace shows the same for a lower beam power of 35 mW. In this case, the pulse length was increased in steps of 5 µs. The fitted Rabi frequency for this data is much lower and has a value of 164 kHz, yielding a

π-pulse length of 19 µs. The beam powers used for the measurements in this chapter were set using the same power meter (PM100D, Thorlabs) and the resulting Rabi frequencies show a possible inaccuracy in our power meter. Using the two-photon Rabi oscillation theory from section 2.2.1 and [61], the Rabi frequencies of 505 kHz and 164 kHz observed here relate to calculated total beam powers of 48 mW and 20 mW respectively.

The data for the high power Raman pulse shows a large first peak followed by a sharp decay. The population transfer that was observed past this point was no longer two-photon Raman transitions, but dominated by spontaneous emission of the atoms due to the high laser intensity. This was observed to be the case as the population transfer occurred even when the two-photon detuning of the Raman beam was changed by a megahertz. A true Rabi oscillation caused by the Raman beam vanishes if the two-photon detuning is changed by this much because the length of the Raman pulse gives the frequency width inversely proportional to the pulse length. For example, a pulse with $\tau = 10$ µs has a frequency width of 100 kHz.

For this reason, the beam power used for the following interferometry measurements was chosen to be 35 mW, again measured using the same power meter as before. Although this has a lower transfer efficiency; the errors due to spontaneous emission are reduced. For large detunings ($\delta \gg \Gamma$), the scattering rate from the upper level – which leads to spontaneous emission – can be approximated [52, p.199] by

$$R_{\text{scatt}} \simeq \frac{\Gamma}{8}\frac{\Gamma^2}{\delta^2}\frac{I}{I_{\text{sat}}}, \tag{6.7}$$

which scales with beam intensity, I, and detuning as δ^{-2}. Finding an optimum between the intensity and detuning that provides a useful Rabi frequency (see (2.14)) and reduces spontaneous emission is key. The shallower gradients of the oscillations at lower power also mean that errors in pulse duration have a smaller effect on the population transfer.

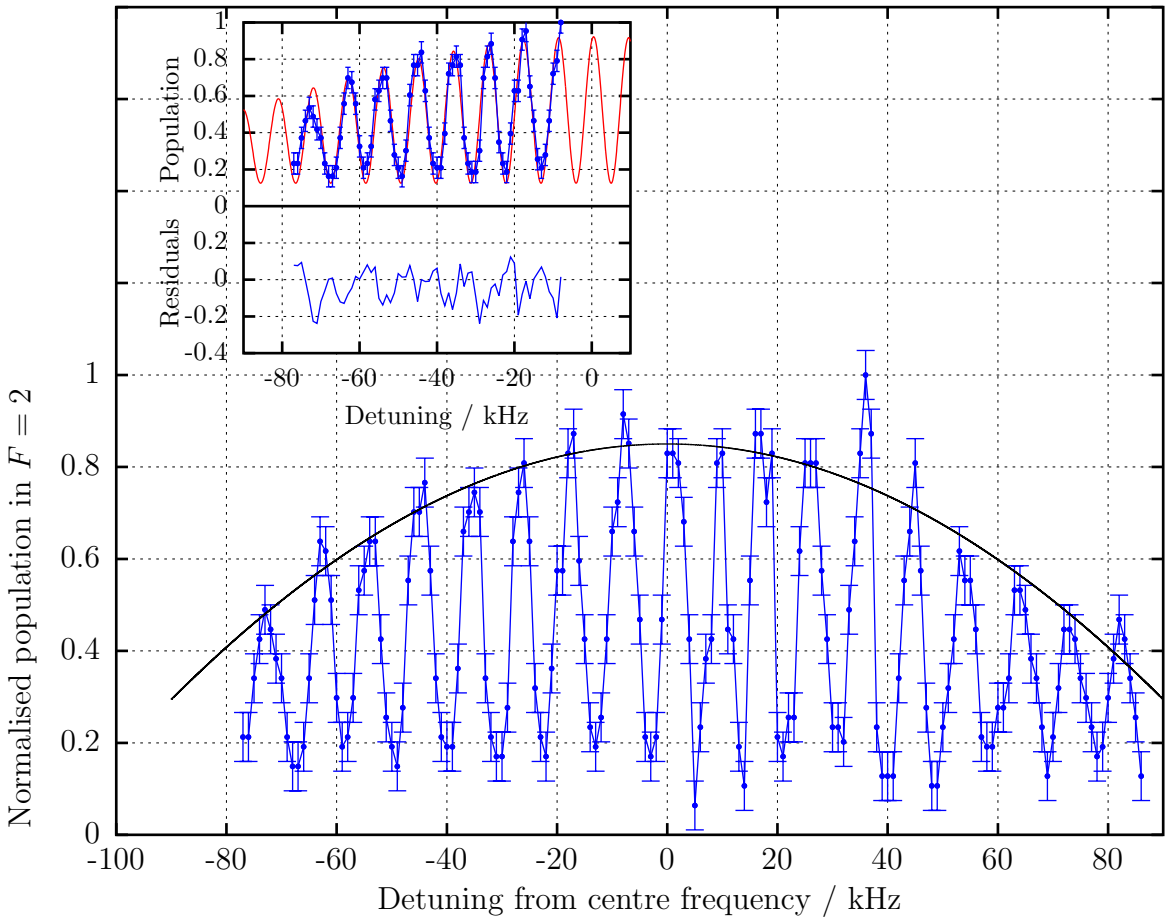

Figure 6.11: Observation of Ramsey fringes in the laboratory for the ^{87}Rb hyperfine ground state splitting with two 9 µs $\pi/2$ pulses separated by 100 µs. The black line is a fit of the envelope governed by the $\pi/2$ pulse length and yields a value of $\tau = 11.1 \pm 0.1$ µs. Inset shows a partial fit (red line) of the fringe using equation (2.15) and a plot of the fit residuals. The χ^2 value of the fit is 1.4, indicating a good agreement with the data [105].

6.4.3 Ramsey Interferometer

The power of the Raman beam was set to 35 mW and the pulse length was chosen to be $\tau = 9$ µs. This corresponds to a $\pi/2$-pulse for this laser power – as seen in the Rabi oscillation results – and so the atoms are prepared in a 50:50 superposition of both states. Using a co-propagating configuration with a circularly polarised beam directed from the upper port of the vacuum chamber, two pulses separated by $T = 100$ µs were used to perform a Ramsey interferometry sequence. Since the momentum transfer to the atoms is small, the interferometer can be closed with only two pulses because the two paths of the interferometer do not diverge spatially during the time frame of the sequence. The frequency applied to the EOM for generating the Raman sidebands was shifted in steps of 1 kHz using the DDS around the central frequency of 6.834 GHz.

The observed Ramsey fringes can be seen in figure 6.11, each point is a single measurement and the errors depicted are the systematic uncertainties on reading the measurement from an oscilloscope. The black line is a fit to the envelope that the fringes are contained in. As described in section 2.2.3, this envelope is governed by the length of the pulses. The fitted curve gives the pulse length as $\tau = 11.1 \pm 0.1$ µs, a difference from the value that was set of 2 µs. This difference could be due to the fact that the Raman laser was operating unlocked and so its detuning was not constant during the measurement period (approximately 45 minutes). This causes a change in the effective Rabi frequency, and subsequently the amplitude of the fringes as described in (2.15).

The inset in figure 6.11 shows a partial fit of the fringe data using equation (2.15). A partial fit was used in this case – instead of a fit to the entire fringe – to minimise the effect from the drifting Raman laser detuning. The fit returns a pulse length of $\tau = 11.4$ µs, comparable to the envelope fit performed above and a pulse separation time of $T = 105$ µs. This is a 5 µs difference from the set value which could be caused by an AOM switching delay as it is just over twice the difference seen between the set time of a single pulse and the fitted pulse length. The residuals are also plotted, from which a value of $\chi^2 = 1.4$ was calculated [105] that represents a good agreement between the fit and the data.

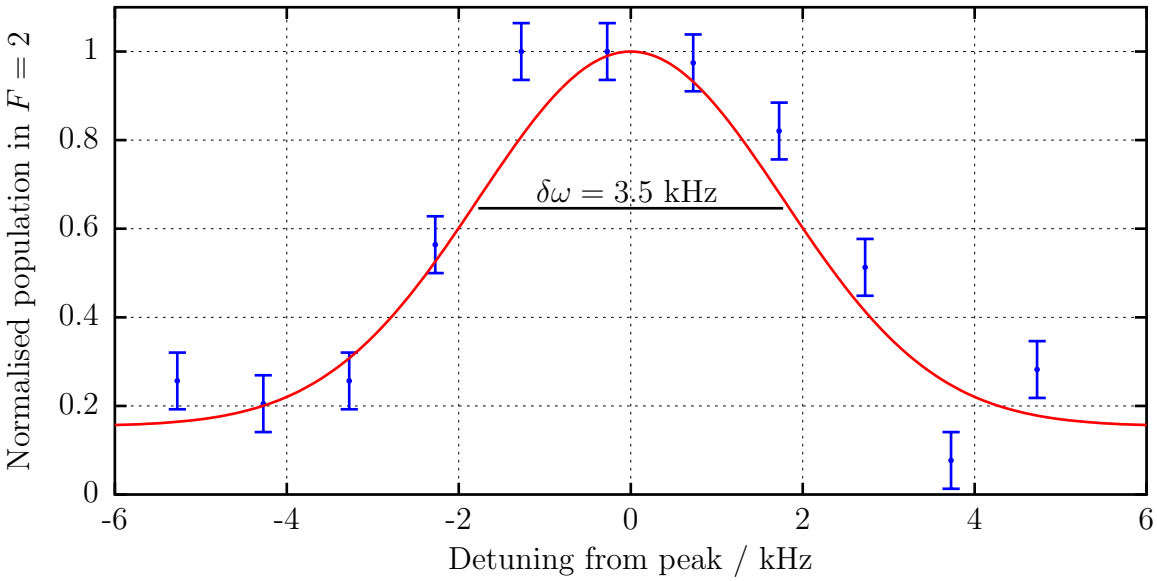

Figure 6.12: Gaussian fit to the central Ramsey fringe of the ^{87}Rb hyperfine splitting obtained in Birmingham.

A Gaussian fit of the central fringe shown in figure 6.12 gives the position of the peak to be $\omega_0 = 6.834683$ GHz with a width of 3.5 kHz. The width of the peak can be used to give a measure of the uncertainty on the determination of the central frequency of $\delta\omega/\omega_0 = 5.2 \times 10^{-7}$.

Although this is no match for a state of the art optical clock, the goal here was to demonstrate the atom interferometry capabilities of the iSense apparatus to show that the components are suitable for use in a quantum device platform. There are currently no technical limitations on measuring gravity using the system, however the much lower signal size requires an improvement in the signal to noise ratio of the detection. A high precision gravity measurement will require a detection system to be implemented in the lower section of the vacuum chamber.

6.4.4 Mobile Atom Interferometry

As described in chapter 5, the entire experiment was packed into a compact form factor and transported from the laboratory in Birmingham to the West Midlands Office in Brussels as the ultimate demonstration of the device. Upon arrival the system was checked

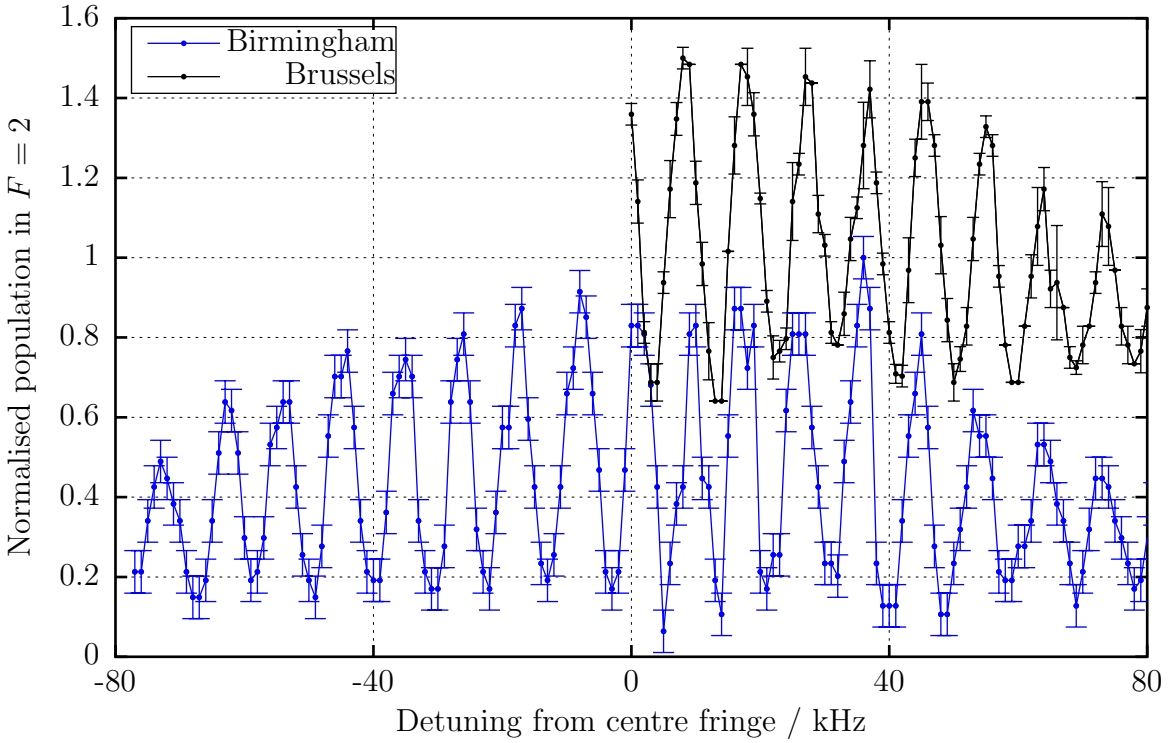

Figure 6.13: Ramsey fringes obtained at the West Midlands Office in Brussels after transportation (in black) compared to the previous results from Birmingham (in blue). A vertical offset of 0.5 has been added to the Brussels data to improve the clarity of the plot.

and the MOT was regenerated. Some recoupling of the Raman laser system was required to regain the same optical power as before transportation. Once everything was setup – the same detuning and power of 1.5 GHz and 35 mW as in Birmingham was used – Rabi oscillations were observed with the same $\pi/2$ time of 9 µs, albeit with an amplitude smaller by a factor of 10. The reduction in signal is likely due to the lower magnetic compensation and the higher optical molasses temperature that this causes. The addition of a magnetic shield will remove this issue.

Using these settings, we were able to recreate the Ramsey fringes in good agreement with those we obtained in Birmingham before packaging the system. Figure 6.13 shows the fringes from Brussels in black above the results from Birmingham in blue and with the same scale. Each Brussels datapoint is an average of three measurements, with statistical errors shown, they have also been offset vertically by 0.5 to improve the visibility of the plot. The same number of fringes are observed within the same frequency range (nine

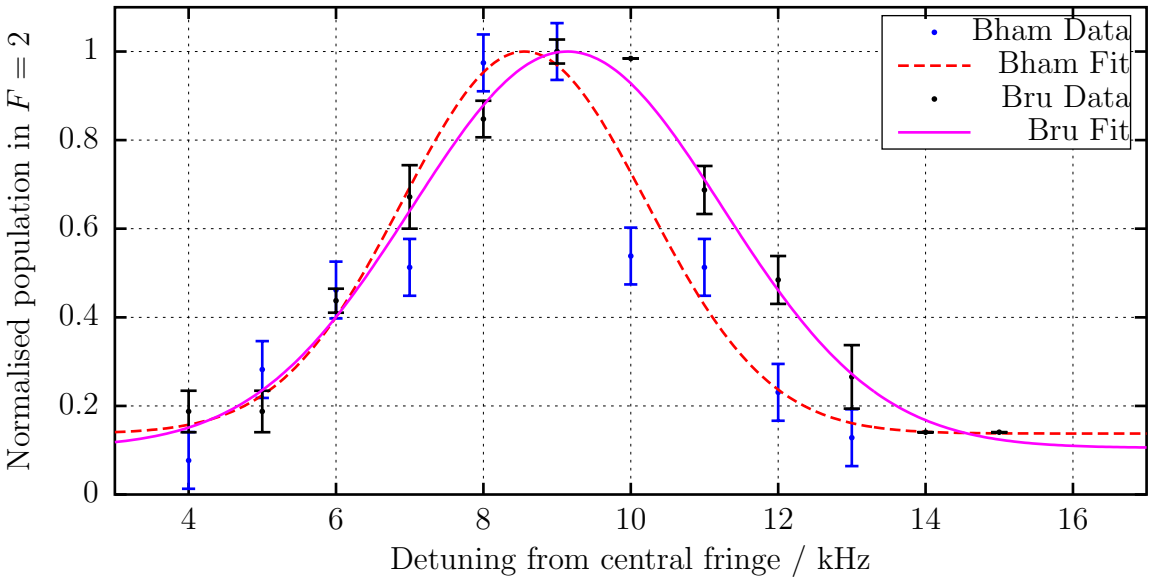

Figure 6.14: Single fringe of Ramsey interferometer signal comparison between Birmingham and Brussels results. The fringe width from Birmingham (blue and red, dashed, data) is 2.75 kHz. The width of the fringe from Brussels (black and magenta, solid, data) is 4.44 kHz. The difference in frequency between the maxima of the peaks is 0.58 kHz.

peaks from 0 kHz to 80 kHz). A fit of the envelope gives a value for the effective Raman pulse length of $\tau = 11.4 \pm 0.1$ µs. This value is comparable to the 11.1 ± 0.1 µs result from the Birmingham measurement.

A comparison of the first order fringes from each experimental run is shown in figure 6.14. The fringe from Birmingham is shown as the blue data and red dashed fit line, it has a fitted width of 2.75 kHz. The data from Brussels is shown in black and magenta and it can be seen that it has a larger width of 4.44 kHz. The difference in these fringe widths corresponds to a 2×10^{-7} variation on the frequency uncertainty $\delta\omega/\omega$. The increase in the fringe width for the Brussels data is most likely due to instabilities in the detuning of the Raman laser from the intermediate level.

There is a difference of 0.58 kHz between the positions of the maxima of the two peaks, this difference is within the errors on the precision of the frequency determination given by the fringe width. The non-optimised magnetic compensation after transportation could also cause a Zeeman shift of the frequency – second order only as the interferometry sequence only addresses the atoms in $m_\mathrm{f} = 0$. From [55], the Zeeman shift on the clock

transition is 575 Hz G^{-2}, suggesting that there could be an uncompensated magnetic field present at the atoms with a high strength of around 1 G. The packaged system had laser boxes with highly magnetic optical isolators inside close to the atoms that could have this effect, however this is a rather large magnetic field to be uncompensated so additional effects could be present.

6.5 Feasibility of iSense as a Gravimeter

The results presented in this chapter can be used to show the feasibility of using the iSense system as a gravimeter, and a theoretical limit can be placed on the resolution of a gravity measurement performed with the device.

If we were to implement a Kasevich-Chu type gravity scheme using the iSense sensor, the maximum freefall time available is 150 ms, giving a time between Raman pulses of $T = 75$ ms. During this time the phase accumulation of the atoms due to gravity is 4.4×10^5 rad. Using the high dispenser current setting from section 6.2.1, the number of atoms trapped in the MOT is 2.7×10^7. Not all of these atoms will be used in the interferometer. As discussed in section 6.4.1, the fact that the atoms begin in F=2 and are spread among all five m_f sublevels means that only 20 % are addressed by the Raman beam. From other experiments [109], the Raman velocity selection chooses 10 % of those remaining atoms, and then detection is only performed on 30 % of the atoms – the atoms near the centre of the cloud – at the output of the interferometer. This gives 1.6×10^5 atoms that will be involved in the final measurement and – if the system were atom shot noise limited – a resolution on the phase of 2.5 mrad.

The iSense device can achieve a repetition rate of 2 Hz for a gravity measurement of this kind, giving the final theoretical sensitivity to gravity of the iSense system to be

$$3.9\ \mu\text{Gal}/\sqrt{\text{Hz}}, \tag{6.8}$$

a value which is competitive with other portable cold atom gravimeters ($1-50\ \mu\text{Gal}/\sqrt{\text{Hz}}$)

and even the FG5 (15 µGal/$\sqrt{\text{Hz}}$).

The iSense system in its current state is not at the atom shot noise limit, nor is it yet as optimised as other portable cold atom gravimeters. There are however no fundamental barriers to reaching a sensitivity of this level with the system, and the additions of magnetic shielding and vibration isolation will be implemented to reach this target.

6.6 Summary

A 3D mirror-MOT has been generated and characterised with both absorption and fluorescence imaging systems. The MOT loads to 6.7×10^6 atoms in 2 seconds at the usual operating parameters, but can be easily increased to 2.75×10^7 atoms in 0.5 seconds by raising the dispenser current. The temperature of the MOT was measured to be 161 µK. After an optical molasses phase the measured temperature was reduced to just 4.4 ± 0.3 µK. It will prove difficult to reduce the temperature further, however this is a suitable starting point for interferometry schemes.

Following the cooling of the atoms, a Ramsey interferometer sequence was performed. A measurement of the central fringe width gave an uncertainty on the hyperfine splitting frequency of $\delta\omega/\omega_0 = 5.2 \times 10^{-7}$.

Finally, the experiment was repeated after packaging and transportation and the results were shown to be in good agreement with the results from the laboratory. The Ramsey fringes were recorded with the same frequency and sensitivity. The first order fringe from each measurement run was compared $\delta\omega_{\text{Bru}} = 4.44$ kHz versus $\delta\omega_{\text{Bham}} = 2.75$ kHz. An offset of 0.5 kHz was observed in the results from Brussels, and could be attributed to a high magnetic field present in the packaged system causing a second order Zeeman shift on the m_{f} states. The observation of atom interferometry after transportation is evidence that the technologies developed within this project are robust enough to operate together out of the comfort zone of the laboratory. An initial theoretical sensitivity to gravity has been presented which will require improvements, such as magnetic shielding

and vibration isolation.

CHAPTER 7

CONCLUSION AND OUTLOOK

This thesis presents the development, and current status, of the iSense demonstrator. The main goal of the project was to create a portable quantum technology platform to demonstrate that cold atom based devices are now advanced enough for 'real-world' applications. This was to be achieved through the construction of the iSense demonstrator; a portable system capable of performing atom interferometry outside the laboratory. Expertise from major research groups around Europe was brought together in Birmingham to achieve the project goal. The aim was to have the iSense demonstrator act as a 'launch pad' for the development of portable quantum sensors.

Compact laser systems distributed through a completely fibre based system have been implemented. A compact vacuum system was designed which weighed 10 kg after installation, including pumping section and the atom chip assembly. The atom chip assembly generates the MOT fields by using only 6.4 W of power. The mirror-MOT loads 6.7×10^6 atoms in 2 seconds at the usual operating parameters, at a temperature of $T_{\mathrm{MOT}} = 161 \pm 11$ µK, and this can be increased to 2.75×10^7 atoms in 350 ms by raising the dispenser current. After optical molasses, the cold atom cloud has a temperature of $T_{\mathrm{OM}} = 4.4$ µK which is lower than other mirror-MOT systems (typically > 8 µK, fully optimised) and comparable to 3D MOT systems (≈ 1 µK). This means that the iSense system generates a cold atom cloud that is a suitable starting point for performing precision atom interferometry measurements. Using this cloud, the theoretical sensitivity to

gravity of the system is 3.9 µGal/$\sqrt{\text{Hz}}$ at a repetition rate of 2 Hz; through the implementation of magnetic shielding and vibration isolation a sensitivity of this level should be achievable by the iSense device.

The large distance of the centre of the MOT from the surface of the chip leads to an improved quality of the beams reflected from the chip, allowing for a more balanced optical molasses to be carried out, therefore leading to lower temperatures. It is unlikely that the current iSense system will be able to reach the temperatures that are possible in standard setups. Temperatures at that level require excellent magnetic field compensation, which would be difficult in our system because of the metallic components of the atom chip assembly and their proximity to the atoms. The temperature that has been achieved shows that atom chips can create cold atom sources that are suitable for deployment in portable atom interferometers, an idea that was previously uncertain.

The temperature result obtained here can lead into further investigations with single beam atom traps that use atom chips with micro-patterned surfaces or macroscopic mirror setups. Chip-based interferometry schemes are also being researched [110, 111]. Combinations of these ideas could deliver substantial reductions in the size and complexity of quantum sensors. The cold atom temperatures reached by these systems are not yet proven to be suitable for atom interferometry however, based on the discoveries presented in this thesis, designs which generate the atomic clouds further from their surface could make this attainable.

Ramsey fringes of the 6.8 GHz hyperfine splitting in ^{87}Rb have been observed with a frequency uncertainty of $\delta\omega/\omega_0 = 5.2 \times 10^{-7}$ as evidence that the device is capable of atom interferometry. The portability and robustness of the iSense system has been demonstrated through the operation of a Ramsey atom interferometer in an office environment in Brussels after a journey of 570 km. The results of the transported measurement show Ramsey fringes that are comparable to the results from Birmingham, with an offset around 0.5 kHz. It is supposed that this was caused by a high magnetic field present in the packaged system inducing a Zeeman shift on the $m_\text{f} = 0$ state being probed. This will

be characterised and removed through the use of magnetic shielding.

The completed system has a volume of 120 litres, weight of 63 kg and a power requirement of 240 W. iSense can be (and indeed has been) transported by two people and operated by only one person. Further reductions in size and weight have been outlined such as single laser cooling methods and trapped interferometry techniques. These will improve future capabilities for land, sea and air uses on Earth. Interestingly, the device is also close to the limit where small to midsize satellite platforms are available; though further reductions in power, and increased robustness, would be required.

The next major step for iSense will be to observe interference fringes caused by gravity. This will involve the further automation of the computer control system for rapid measurement taking. Improvements to the stability of the laser system will be performed throughout such as alternative temperature and polarisation control. Magnetic shielding will also be required to achieve the final sensitivity of the system, and the FBH compact spectroscopy setup will also be integrated when completed and delivered. As a portable device, iSense can then begin to perform comparative measurements with other gravimeters. The Natural Environment Research Council (NERC) geodesy facility in Sussex, UK is planned to be one of the first test locations because they own and operate an FG5-X. It would also be beneficial to compare it to other cold atom gravimeters from the iSense team such as those at SYRTE and Humboldt Universität Berlin – possibly even to participate in one of the international gravimeter comparison campaigns. This would further cement the idea of replacing traditional gravimeters with quantum devices.

iSense has been seen to propel cold atom systems away from the academic community and into the wider world, and it has caught the attention of industry and the government in the UK. iSense is a key device within the Birmingham led UK National Quantum Technology Hub in Sensors and Metrology, where it will continue to be used as a test platform for novel technologies that will further reduce the size, weight and power of quantum sensors. We are on the cusp of the next ‘quantum revolution’.

LIST OF REFERENCES

[1] S M Dickerson, J M Hogan, A Sugarbaker, D M S Johnson, and M A Kasevich. Multiaxis inertial sensing with long-time point source atom interferometry. *Physical Review Letters*, 111, 2013.

[2] T L Nicholson et al. Systematic evaluation of an atomic clock at 2×10^{-18} total uncertainty. *Nature communications*, 6:6896, January 2015.

[3] D M Farkas, K M. Hudek, E A. Salim, S R Segal, M B Squires, and D Z Anderson. A compact, transportable, microchip-based system for high repetition rate production of Bose-Einstein condensates. *Applied Physics Letters*, 96(9):093102, March 2010.

[4] Coldquanta website. `http://www.coldquanta.com/`. Retrieved: 01/07/2015.

[5] R Geiger et al. Detecting inertial effects with airborne matter-wave interferometry. *Nature communications*, 2:474, January 2011.

[6] T van Zoest et al. Bose-Einstein condensation in microgravity. *Science (New York, N.Y.)*, 328(5985):1540–3, June 2010.

[7] D N Aguilera et al. STE-QUEST test of the universality of free fall using cold atom interferometry. *Classical and Quantum Gravity*, 31(11):115010, 2014.

[8] C Jönsson. Electron diffraction at multiple slits. *Zeitschrift für Physik*, 161, 1961.

[9] N F Ramsey. A molecular beam resonance method with separated oscillating fields. *Physical Review*, 78:695, 1950.

[10] A W Overhauser and R Colella. Experimental test of gravitationally induced quantum interference. *Phys. Rev. Lett.*, 33:1237–1239, Nov 1974.

[11] R Colella, A Overhauser, and S Werner. Observation of Gravitationally Induced Quantum Interference. *Physical Review Letters*, 34(23):1472–1474, June 1975.

[12] M Kasevich and S Chu. Atomic interferometry using stimulated raman transitions. *Physical Review Letters*, 67(2):181–184, Jul 1991.

[13] Ch J Bordé, Ch Salomon, S Avrillier, A van Lerberghe, Ch Bréant, D Bassi, and G Scoles. Optical Ramsey fringes with traveling waves. *Physical Review A*, 30(4): 1836–1848, October 1984.

[14] M Kasevich and S Chu. Measurement of the gravitational acceleration of an atom with a light-pulse atom interferometer. *Applied Physics B*, 54(5):321–332, May 1992.

[15] B Brezger, L Hackermüller, S Uttenthaler, J Petschinka, M Arndt, and A Zeilinger. Matter-Wave Interferometer for Large Molecules. *Physical Review Letters*, 88(10): 100404, February 2002.

[16] S Gerlich, S Eibenberger, M Tomandl, S Nimmrichter, K Hornberger, P J Fagan, J Tüxen, M Mayor, and M Arndt. Quantum interference of large organic molecules. *Nature communications*, 2:263, January 2011.

[17] Z-K Hu, B-L Sun, X-C Duan, M-K Zhou, L-L Chen, S Zhan, Q-Z Zhang, and J Luo. Demonstration of an ultrahigh-sensitivity atom-interferometry absolute gravimeter. *Physical Review A*, 88(4):043610, October 2013.

[18] J B Fixler, G T Foster, J M McGuirk, and M A Kasevich. Atom interferometer measurement of the newtonian constant of gravity. *Science (New York, N.Y.)*, 315 (5808):74–7, January 2007.

[19] G Rosi, F Sorrentino, L Cacciapuoti, M Prevedelli, and G M Tino. Precision measurement of the Newtonian gravitational constant using cold atoms. *Nature*, 510(7506):518–21, June 2014.

[20] M Snadden, J McGuirk, P Bouyer, K Haritos, and M Kasevich. Measurement of the Earth's Gravity Gradient with an Atom Interferometer-Based Gravity Gradiometer. *Physical Review Letters*, 81(5):971–974, August 1998.

[21] G Rosi, L Cacciapuoti, F Sorrentino, M Menchetti, M Prevedelli, and GM Tino. Measurement of the Gravity-Field Curvature by Atom Interferometry. *Physical Review Letters*, 114(1):013001, January 2015.

[22] A Gauguet, B Canuel, T Lévèque, W Chaibi, and A Landragin. Characterization and limits of a cold-atom Sagnac interferometer. *Physical Review A*, 80(6):063604, December 2009.

[23] D Schlippert, J Hartwig, H Albers, L L Richardson, C Schubert, A Roura, W P Schleich, W Ertmer, and E M Rasel. Quantum Test of the Universality of Free Fall. *Physical Review Letters*, 112(20):203002, May 2014.

[24] A Wicht, J M Hensley, E Sarajlic, and S Chu. A preliminary measurement of the fine structure constant based on atom interferometry. *Physica scripta*, T102:82, 2002.

[25] P Cladé, E de Mirandes, M Cadoret, S Guellati-Khélifa, C Schwob, F Nez, L Julien, and F Biraben. Determination of the Fine Structure Constant Based on Bloch Oscillations of Ultracold Atoms in a Vertical Optical Lattice. *Physical Review Letters*, 96(3):033001, January 2006.

[26] S-W Chiow, S Herrmann, S Chu, and H Müller. Noise-Immune Conjugate Large-Area Atom Interferometers. *Physical Review Letters*, 103(5):050402, July 2009.

[27] P W Graham, J M Hogan, M A Kasevich, and S Rajendran. New Method for Gravitational Wave Detection with Atomic Sensors. *Physical Review Letters*, 110 (17):171102, April 2013.

[28] S Dimopoulos, P Graham, J Hogan, M Kasevich, and S Rajendran. Atomic gravitational wave interferometric sensor. *Physical Review D*, 78(12):122002, December 2008.

[29] J Sauer, M Barrett, and M Chapman. Storage Ring for Neutral Atoms. *Physical Review Letters*, 87(27):270401, December 2001.

[30] S Wu, W Rooijakkers, P Striehl, and M Prentiss. Bidirectional propagation of cold atoms in a stadium-shaped magnetic guide. *Physical Review A*, 70(1):013409, July 2004.

[31] W Torge. *Gravimetry*. Walter de Gruyter, 1st edition, 1989.

[32] T M Niebauer, G S Sasagawa, J E Faller, R Hilt, and F Klopping. A new generation of absolute gravimeters. *Metrologia*, 32(3):159, 1995.

[33] R Rummel. Geoid and gravity in earth sciences an overview. *Earth, Moon, and Planets*, 94:3–11, 2004.

[34] J Bouman, M Fuchs, E Ivins, W van der Wal, E Schrama, P Visser, and M Horwath. Antarctic outlet glacier mass change resolved at basin scale from satellite gravity gradiometry. *Geophysical Research Letters*, 41(16):5919–5926, August 2014.

[35] J Müller, M Naeimi, O Gitlein, L Timmen, and H Denker. A land uplift model in Fennoscandia combining GRACE and absolute gravimetry data. *Physics and Chemistry of the Earth, Parts A/B/C*, 53-54:54–60, January 2012.

[36] S Branca, D Carbone, and F Greco. Intrusive mechanism of the 2002 NE-Rift eruption at Mt. Etna (Italy) inferred through continuous microgravity data and volcanological evidences. *Geophysical Research Letters*, 30(20):3–6, 2003.

[37] N Metje et al. Mapping the Underworld State-of-the-art review. *Tunnelling and Underground Space Technology*, 22(5-6):568–586, September 2007.

[38] J M Goodkind. The superconducting gravimeter. *Review of Scientific Instruments*, 70(11):4131, November 1999.

[39] GWR instruments, inc. `www.gwrinstruments.com`. Retrieved: 01/07/2015.

[40] O Francis et al. The European Comparison of Absolute Gravimeters 2011 (ECAG-2011) in Walferdange, Luxembourg: results and recommendations. *Metrologia*, 50 (3):257–268, June 2013.

[41] Micro-g lacoste website. `www.microglacoste.com`. Retrieved: 01/07/2015.

[42] L Timmen, O Gitlein, V Klemann, and D Wolf. Observing Gravity Change in the Fennoscandian Uplift Area with the Hanover Absolute Gravimeter. *Pure and Applied Geophysics*, 169:1331–1342, August 2012.

[43] M Schmidt, A Senger, M Hauth, C Freier, V Schkolnik, and A Peters. A mobile high-precision absolute gravimeter based on atom interferometry. *Gyroscopy and Navigation*, 2(3):170–177, August 2011.

[44] M Hauth, C Freier, V Schkolnik, A Senger, M Schmidt, and A Peters. First gravity measurements using the mobile atom interferometer GAIN. *Applied Physics B*, April 2013.

[45] S Merlet, Q Bodart, N Malossi, A Landragin, F Pereira Dos Santos, O Gitlein, and L Timmen. Comparison between two mobile absolute gravimeters: optical versus atomic interferometers. *Metrologia*, 47(4):L9–L11, August 2010.

[46] Y Bidel, O Carraz, R Charrière, M Cadoret, N Zahzam, and A Bresson. Compact cold atom gravimeter for field applications. *Applied Physics Letters*, 102(14):144107, 2013.

[47] Xinan Wu. *Gravity Gradient Survey with a Mobile Atom Interferometer*. PhD thesis, Stanford University, 2009.

[48] L Zhou, Z-Y Xiong, W Yang, B Tang, W-C Peng, Y-B Wang, P Xu, J Wang, and M-S Zhan. Measurement of Local Gravity via a Cold Atom Interferometer. *Chinese Physics Letters*, 28(1):013701, January 2011.

[49] B Wu, Z Wang, B Cheng, Q Wang, A Xu, and Q Lin. The investigation of a μGal-level cold atom gravimeter for field applications. *Metrologia*, 51(5):452–458, October 2014.

[50] M Hauth. *A mobile, high-precision atom-interferometer and its application to gravity observations*. PhD thesis, Humboldt-Universität zu Berlin, 2015.

[51] H J Metcalf and P van der Straten. *Laser Cooling and Trapping*. Springer-Verlag, 1st edition, 1999.

[52] C J Foot. *Atomic Physics*. Oxford University Press, 1st edition, 2005.

[53] W Ertmer, R Blatt, J L Hall, and M Zhu. Laser manipulation of atomic beam velocities: Demonstration of stopped atoms and velocity reversal. *Physical Review Letters*, 54(10):996–999, March 1985.

[54] S Chu, L Hollberg, J E Bjorkholm, A Cable, and A Ashkin. Three-dimensional viscous confinement and cooling of atoms by resonance radiation pressure. *Physical Review Letters*, 55(1):48, 1985.

[55] D A Steck. Rubidium 87 D line data. available online at http://steck.us/alkalidata (revision 2.1.4, 23 December 2010).

[56] P D Lett, R N Watts, C Westbrook, W D Phillips, P Gould, and H J Metcalf. Observation of atoms laser cooled below the Doppler limit. *Physical Review Letters*, 61(2):169–173, July 1988.

[57] J Dalibard and C Cohen-Tannoudji. Laser cooling below the doppler limit by polarization gradients: simple theoretical models. *J. Opt. Soc. Am. B*, 6(11):2023–2045, Nov 1989.

[58] A L Migdall, J V Prodan, W D Phillips, T H Bergeman, and H J Metcalf. First observation of magnetically trapped neutral atoms. *Physical Review Letters*, 54(24): 2596–2599, 1985.

[59] A Arnold. *Preparation and Manipulation of an ^{87}Rb Bose-Einstein Condensate.* PhD thesis, University of Sussex, 1999.

[60] J Reichel, W Hänsel, and T W Hänsch. Atomic micromanipulation with magnetic surface traps. *Phys. Rev. Lett.*, 83(17):3398–3401, 1999.

[61] P R Berman, editor. *Atom Interferometry.* Academic Press, 1st edition, 1997.

[62] Brenton Young, Mark Kasevich, and Steven Chu. Precision atom interferometry with light pulses. In P R Berman, editor, *Atom Interferometry*, page 363. Academic Press, Inc, 1st edition, 1997.

[63] F K Fatemi, M L Terraciano, M Bashkansky, and Z Dutton. Cold atom Raman spectrography using velocity-selective resonances. *Optics express*, 17(15):12971–12980, 2009.

[64] E Mach. Ueber einen interferenzrefraktor. *Zeitschrift für Instrumentenkunde*, 12: 89–93, 1892.

[65] Ch J Bordé. Atomic interferometry with internal state labelling. *Physics letters A*, 140(1):3–5, 1989.

[66] A Peters, KY Chung, and S Chu. Measurement of gravitational acceleration by dropping atoms. *Nature*, 400:849–852, 1999.

[67] L Zhou, Z Y Xiong, W Yang, B Tang, W C Peng, K Hao, R B Li, M Liu, J Wang, and M S Zhan. Development of an atom gravimeter and status of the 10-meter atom

interferometer for precision gravity measurement. *General Relativity and Gravitation*, 43(7):1931–1942, 2011.

[68] J Hartwig, S Abend, C Schubert, D Schlippert, H Ahlers, K Posso-Trujillo, N Gaaloul, W Ertmer, and E M Rasel. Testing the universality of free fall with rubidium and ytterbium in a very large baseline atom interferometer. *New Journal of Physics*, 17(3):035011, 2015.

[69] P Cladé, S Guellati-Khélifa, C Schwob, F Nez, L Julien, and F Biraben. A promising method for the measurement of the local acceleration of gravity using Bloch oscillations of ultracold atoms in a vertical standing wave. *Europhysics Letters (EPL)*, 71(5):730–736, September 2005.

[70] N Poli, F-Y Wang, M Tarallo, A Alberti, M Prevedelli, and G Tino. Precision Measurement of Gravity with Cold Atoms in an Optical Lattice and Comparison with a Classical Gravimeter. *Physical Review Letters*, 106(3), January 2011.

[71] Q Beaufils, G Tackmann, X Wang, B Pelle, S Pelisson, P Wolf, and F dos Santos. Laser Controlled Tunneling in a Vertical Optical Lattice. *Physical Review Letters*, 106(21), May 2011.

[72] G Tackmann, B Pelle, A Hilico, Q Beaufils, and F Pereira Dos Santos. Raman-laser spectroscopy of Wannier-Stark states. *Physical Review A*, 84(6), October 2011.

[73] R Charrière, M Cadoret, N Zahzam, Y Bidel, and A Bresson. Local gravity measurement with the combination of atom interferometry and bloch oscillations. *Phys. Rev. A*, 85:013639, Jan 2012.

[74] Website of the QUANTUS project. `http://www.iqo.uni-hannover.de/quantus.html`. Retrieved: 01/07/2015.

[75] M H Anderson, J R Ensher, M R Matthews, C E Wieman, and E A Cornell. Observation of Bose-Einstein condensation in a dilute atomic vapor. *Science (New York, N.Y.)*, 269(5221):198–201, July 1995.

[76] W Hänsel, P Hommelhoff, T W Hänsch, and J Reichel. Bose-Einstein condensation on a microelectronic chip. *Nature*, 413(6855):498–501, October 2001.

[77] D M Farkas, E A Salim, and J Ramirez-Serrano. Production of rubidium Bose-Einstein condensates at a 1 hz rate. *ArXiv e-prints*, 1403.4641, March 2014.

[78] J Rudolph et al. A high-flux BEC source for mobile atom interferometers. *New Journal of Physics*, 17(6):065001, June 2015.

[79] A Piccardo-Selg. *Cold Atom Sources for Portable Quantum Sensors*. PhD thesis, University of Nottingham, 2013.

[80] S G Cox, P F Griffin, C S Adams, D DeMille, and E Riis. Reusable ultrahigh vacuum viewport bakeable to 240°C. *Review of Scientific Instruments*, 74(6):3185–3187, 2003.

[81] B Kaltenhäuser, H Kübler, A Chromik, J Stuhler, and T Pfau. Low retaining force optical viewport seal. *Review of Scientific Instruments*, 78(4):046107, 2007.

[82] S Spießberger, M Schiemangk, A Sahm, A Wicht, H Wenzel, and A Peters. Micro-integrated 1 Watt semiconductor laser system with a linewidth of 3.6 kHz. *Optics Express*, 19(8):7077–7083, 2011.

[83] Isowave website. `www.isowave.com`. Retrieved: 21/10/2015.

[84] H Duncker, O Hellmig, A Wenzlawski, A Grote, A J Rafipoor, M Rafipoor, K Sengstock, and P Windpassinger. Ultrastable, Zerodur-based optical benches for quantum gas experiments. *Applied optics*, 53(20):4468–74, July 2014.

[85] L Ricci, M Weidemüller, T Esslinger, A Hemmerich, C Zimmermann, V Vuletic, W König, and T W Hänsch. A compact grating-stabilized diode laser system for atomic physics. *Optics Communications*, 117(5-6):541–549, June 1995.

[86] E Luvsandamdin, S Spießberger, M Schiemangk, A Sahm, G Mura, A Wicht, A Peters, G Erbert, and G Tränkle. Development of narrow linewidth, micro-integrated extended cavity diode lasers for quantum optics experiments in space. *Applied Physics B*, 111(2):255–260, January 2013.

[87] E Luvsandamdin, C Kürbis, M Schiemangk, A Sahm, A Wicht, A Peters, G Erbert, and G Tränkle. Micro-integrated extended cavity diode lasers for precision potassium spectroscopy in space. *Optics Communications*, 22(7):7790–7798, 2014.

[88] J O Maclean, M T Greenaway, R P Campion, T Pyragius, T M Fromhold, A J Kent, and C J Mellor. III-V semiconductor waveguides for photonic functionality at 780 nm. In *SPIE OPTO*, pages 898805–898805. International Society for Optics and Photonics, 2014.

[89] B Arar et al. Double-heterostructure ridge-waveguide GaAs/AlGaAs phase modulator for 780nm lasers. *Applied Physics B*, 116(1):175–181, October 2013.

[90] H Müntinga et al. Interferometry with Bose-Einstein Condensates in Microgravity. *Physical Review Letters*, 110(9):093602, February 2013.

[91] J M Supplee, E A Whittaker, and W Lenth. Theoretical description of frequency modulation and wavelength modulation spectroscopy. *Applied optics*, 33(27):6294–302, September 1994.

[92] D J McCarron, S A King, and S L Cornish. Modulation transfer spectroscopy in atomic rubidium. *Measurement Science and Technology*, 19(10):105601, 2008.

[93] C C Nshii et al. A surface-patterned chip as a strong source of ultracold atoms for quantum technologies. *Nature nanotechnology*, 8(5):321–4, May 2013.

[94] M Vangeleyn, P F Griffin, E Riis, and A S Arnold. Single-laser, one beam, tetrahedral magneto-optical trap. *Optics Express*, 17(16):13601, July 2009.

[95] Q Bodart, S Merlet, N Malossi, F Pereira Dos Santos, P Bouyer, and A Landragin. A cold atom pyramidal gravimeter with a single laser beam. *Applied Physics Letters*, 96(13):134101, 2010.

[96] Z Gan, D Huang, X Wang, D Lin, and S Liu. Getter free vacuum packaging for MEMS. *Sensors and Actuators A: Physical*, 149(1):159–164, January 2009.

[97] J Rushton, M Aldous, and M Himsworth. The Feasibility of a Fully Miniaturized Magneto-Optical Trap for Portable Ultracold Quantum Technology. *ArXiv e-prints*, 1405.3148, May 2014.

[98] A da Silva Curiel, A Carrel, A Cawthorne, L Gomes, M Sweeting, and F Chizea. Commissioning of nigeriasat-2 high resolution imaging mission. In *Annual AIAA/USU Conference on Small Satellites*, pages SSC12–XI–6. Optical Society of America, 2012.

[99] V Ménoret, R Geiger, G Stern, N Zahzam, B Battelier, A Bresson, A Landragin, and P Bouyer. Dual-wavelength laser source for onboard atom interferometry. *Optics letters*, 36(21):4128–30, November 2011.

[100] F Theron, O Carraz, G Renon, N Zahzam, Y Bidel, M Cadoret, and A Bresson. Narrow linewidth single laser source system for onboard atom interferometry. *Applied Physics B*, 118(1):2–5, December 2014.

[101] R W G Moore, L A Lee, E A Findlay, L Torralbo-Campo, G D Bruce, and D Cassettari. Measurement of Vacuum Pressure with a Magneto-Optical Trap: a Pressure-Rise Method. *ArXiv e-prints*, 1401.7949, January 2014.

[102] T Arpornthip, C A Sackett, and K J Hughes. Vacuum Pressure Measurements using a Magneto-Optical Trap. *Physical Review A*, 85(3):033420, March 2012.

[103] W Herr. *Eine kompakte Quelle quantenentarteter Gase hohen Flusses für die Atominterferometrie unter Schwerelosigkeit*. PhD thesis, Leibniz Universität Hannover, 2013.

[104] S Du. *Atom-chip Bose-Einstein condensation in a portable vacuum cell*. PhD thesis, University of Colorado, 2005.

[105] I G Hughes and T P A Hase. *Measurements and their Uncertainties*. Oxford University Press, 2010.

[106] P Böhi, M F Riedel, J Hoffrogge, J Reichel, T W Hänsch, and P Treutlein. Coherent manipulation of Bose-Einstein condensates with state-dependent microwave potentials on an atom chip. *Nature Physics*, 5(8):592–597, July 2009.

[107] P A Böhi. *Coherent manipulation of ultracold atoms with microwave near-fields*. PhD thesis, Max-Planck-Institut für Quantenoptik, 2010.

[108] M Kasevich, D S Weiss, E Riis, K Moler, S Kasapi, and S Chu. Atomic velocity selection using stimulated Raman transitions. *Physical review*, 66(18):2297–2300, 1991.

[109] M Schmidt. *A mobile high-precision absolute gravimeter based on atom interferometry*. PhD thesis, Humbolt-Universität zu Berlin, 2011.

[110] C Deutsch, F Ramirez-Martinez, C Lacroûte, F Reinhard, T Schneider, J N Fuchs, F Piéchon, F Laloë, J Reichel, and P Rosenbusch. Spin Self-Rephasing and Very Long Coherence Times in a Trapped Atomic Ensemble. *Physical Review Letters*, 105(2):020401, July 2010.

[111] M Ammar, M Dupont-Nivet, L Huet, J-P Pocholle, P Rosenbusch, I Bouchoule, C I Westbrook, J Estève, J Reichel, C Guerlin, and S Schwartz. Symmetric microwave potentials for interferometry with thermal atoms on a chip. *ArXiv e-prints*, 1412.7433, December 2014.

[112] Thorlabs, Inc. *Si Biased Detector DET36A/M*, March 2015. Rev. D.

APPENDIX A

ISENSE MEMBER INSTITUTIONS

Abbr.	Name	Country
UBham (Coordinator)	The University of Birmingham	GB
UNott	University of Nottingham	GB
UHH	Universität Hamburg	DE
SYRTE	Centre National de la Recherche Scientifique: SYRTE	FR
UNIFI	University of Florence	IT
LUH	Leibniz Universität Hannover	DE
OEAW	Institute for Quantum Optics and Quantum Information - Austrian Academy of Sciences	AT
FBH	Ferdinand Braun Institut für Höchsfrequenz-technik im Forschungsverbund Berlin	DE
ONERA	Office National d'Etudes et de Recherches Aérospatiales	FR

Table A.1: List of members of the iSense collaboration.

APPENDIX B

IMAGING

B.1 Fluorescence Image Analysis

A photodiode was used to take fluorescence images of the MOT and for detection after the atom interferometry sequence. For our setup, the cloud was imaged onto the photodiode with a 25.4 mm radius lens 60 mm from the atoms, giving a solid angle of $\Omega = 2.95 \times 10^{-2}$. The photodiode generates a current based on the number of photons that it observes. This is called the photocurrent and is given by

$$i = eR_{\text{scat}}\Omega NQ \tag{B.1}$$

with e the electron charge, R_{scat} the photon scattering rate, N the atom number. Q is the quantum efficiency of the photodiode and was converted from the responsivity $\mathcal{R}$ of 0.48 A/W (quoted in [112], and verified in the laboratory) at $\lambda = 780$ nm using

$$Q = \frac{\mathcal{R}hc}{\lambda e}. \tag{B.2}$$

The saturation parameter s_0 is the ratio of beam intensity to saturation intensity of

the transition used. Our beam intensity gives us a value

$$\begin{aligned} s_0 = \frac{I}{I_{\text{sat}}} &= \frac{29.84}{1.669} \\ &= 17.86, \end{aligned}$$

where $I_{\text{sat}} = 1.669\ \text{mW}\,\text{cm}^{-2}$ for ^{87}Rb [55] and I is for the six MOT beams at 18 mm and 10 mW.

To obtain the scattering rate, we need to know how many atoms are involved in scattering events. The percentage of the population in the excited state is given by

$$p = \frac{s_0}{2\left(1 + s_0 + \left(2\frac{\Delta}{\Gamma}\right)^2\right)}, \tag{B.3}$$

for a specific detuning Δ and beam intensity. Multiplying this by the linewidth gives us the scattering rate of our cooling light photons from the atoms as $R_{\text{scat}} = 9.6 \times 10^6\ \text{s}^{-1}$.

The photodiode voltage is measured over a load resistance of $R_{\text{load}} = 1.0\ \text{M}\Omega$ and can be written as $V = iR_{\text{load}}$. Inserting equation (B.1) and rearranging gives the atom number as a function of photodiode voltage

$$N = \frac{V}{eR_{\text{scat}}\Omega Q R_{\text{load}}}. \tag{B.4}$$

B.2 Absorption Image Analysis

The processs of absorption imaging uses a near resonant beam incident on the atomic cloud. The atoms absorb photons from the beam and this leaves a shadow on the beam. It can be used to calculate the optical density of the cloud, and consequently the number of atoms can be extracted.

The optical density is calculated by taking three absorption images; one image containing the atoms and detection light I_{atoms}, one with just the detection light I_{noatoms} and a background image with all sources of light turned off I_{bkg}. The optical density is then

calculated with

$$OD = \ln\left(\frac{I_{\text{atoms}} - I_{\text{bkg}}}{I_{\text{noatoms}} - I_{\text{bkg}}}\right). \tag{B.5}$$

The integration of the optical density over the entire image is then performed. This is related to the number of atoms by a conversion factor

$$N = OD_{\text{SUM}} \times \frac{\omega_0^2}{6\pi c^2}\left(1 + \frac{4\delta^2}{\Gamma^2} + \frac{I_{\text{beam}}}{I_{\text{sat}}}\right), \tag{B.6}$$

which is dependant on the detuning of the detection light δ and the ratio of the beam intensity to the saturation intensity of the transition $I_{\text{beam}}/I_{\text{sat}}$. ω_0 and Γ are the wavelength and linewidth of the detection transition. For a physical system, (B.6) must be multiplied by the detection area per pixel for the imaging system used.